

THESIS

2
2000



This is to certify that the
dissertation entitled

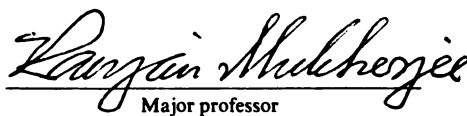
**DESIGN AND CONTROL OF CONTRAINED ROBOTIC SYSTEMS FOR
ENHANCED DEXTERITY AND MOBILITY**

presented by

Mark Andrew Minor

has been accepted towards fulfillment
of the requirements for

Ph.D. _____ degree in Mechanical Engineering


Major professor

Date May 04, 2000

PLACE IN RETURN BOX to remove this checkout from your record.
TO AVOID FINES return on or before date due.
MAY BE RECALLED with earlier due date if requested.

| DATE DUE | DATE DUE | DATE DUE |
|-------------|----------|----------|
| MAY 03 2007 | | |
| | | |
| | | |
| | | |
| | | |
| | | |
| | | |
| | | |
| | | |
| | | |

Design and Control of Constrained Robotic Systems for Enhanced Dexterity and Mobility

By

Mark Andrew Minor

A DISSERTATION

Submitted to
Michigan State University
in partial fulfillment of the requirements
for the degree of

DOCTOR OF PHILOSOPHY

Department of Mechanical Engineering

2000

ABSTRACT

Design and Control of Constrained Robotic Mechanisms for Enhanced Dexterity and Mobility

By

Mark Andrew Minor

With continued developments in the field of robotics, there has been considerable research on manipulation, mobility, and control. Research in these areas has led to the development of sophisticated mechanisms and systems with enhanced capabilities. While innovations in actuator and sensor technology has significantly contributed towards meeting new challenges, the design problems have become increasingly complex due to greater number of constraints imposed by limitations in space, weight, power, and computational capability. Innovative design and control is often the key to successful implementation of these systems and the subject of this dissertation. Presented herein is the design of three separate systems, each with its own unique challenges in dexterity, mobility, and control. Specifically, we present the design of a dexterous mechanism for minimally invasive surgery, a miniature climbing robot for reconnaissance operation, and the control of a spherical robot which offers to provide maximum mobility and stability.

A surgical instrument was designed for minimally invasive surgery with optimized load capacity and dexterity. The instrument fits through a standard 10 mm port and is optimized for bi-directional 180° articulation and unlimited rotation of a pair of forceps at the tip of the instrument. The state-of-the-art in surgical instrumentation does not have similar capabilities. A miniature climbing-robot for inspection and reconnaissance in urban environments is also developed. Similar to the surgical instrument design, which is constrained by space limitations, the climbing-robot design is constrained by weight, size, and power usage. A biped kinematic structure was chosen for the climbing-robot for its inherent advantages. This kinematic structure allows the robot to traverse horizontal and

vertical surfaces, and transition between surfaces of different inclination. Similar to the climbing-robot, the spherical robot is intended for reconnaissance missions, but its control problem is more challenging due to the presence of nonholonomic constraints. A unique coordinate system is defined on the sphere for the purpose of control – this results in simple linear and curvilinear motion on the plane for independent control action. These motions are exploited to design trajectories between initial and final configurations of the sphere described by the two Cartesian coordinates of its point of contact and three orientation coordinates. The solution of these trajectories are straightforward and require minimal computation. Among the three problems considered, experimental work was done with the climbing-robot. The robot was designed, built, and tested under computer control.

Copyright by
Mark Andrew Minor
2000

To my loving wife Kristin...
...we finally get to move on to the next stage of life.

ACKNOWLEDGMENTS

I would like to take this opportunity to thank and acknowledge those who have helped me complete this milestone in my life. It is impossible mention everyone since this has been a lifelong process beginning in elementary school in and proceeding through my graduate degrees. My parents, of course, come first since they have been so crucial to nurturing my work etiquette, passion to help people, and mechanical inclinations. They have given me so many advantages in life, I cannot thank them enough.

I must also state my appreciation to Northwestern Michigan College. The faculty at NMC (Dick Minor, Jim Coughlin, Terry Sievert, Ray Niergarth, Jay Berry, Lesslie Spencer, Jerry Williams, Bob Rudd, Adam Gahn, Ken Stepnitz, Erik Wildman, and Steve Balance, to name a few) have played a pivotal role in helping me realize my passion for both education and engineering. They provided me with an unsurpassed foundation in math, science, machining, and manufacturing techniques that I use as a daily, and I would have certainly taken a different path in life if not for these individuals.

At the University of Michigan, I developed my passion for design, modeling, and control of dynamic systems. The teachings of Drs. Bruce Karnopp, Robert Keller, Noboru Kikuchi and Alan Ward played significant roles in developing this passion and luring me to graduate school, for which I am thankful.

Of course, I must thank Dr. Craig Somerton for attracting me to Michigan State University. MSU has offered an excellent education and opportunities to refine my teaching skills. For these teaching opportunities, I am thankful to Dr. Ronald Rosenberg. He has provided me many opportunities at MSU and has been a very inspiring educator

and advisor. Likewise I must thank Drs. Clarke Radcliffe, Steve Shaw, Brian Feeny, Alejandro Diaz, Alan Haddow, Hassan Khalil, and Craig Gunn for their active roles in helping me expand my understanding of dynamics systems, design methodologies, and teaching. I must also extend thanks to my PhD advisor, Ranjan Mukherjee. He has provided me with many great opportunities to work on very exciting research projects and in turn develop the skills to profit on these with publications, patents, and proposals.

Lastly, I must thank all of my friends at MSU. The dynamic systems group, Brookes Byam, Charles Birdsong, Joe DeRose, Joga Setiawan, Tuhin Das, Gary Gosciak, Brennan Sicks, and Sally Starr have provided countless hours of stress relief, lunch time follies, and stimulating discussions. Without their support, this would have been a much more difficult process. I must also thank the Mechanical Engineering staff, which includes Carol Bishop, Aida Rodriguez, Nancy Chism, Kathy Chomas, and Roy Bailiff, who have always been there to help me and lend a hand in times of need.

More than anything, though, all of these fine people I have acknowledged have been like family, and family is what makes life so enjoyable.

TABLE OF CONTENTS

| | |
|--|-----|
| LIST OF TABLES | xi |
| LIST OF FIGURES..... | xii |
| LIST OF ABBREVIATIONS | xvi |
| 1. Introduction | 1 |
| 1.1 A New Era..... | 1 |
| 1.2 Objectives..... | 1 |
| 1.3 Document Structure..... | 2 |
| 2. A Surgical Mechanism with Enhanced Dexterity and Reachability | 4 |
| 2.1 Motivation | 4 |
| 2.2 Related Research | 6 |
| 2.3 Design of an Articulated Mechanism..... | 8 |
| 2.3.1 Kinematic Structure..... | 8 |
| 2.3.2 Input-Output Force Relationship..... | 9 |
| 2.3.3 Optimization of the AMMIS Link Configuration | 14 |
| 2.4 Dexterous Articulated Linkage for Surgical Applications | 17 |
| 2.4.1 Methodologies Explored | 17 |
| 2.4.2 Description of Functionality..... | 18 |
| 2.4.3 Force Analysis..... | 20 |
| 2.4.4 Load Capacity Maximization | 24 |
| 2.5 Manufacturing, Performance, and Practical Considerations | 27 |
| 2.6 Other Considerations..... | 29 |
| 3. Design and Implementation of a Miniature Climbing Robot..... | 30 |
| 3.1 Motivation | 30 |

| | | |
|-------|---|----|
| 3.2 | Basic Structure | 31 |
| 3.3 | Existing Wall Climbing Robots | 32 |
| 3.4 | Design Constraints | 35 |
| 3.5 | Robot Kinematics..... | 36 |
| 3.5.1 | General Form..... | 36 |
| 3.5.2 | Performance Criteria | 37 |
| 3.5.3 | Joint Structure: The Simple Biped | 38 |
| 3.5.4 | Joint Structure: The Two-Legged Biped (revolute hip joint)..... | 40 |
| 3.5.5 | Joint Structure: The Two-Legged Biped (prismatic hip joint)..... | 42 |
| 3.5.6 | Joint Structure: the Two-Legged Biped (hybrid hip joint)..... | 43 |
| 3.5.7 | Selection of Kinematics Structure..... | 47 |
| 3.5.8 | Coupled DOF and the Two-Legged Biped | 49 |
| 3.6 | Robot Design..... | 52 |
| 3.6.1 | Biped Structure..... | 52 |
| 3.6.2 | Force Analysis: climbing a vertical surface supported by foot 1 | 57 |
| 3.6.3 | Force Analysis: climbing a vertical surface supported by Foot 2 | 62 |
| 3.6.4 | Force Analysis: Steering on a vertical surface while supported by Foot 2 .. | 64 |
| 3.6.5 | Actuator Selection Criteria..... | 65 |
| 3.6.6 | Actuator Selection | 69 |
| 3.6.7 | Structural Optimization | 73 |
| 3.7 | Testing..... | 78 |
| 3.8 | Future Work | 80 |
| 3.9 | Other Considerations..... | 81 |
| 4. | Control of a Spherical Robot for Enhanced Mobility | 83 |
| 4.1 | Motivation | 83 |

| | |
|---|-----|
| 4.2 Kinematics Model | 87 |
| 4.3 Reachability of Arbitrary Configurations | 92 |
| 4.4 Kinematics Models in the Literature | 96 |
| 4.5 Traditional Nonholonomic Control Techniques | 99 |
| 4.6 Simple Geometric Motion Planning..... | 101 |
| 4.6.1 Partial Reconfiguration Algorithm..... | 102 |
| 4.6.2 Simulation of Partial Reconfiguration Algorithm..... | 104 |
| 4.6.3 Complete Reconfiguration Algorithm..... | 106 |
| 4.6.4 Simulation of Complete Reconfiguration Algorithm..... | 110 |
| 4.6.5 Reachability of All orientations | 112 |
| 4.7 Other Comments | 116 |
| 5. Concluding Remarks | 118 |
| Bibliography..... | 121 |
| Appendix A | 128 |
| Appendix B | 155 |

LIST OF TABLES

| | |
|--|----|
| Table 1. Mmax for different values of n and L/r using long links ($\beta=0$, $\gamma=90$ degrees)... | 10 |
| Table 2. M_{max} for configurations of common lengths using either short or long links. | 13 |
| Table 3. M_{max} for configurations of equal length using permutations of | 13 |
| Table 4. Results of AMMIS link optimization, sorted in decreasing optimality. | 16 |
| Table 5. Gear tooth forces and effective torque for a typical instrument configuration ($L=14.5\text{mm}$, $r_B=2.0\text{mm}$, $D=6.35\text{mm}$, $L_B=2.7\text{mm}$, $r_{TIP}=10\text{mm}$, $F_{tip}=5\text{N}$, Diametral Pitch = 64). | 23 |
| Table 6. Optimum gear thicknesses. | 27 |
| Table 7. Data indicating space requirements and mobility of various robot joint structures and strides. | 47 |
| Table 8. Weighted performance evaluations of the robot configurations operating in open, confined, and mixed environments..... | 48 |
| Table 9. Maxon motor performance (10mm, .75w, plastic planetary gearbox)..... | 70 |
| Table 10. Maxon motor performance (13mm, 1.2w, metal planetary gearbox). | 71 |
| Table 11. Portescap motor performance (13mm, 2.5w, metal planetary gearbox). | 71 |
| Table 12. Portescap motor performance (17mm, 3.2w, metal planetary gearbox). | 71 |

LIST OF FIGURES

| | |
|---|----|
| Figure 1 - AMMIS Kinematic Structure | 8 |
| Figure 2 - Long and short link diagrams | 11 |
| Figure 3. Reachable and Dexterous Workspaces | 14 |
| Figure 4. The DALSA Mechanism. | 18 |
| Figure 5. Exploded view of DALSA linkage. | 19 |
| Figure 6. DALSA mechanism Free-Body-Diagrams. | 20 |
| Figure 7. The Biped Climbing Adaptable Robot (RAMR1) scaling a vertical surface. . | 31 |
| Figure 8. Space requirement typified by cross sectional area required for walking. | 37 |
| Figure 9. The Simple Biped robot. | 38 |
| Figure 10. Mobility of evaluation of the simple biped structure. | 39 |
| Figure 11. Space requirements of the simple biped structure during flipping and crawling strides. | 39 |
| Figure 12. Simple biped and two-legged biped attempting to traverse a 270° corner. | 40 |
| Figure 13. Mobility evaluation of the revolute hip two legged biped. | 41 |
| Figure 14. Space requirements of the revolute hip two-legged biped during flipping and crawling strides. | 41 |
| Figure 15. Locomotion of a Two-Legged Biped robot using a prismatic hip joint. | 42 |
| Figure 16. Mobility evaluation of the prismatic hip two-legged biped robot. | 43 |
| Figure 17. Space requirements of the prismatic hip two-legged biped during flipping and crawling strides. | 43 |
| Figure 18. A hybrid revolute and prismatic joint shown assembled and in exploded view. | 44 |
| Figure 19. The hybrid revolute and prismatic joint shown in several positions. | 45 |
| Figure 20. Joint and link structure of the Two-Legged Biped with coupled DOF. | 50 |
| Figure 21. Illustrated pictures of the Biped Climbing robot with a revolute hip joint. | 52 |

| | |
|--|-----|
| Figure 22. An exploded diagram of the Biped Climbing Robot with Smart Robotic Feet (Dangi, Stam, et al. 2000). | 53 |
| Figure 23. Belt drive system coupling articulation of Ankle #1 and the hip joint. | 54 |
| Figure 24. Ankle #1 and the differential. | 55 |
| Figure 25. The worm drive at joint 4. | 56 |
| Figure 26. Free body diagrams of the climbing robot supported by Foot #1 on a vertical surface (some forces omitted for clarity). | 58 |
| Figure 27. Free body diagrams of the climbing robot supported by Foot #2 on a vertical surface (some forces omitted for clarity). | 61 |
| Figure 28. Diagram of the climbing robot steering via Foot #1 on a vertical surface. | 64 |
| Figure 29. Diagram of robot Boundary Conditions used for Structural Analysis..... | 73 |
| Figure 30. FEM analysis of Link 3 subjected to maximum loading. | 75 |
| Figure 31. FEM analysis of Link 4 subjected to maximum loading. | 77 |
| Figure 32. FEM analysis of Link 5 subjected to maximum loading. | 77 |
| Figure 33. Biped climbing a vertical surface. Start position and beginning of motion. .. | 79 |
| Figure 34. Biped climbing a vertical surface, halfway through step..... | 79 |
| Figure 35. Biped climbing a vertical surface. Near end of step and final position. | 79 |
| Figure 36. Spherobot Mobile Robot..... | 84 |
| Figure 37. Nonholonomic constraints: parallel parking..... | 85 |
| Figure 38. Spherobot Coordinate System. | 87 |
| Figure 39. Spherobot Orientation Variables. | 88 |
| Figure 40. Partial Reconfiguration of the sphere. | 102 |
| Figure 41. Partial reconfiguration simulation: top view. | 104 |
| Figure 42. Partial reconfiguration simulation: chart view..... | 105 |
| Figure 43. Complete reconfiguration process, top view. | 107 |
| Figure 44. Complete reconfiguration process, perspective view. | 108 |

| | |
|--|-----|
| Figure 45. Complete reconfiguration simulation: top view. | 111 |
| Figure 46. Complete reconfiguration simulation: chart view. | 112 |
| Figure 47. Paths of point F as $\Delta\alpha$ varies. from Error! Objects cannot be created from editing field codes. to Error! Objects cannot be created from editing field codes. | 113 |
| Figure 48. Net sphere re-orientation $\Delta\phi_G$ as a function of Error! Objects cannot be created from editing field codes. for Error! Objects cannot be created from editing field codes. and $r = 0.25, 0.5, 1.0, 2.0, 5.0, 10.0$ | 114 |
| Figure 49. Counter Clock-Wise (CCW) and alternate Clock-Wise (CW) and paths for complete reconfiguration..... | 115 |
| Figure 50. Assembled view of DALSA surgical mechanism (sheet 1). | 129 |
| Figure 51. Exploded view of DALSA surgical mechanism (sheet 2). | 130 |
| Figure 52. DALSA Component: Bevel Gear Pinion (sheet 3). | 131 |
| Figure 53. DALSA Component: Bevel Gear (sheet 4). | 132 |
| Figure 54. DALSA Component: Forceps (sheet 5). | 133 |
| Figure 55. DALSA Component: Spur Gear with 48DP and 12 teeth (sheet 6). | 134 |
| Figure 56. DALSA Component: Base Link (sheet 7). | 135 |
| Figure 57. DALSA Component: Drive Shaft (sheet 8). | 136 |
| Figure 58. DALSA Component: Tip Link (sheet 9). | 137 |
| Figure 59. DALSA Component: Tip Retainer Plate (sheet 10). | 138 |
| Figure 60. DALSA Component: drive link (sheet 11). | 139 |
| Figure 61. DALSA Component: Idler Pulley (sheet 12). | 140 |
| Figure 62. DALSA component: driveshaft retaining plate (sheet 13). | 141 |
| Figure 63. DALSA Component: Spur Gear 64DP, 16 Teeth (sheet 14). | 142 |
| Figure 64. DALSA Component: Pin (sheet 15). | 143 |
| Figure 65. DALSA Component: Alignment Pin (sheet 16). | 144 |
| Figure 66. DALSA Component: Drag Link (sheet 17). | 145 |

| | |
|--|-----|
| Figure 67. DALSA Component: Swivel (sheet 18). | 146 |
| Figure 68. DALSA Component: Spur Gear 64DP, 12 Tooth (sheet 19). | 147 |
| Figure 69. DALSA Component: Spur Gear 64DP, 16 Tooth, .075ID (sheet 20). | 148 |
| Figure 70. DALSA Component: Forceps Jaw (sheet 21)..... | 149 |
| Figure 71. DALSA Component: Tip Retainer Spacer (sheet 22). | 150 |
| Figure 72. DALSA Component: Drive Shaft Spacer (sheet 23). | 151 |
| Figure 73. DALSA Component: Bevel Gear Spacer (sheet 24). | 152 |
| Figure 74. DALSA Component: Drive Shaft Extension (sheet 25). | 153 |
| Figure 75. DALSA Component: Drive Shaft Coupler (sheet 26). | 154 |
| Figure 76. Exploded View of the RAMR1 climbing robot..... | 156 |
| Figure 77. RAMR1 Component: Differential Housing..... | 157 |
| Figure 78. RAMR1 Component: Bracket for Foot #1. | 158 |
| Figure 79. RAMR1 Component: Bracket for Motor #1..... | 159 |
| Figure 80. RAMR1 Component: Link #3. | 160 |
| Figure 81. RAMR1 Component: Link #5 | 161 |
| Figure 82. RAMR1 Component: Link 4 Bracket for Motors #2 and #3..... | 162 |
| Figure 83. RAMR1 Component: Link 4 Motor Bracket Coupling Plate | 163 |
| Figure 84. RAMR1 Component: Pin for Joint #3. | 164 |
| Figure 85. RAMR1 Component: Pin for Joint #4. | 165 |
| Figure 86. RAMR1 Component: Link 3 Support Strut..... | 166 |
| Figure 87. RAMR1 Component: Final SRF Suction Block Design. | 167 |
| Figure 88. RAMR1 Component: Early SRF Suction Block Design. | 168 |
| Figure 89. RAMR1 Component: Modified Worm..... | 169 |

LIST OF ABBREVIATIONS

1. AMMIS – Articulated Manipulator for Minimally Invasive Surgery
2. CCW – Counter Clock Wise
3. CW – Clock Wise
4. DALSA – Dexterous Articulated Linkage for Surgical Applications
5. DOF – Degree Of Freedom
6. DP – Diametral Pitch of gear
7. FBD – Free Body Diagram
8. FEA – Finite Element Analysis
9. MIS – Minimally Invasive Surgery
10. mNm – Torque unit of milli Newton meter
11. MPC – Maximum Power Consumption of DC motors
12. OD – Outside Diameter
13. PA – Pressure Angle of gear tooth profile
14. PLC – Package Length Constraint of DC motor
15. RAMR – Reconfigurable Adaptable Micro Robot
16. SEA – Super Elastic Alloy
17. SLSF – Shaft Load Safety Factor of DC motor
18. TSF – Torque Safety Factor of DC motor

1. Introduction

1.1 A New Era

During the twentieth century, an era of robotics was born from dreams and necessity. In their earliest conception, robots were imagined as humanoid devices that would serve people and relieve them of laborious activities (Asimov 1940; Capek 1923). Despite this creative view of robotics, the technology to implement them did not yet exist. It was necessity that actually spurred the innovation leading to the first robotics system. Designed to manipulate radioactive materials at Argonne National Laboratories during World War II (Goertz and Thompson 1954), this first master-slave system integrated mechanisms with parallel kinematics, DC motors, and analog controllers to create position control and force reflection. This project helped motivate numerous researchers to pursue dreams of robotic systems with improved dexterity, control, and repeatability.

1.2 Objectives

Expected productivity gains and improved work environments are primary motivations for implementing robots in manufacturing. Robots have been able to achieve these improvements because they are designed to perform a range of repetitive actions with greater precision, repeatability, and speed than humans. These capabilities are the result of several decades of research on manipulation, mobility, and control of robotic systems. Further expansion of robotics is likewise dependent on continued research in these areas. Since all robots are constrained by available space, weight, power, and computational resources, achieving an optimal balance of these constraints and desired performance is a significant challenge. This is especially true when new applications are becoming increasingly constrained.

In this dissertation, the objective is to achieve new and innovative solutions in design and control for state-of-the-art robotic applications where constraints on space, weight, power, and computational ability are both substantial and critical. This is achieved through the design and control of constrained robotic mechanisms for enhanced dexterity and superior mobility. Several cutting-edge applications of robotics are especially selected to emphasize these issues.

To best address dexterity in a constrained environment, a dexterous instrument for Minimally Invasive Surgery (MIS) is designed to provide dexterity, reachability, and load capacity not yet achieved by other instruments. Space constraints are again addressed in conjunction with mobility in the design of a miniature climbing-robot for urban environments. The resulting robot is the smallest of its kind to date and provides very formidable design constraints on space, weight, and power usage. Mobility is further examined from a controls approach in the design of a spherical reconnaissance robot. Unlike the climbing robot, which possesses relatively straightforward kinematics, the spherical robot has non-linear nonholonomic rolling constraints, which prohibit the application of traditional control techniques. Unlike existing techniques in the literature that are not computationally effective, a very efficient approach is devised for planning the motion of the spherical robot by exploiting fundamental motions created by a unique coordinate system defined on the surface of the sphere. A summary of the document structure follows.

1.3 Document Structure

The structure of the dissertation is now presented. Design and control of constrained robotic mechanisms for enhanced dexterity and mobility is addressed via several state-of-the-art applications of robotics. To best address dexterity and reachability in a

constrained environment, a dexterous instrument for Minimally Invasive Surgery (MIS) is designed in Chapter 2. Space constraints are again addressed in conjunction with enhanced mobility in the design of a miniature climbing-robot for urban environments in Chapter 3. Mobility is further address from a controls approach in the design of a control strategy for a spherical reconnaissance robot with extremely non-linear nonholonomic rolling constraints in Chapter 4.

In each of the aforementioned chapters, a motivational statement and review of specifically relevant literature is presented for each of these systems. The design process, associated analysis, optimization, and proof of concept are also presented. At the end of each chapter, a brief statement about the accomplishments in dexterity and mobility is made. Final concluding remarks summarizing these accomplishments are presented in Chapter 5. Appendix A contains design drawings for the surgical mechanism, Appendix B contains design drawings for the climbing robot, and Appendix C contains details of the load analysis conducted on the climbing robot in Chapter 3.

2. A Surgical Mechanism with Enhanced Dexterity and Reachability

2.1 Motivation

Since the late 1980s, minimally invasive surgery has gained widespread acceptance because of the significant advantages realized by the patient in the form of reduced trauma, recovery time, and procedural costs. Despite growing demand, however, fewer new Minimally Invasive Surgical (MIS) procedures are being developed. This can be attributed to the fact that the skill required to perform advanced procedures is beyond the ability of most surgeons, given the current level of technology available. Dexterous instruments can help reverse this trend.

Current state-of-the-art instruments in MIS provide single joint articulation of the tip up to 90 degrees (Ethicon Endo Surgeries 1998; Pivotal Medical Innovations 1996). Despite tip articulation, they are incapable of placing sutures with arbitrary orientation at surgical sites. We propose to alleviate dexterity and reachability inadequacies of current MIS instruments through the development of the Dexterous Articulated Linkage for Surgical Applications (DALSA).

The DALSA mechanism is a geared serial link mechanism that can be coupled to form either a manual or robotic instrument. Design of DALSA highlights the impact of space and operational constraints on robotic systems that must achieve a desired workspace, load capacity, and dexterity. DALSA can be appreciated in light of the following stringent constraints imposed by MIS:

1. **Instrument Size:** A port on the patient body, which typically varies between 2 and 15mm diameter (Rosen and Carlton 1997; Schurr, Melzer, et al. 1993; Yuan, Lee, et al. 1997), determines the size of the mechanism. Smaller ports reduce scarring, but larger ports allow instrument designs with greater load capacity and dexterity. The common 10mm port was selected for DALSA design.

2. **Articulation and Tip Rotation:** Difficult tasks in MIS, such as suturing, require that the tip of the instrument approach tissue at arbitrary orientation and perform surgical tasks. Given the four DOF inherent to a port, dexterity necessitates that two additional DOF are provided. In DALSA, these two DOF are provided via 180° bi-directional tip articulation and unlimited rotation about the articulated longitudinal axis. Articulation is divided among several links, to provide encircling capability and improved reachability.

3. **Load Capacity.** The desired load capacity of the instrument is dictated by the intended surgical procedures. For suturing, the instrument will drive a suture through tissue, displace the tissue for alignment purposes, and pull the suture material for knot tying. The pull-out strength of a suture in tissue varies between 2N and 15N (Bunt and Moore 1993; Trowbridge, Lawford, et al. 1989). The driving force of a needle through soft tissue is much less, on the order of 3N (Seki 1988). A driving force of 5N at the tip of a 1cm needle was targeted for DALSA design.

4. **Durability and Reliability.** The necessity for reliable instruments during surgery is obvious.

This chapter is organized as follows. In section 2.2, we examine state-of-the-art surgical instrumentation. In section 2.3, we present and optimize the articulation component of DALSA. In section 2.4, we integrate tip rotation and actuation with the articulated

linkage to complete DALSA design. In the same section we evaluate its performance and optimize its structure. In section 2.5 we address manufacturability and cost considerations. Final observations about the design of dexterous robotic mechanisms are provided in section 2.6.

2.2 Related Research

MIS instruments are comprised of a slender rigid tube and an end-effector. The instruments are inserted through a port in the human body that constrains the motion of the end-effector by allowing it to move with four DOF. These DOF are insertion depth and the three axis of rotation about the insertion point. Numerous approaches have been adopted to provide greater freedom of movement to the end-effector. The simplest of these consist of a single revolute joint supporting the end-effector. Such mechanisms are typically actuated by push-pull rods and, or, four bar linkages (Faraz and Payandeh 1997; Hassler, Murray, et al. 1994; Jaeger 1987; Wales, Paraschac, et al. 1997; Zvenyatsky, Aranyi, et al. 1995). A mechanism using bevel gears for articulation has also been developed (Knoepfler 1993). Including the four DOF inherent to a port, these mechanism allow the end-effector to have five DOF, which is inadequate for full dexterity.

Other approaches to articulation use a serial chain of links with revolute joints. Distributing articulation among several joints decreases sharp bends in the instrument and is less harmful to cables or wires routed throughout the mechanism. One such device (Huitema 1998) uses a flexible neck formed by five vertebrae and integral actuator bands for steering. This device only provides one articulation DOF and is inadequate for full dexterity. Other serial link devices with similar limitations use lead screws (Faraz and Payandeh 1997) or five bar linkages (Guo, Qian, et al. 1992; Zhang, Guo, et al. 1992). A

steerable channel (Schurr, Melzer, et al. 1993), actuated by opposing tendons routed along the channel, provides articulation in two directions as well as rotation of the end-effector. Though the instrument provides the necessary DOF for complete dexterity, it lacks sufficient rigidity. In an improved design, a chain of five four bar linkages was used to develop a trunk mechanism with a central passage for end effector operation (Mueglitz, Kunad, et al. 1993; Schurr, Melzer, et al. 1993). The trunk provides excellent dexterity via 180° articulation and unlimited tip rotation for full dexterity. However, it suffers from two drawbacks: the long chain of links creates large actuation forces reducing controllability, and the Super Elastic Alloy (SEA) tube used for driving tip rotation is unreliable when subjected to large cyclic strains in articulated configurations (Plietsch 1997). A device using four serial links, AMMIS, implements planetary gearing with unity ratio to drive successive links for $\pm 180^\circ$ articulation distributed equally amongst the links (Mukherjee, Minor, et al. 1998). Starting with the AMMIS structure, DALSA adds additional DOF for full dexterity and optimizes the mechanical structure. It provides the same dexterity as the trunk mechanism but has improved rigidity and reduced force magnification. The gearing in DALSA introduces backlash which must be restricted during manufacturing.

Among other instruments, tendon actuated Stuart-platforms are used for end-effector dexterity (Cohn, Crawford, et al. 1995; Schenker, Das, et al. 1995). The first of these lacks repeatability and provides less than 90° articulation, which makes it unsuitable for dexterous tip placement. The second device is larger ($\phi 25\text{mm}$) and uses a serial chain of tendon actuated links supporting a wrist. This device provides high accuracy and minimal backlash, but its large size prohibits MIS applications. A number of dexterous mechanisms can be found in industrial applications, but it is doubtful if they can be effectively miniaturized for MIS (Lande and David 1981; Milenkovic 1987; Rosheim 1987; Stanisic and Duta 1990; Susnjara and Fleck 1982).

2.3 Design of an Articulated Mechanism

2.3.1 Kinematic Structure

In this section, we discuss the articulation of DALSA, which is provided by the Articulated Manipulator for Minimally Invasive Surgery (AMMIS) (Mukherjee, Minor, et al. 1998). AMMIS is a serial concatenation of geared linkages where every link, except the last, is both a driven-link and a driving-link. The last link is only a driven-link. This idea is used to transfer power from a single actuator to simultaneously articulate each link. This idea is realized by the four-link AMMIS in Figure 1, where the driving gear is located at the base; Link-0.

Describing AMMIS in terms of planetary gearing terminology, it suffices to say that each link in AMMIS functions as a carrier arm and as a sun. Link-1 is a carrier for planetary Gears 4 and 5, and its motion driven by Gear-1 produces rotation of the planets since

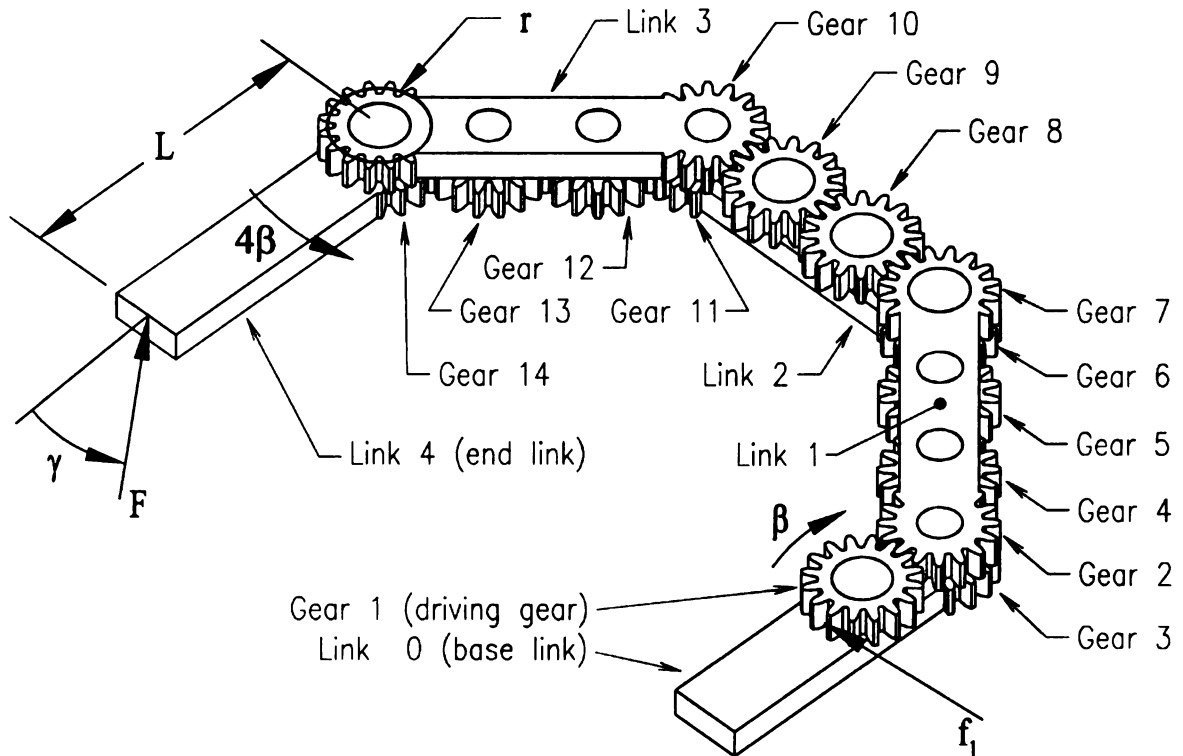


Figure 1 - AMMIS Kinematic Structure

Gear 3, acting as a sun, is stationary. The successive link, Link-2, is then driven by the rotation of planet Gear 5 and sun Gear-7 integral to Link-1. Each successive set of link and gears functions similarly. Unity gear ratio between planets and suns, and even number of planets, produces identical relative motion between each link. A net rotation of 4β of the fourth link occurs for β rotation of Gear-1.

2.3.2 Input-Output Force Relationship

2.3.2.1 AMMIS with arbitrary articulation and load orientation

We study the input-output force relationship to determine the magnitude of the forces required to drive AMMIS. If these forces are large, they will lead to failure of the miniature components. In addition, actuation of the mechanism will not be ergonomically suitable

Consider the free-body diagrams of the last three links of an n -link AMMIS for an articulation angle β . Let F denote the tip force exerted by AMMIS acting at an arbitrary angle γ . For $i=1,2,\dots,n$, let P_i , acting at an angle of α_i , denote the pin force at the point of articulation and f_i denote the driving force of the i -th link. Ignore gear pressure angles and assume common gear pitch radii, r . The static equilibrium conditions for the last three links are,

$$\begin{aligned} P_n \cos \alpha_n - F \cos \gamma - f_n \sin \beta &= 0 \\ P_n \sin \alpha_n - F \sin \gamma - f_n \cos \beta &= 0 \\ f_n r - FL \sin \gamma &= 0 \end{aligned} \tag{2.1}$$

$$\begin{aligned} P_{n-1} \cos \alpha_{n-1} - P_n \cos(\beta + \alpha_n) - f_{n-1} \sin \beta &= 0 \\ P_{n-1} \sin \alpha_{n-1} - P_n \sin(\beta + \alpha_n) - f_{n-1} \cos \beta &= 0 \\ 6P_n r \sin(\beta + \alpha_n) - 4f_n r - f_{n-1} r &= 0 \end{aligned} \tag{2.2}$$

$$\begin{aligned}
P_{n-2} \cos \alpha_{n-2} - P_{n-1} \cos(\beta + \alpha_{n-1}) - f_{n-2} \sin \beta - f_n \sin \beta &= 0 \\
P_{n-2} \sin \alpha_{n-2} - P_{n-1} \sin(\beta + \alpha_{n-1}) - f_{n-2} \cos \beta - f_n \cos \beta &= 0 \\
6P_{n-1}r \sin(\beta + \alpha_{n-1}) - f_n r(6 \cos \beta + 1) - 4f_{n-1}r - f_{n-2}r &= 0
\end{aligned} \tag{2.3}$$

Equations (2.1) and (2.2) are used to solve for f_n , α_n , P_n , and then f_{n-1} , α_{n-1} , P_{n-1} . Subsequently Eq. (2.3) can be used recursively to solve for the unknown forces of the k -th link, $k=n-2, n-3, \dots, 2, 1$, in the following manner:

$$\begin{aligned}
f_k &= -4f_{k+1} + 6P_{k+1} \sin(\beta + \alpha_{k+1}) - f_{k+2}(6 \cos \beta + 1) \\
\alpha_k &= \tan^{-1} \left[\frac{f_k \cos \beta + P_{k+1} \sin(\beta + \alpha_{k+1}) - f_{k+2} \cos \beta}{f_k \sin \beta + P_{k+1} \cos(\beta + \alpha_{k+1}) - f_{k+2} \sin \beta} \right] \\
P_k &= \pm \sqrt{f_k^2 + P_{k+1}^2 + f_{k+2}^2 + 2f_k P_{k+1} \sin(2\beta + \alpha_{k+1}) - 2f_k f_{k+2} \cos 2\beta - 2P_{k+1} f_{k+2} \sin \alpha_{k+1}}
\end{aligned} \tag{2.4}$$

Force magnification in AMMIS is denoted by $M = (f_1 / F)$. Numerical simulations were used to compute M for different values of β , γ , n , and L/r ratio. The following observations were made:

1. M is maximum at $\beta=0$ and $\gamma=\pm 90^\circ$,
2. The maximum force magnification, M_{max} , varies nonlinearly with n ;
3. M_{max} is independent of r , but linearly proportional to L/r .

The first and third observations are intuitive, but the second is not. To quantify the nonlinear relationship between M_{max} and n , we construct Table 1. From the data therein, we deduce $M_{max}=3n^2+2n$ when $L/r=5$ and $M_{max}=3n^2+3n$ when $L/r=6$. The nonlinear relationship can be attributed to the fact that M_{max} increases as the number of articulated segments increase, even when the total length of AMMIS is constant. This is investigated in the next section.

Table 1. M_{max} for different values of n and L/r using long links ($\beta=0$, $\gamma=90$ degrees)

| | n=2 | n=3 | n=4 | N=5 | n=6 |
|---------|-----|-----|-----|-----|-----|
| $L/r=5$ | 16 | 33 | 56 | 85 | 120 |
| $L/r=6$ | 18 | 36 | 60 | 90 | 126 |

2.3.2.2 AMMIS with fixed length

To change the number of links of AMMIS without changing its total length, we introduce the "short link", shown in Figure 2 adjacent to a normal link. The short link eliminates the intermediate gears, maintains the direction of articulation, and reduces the effective length from 6 to 2 pitch radii. Every normal link can be replaced with three short links without changing the total length of AMMIS.

AMMIS with 2, 3, and 4 links were studied. All links, except the last, were replaced by short links, resulting in 4, 7 and 10 link configurations. The last link was not replaced since it should have sufficient length to support an end-effector. Force magnification for these configurations can be seen in Table 2 with two variations of the last link; $L=5r$ and $L=6r$. The results indicate that M_{max} is linearly proportional to the number of links when the total length of AMMIS is kept constant; irrespective of the last link length. In the case where $L=5r$, $M_{max}=33$ for 3 links and 77 for 7 links. For $L=6r$, $M_{max}=60$ for 4 links and 150 for 10 links. This result is not intuitive.

Also consider force magnification when the normal links are partially replaced with short links. This will determine whether M_{max} depends upon the relative location of the short

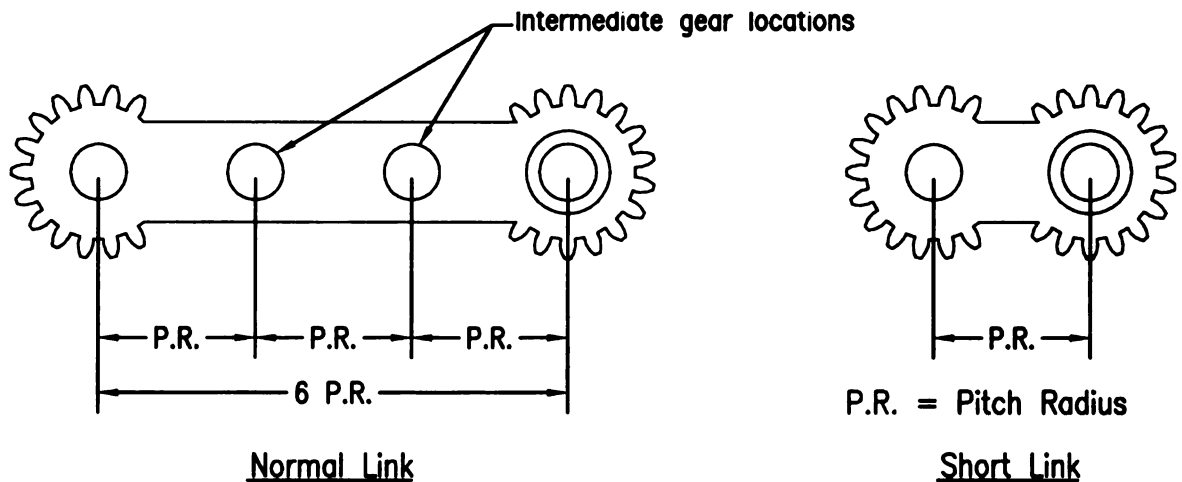


Figure 2 - Long and short link diagrams

links in the mechanism. We consider variations of an AMMIS initially with three normal links and an end link. Nineteen variations are possible and are shown in Table 3, for $L=6r$. The data, sorted in the order of increasing M_{max} , reveals:

s

19. M_{max} is the least for the four-link configuration, followed by the six-link configurations, and then by eight and ten-link configurations.
20. Data in Table 2 indicates M_{max} is not quite proportional to the number of links - it is dependent on the relative position of the short and normal links. For example, for $n=6$, the ten variations in the link configuration produce M_{max} varying between 78 and 102.
21. For a given n , M_{max} is lower for link configurations with normal links closer to the base. The ten configurations for $n=6$ and the seven configurations for $n=8$ support this conclusion.

Table 2. M_{max} for configurations of common lengths using either short or long links.

| Link Configuration | | M_{max} $L=5r$ | M_{max} $L=6r$ |
|------------------------|--------|---------------------|---------------------|
| 6r, L | (n=2) | 16 | 18 |
| 2r,2r,2r,L | (n=4) | 32 | 36 |
| 6r,6r,L | (n=3) | 33 | 36 |
| 2r,2r,2r,2r,2r,2r,L | (n=7) | 77 | 84 |
| 6r,6r,6r,L | (n=4) | 56 | 60 |
| 2r,2r,2r,2r,2r,2r,2r,L | (n=10) | 140 | 150 |

Table 3. M_{max} for configurations of equal length using permutations of short and long links.

| Link Configuration | | M_{max} $L=6r$ |
|------------------------|--------|---------------------|
| 6r,6r,6r,L | (n=4) | 60 |
| 6r,6r,2r,2r,2r,L | (n=6) | 78 |
| 6r,2r,6r,2r,2r,L | (n=6) | 82 |
| 6r,2r,2r,6r,2r,L | (n=6) | 86 |
| 2r,6r,6r,2r,2r,L | (n=6) | 86 |
| 6r,2r,2r,2r,6r,L | (n=6) | 90 |
| 2r,6r,2r,6r,2r,L | (n=6) | 90 |
| 2r,6r,2r,2r,6r,L | (n=6) | 94 |
| 2r,2r,6r,6r,2r,L | (n=6) | 94 |
| 2r,2r,6r,2r,6r,L | (n=6) | 98 |
| 2r,2r,2r,6r,6r,L | (n=6) | 102 |
| 6r,2r,2r,2r,2r,2r,L | (n=8) | 108 |
| 2r,6r,2r,2r,2r,2r,L | (n=8) | 112 |
| 2r,2r,6r,2r,2r,2r,L | (n=8) | 116 |
| 2r,2r,2r,6r,2r,2r,L | (n=8) | 120 |
| 2r,2r,2r,2r,6r,2r,L | (n=8) | 124 |
| 2r,2r,2r,2r,2r,6r,L | (n=8) | 128 |
| 2r,2r,2r,2r,2r,6r,L | (n=8) | 132 |
| 2r,2r,2r,2r,2r,2r,2r,L | (n=10) | 150 |

2.3.3 Optimization of the AMMIS Link Configuration

We select several criteria for optimizing the AMMIS link configuration using the perspectives of a design engineer and a surgeon. These criteria are quantified using cost functions (Arora 1989) described below:

1. **Workspace and Dexterous Workspace:** Workspace is the region that the end-effector can reach and dexterous workspace is the sub-space that can be reached with all orientations (Craig 1989). An MIS instrument should have a large and dexterous workspace. For simplicity, we consider l_0 , θ , and β in Figure 3 to compute both workspaces by area instead of volume. Examination of Figure 3 and the restriction imposed on β obviates that the tip will not be able to reach any point in the workspace with all orientations. For this reason the definition of dexterous workspace is relaxed

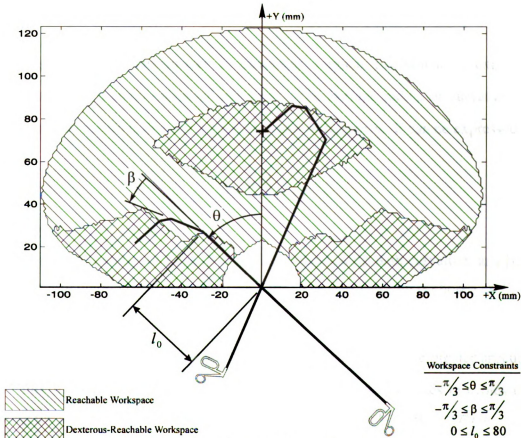


Figure 3. Reachable and Dexterous Workspaces

to include regions that provide 270° range of end-effector orientation. Reachable and dexterous workspaces are denoted by A_r and A_d , respectively; and their cost functions are $C_1=A_r$ and $C_2=A_d$. A similar criteria was used by (Faraz and Payandeh 1997).

2. **Force Magnification:** The negative effects of large force magnification were outlined in the previous section. The cost function for force magnification will be $C_3=M_{max}$.
3. **Backlash:** Backlash occurs in mechanisms due to clearance allowances that assure smooth operation. It can degrade tip placement, accuracy, and repeatability. Backlash depends on the number of meshing gears and for AMMIS the cost function will be $C_4 = n_s + 3n_n$, where n_s and n_n are the number of short and long links, respectively.
4. **Average tip path curvature:** A dexterous surgical instrument is expected to articulate with a small radius of curvature. The average radius of curvature of the path trace by the tip is therefor a good indicator of dexterity. It can be expressed as

$$\bar{\rho} = \frac{n}{\pi} \int_0^{\pi/n} \rho d\beta \quad (2.5)$$

where n is the number of links, ρ is the instantaneous tip path curvature, and β is the relative articulation between successive links. The cost function is chosen as $C_5 = \bar{\rho}$.

5. **Maximum articulation angle per link:** Fewer links will require greater articulation per link for a net 180° articulation and adversely increases stresses in cables routed along the mechanism. The cost function is represented by $C_6 = \beta_{max} = \pi / n$.

We limit our search among configurations with two, three, and four links where the last link is a normal link supporting a surgical tool. The optimal configuration is obtained by finding the minimum weighted sum of the normalized cost functions. The choice of weights depend upon the desired characteristics of the surgical instrument, but are somewhat subjective. The weighted sum is described as

$$CF = -w_1 C_1^N - w_2 C_2^N + w_3 C_3^N + w_4 C_4^N + w_5 C_5^N + w_6 C_6^N \quad (2.6)$$

where w_i and C_i^N , $i=1,...,6$ are the weights and normalized cost functions, respectively, corresponding to the elementary cost function C_i , $i=1,...,6$. The idea behind the optimization process is to choose the link configuration that has large values of C_1^N and C_2^N , and small values of C_3^N , C_4^N , C_5^N and C_6^N . For the task of suturing, the weights are chosen as

$$w_1 = 8.0 \quad w_2 = 6.0 \quad w_3 = 4.0 \quad w_4 = 3.0 \quad w_5 = 1.0 \quad w_6 = 1.0 \quad (2.7)$$

The maximum weights were assigned to dexterous workspace and force magnification.

Table 4. Results of AMMIS link optimization, sorted in decreasing optimality.

| Rank | Link Configuration | Individual Cost functions | | | | | | Net Cost |
|------|--------------------|---------------------------|---------|---------|---------|---------|---------|----------|
| | | C_1^N | C_2^N | C_3^N | C_4^N | C_5^N | C_6^N | |
| 1 | 6r,2r,L | 0.30 | 0.24 | 0.18 | 0.20 | 0.21 | 0.28 | -1.98 |
| 2 | 2r,L | 0.25 | 0.17 | 0.09 | 0.05 | 0.15 | 0.42 | -1.93 |
| 3 | 6r,2r,2r,L | 0.32 | 0.26 | 0.26 | 0.25 | 0.23 | 0.21 | -1.92 |
| 4 | 2r,2r,L | 0.26 | 0.19 | 0.16 | 0.10 | 0.18 | 0.28 | -1.83 |
| 5 | 6r,L | 0.26 | 0.22 | 0.12 | 0.15 | 0.21 | 0.42 | -1.79 |
| 6 | 6r,6r,2r,L | 0.33 | 0.31 | 0.32 | 0.35 | 0.30 | 0.21 | -1.65 |
| 7 | 2r,2r,2r,L | 0.26 | 0.22 | 0.24 | 0.15 | 0.20 | 0.21 | -1.57 |
| 8 | 6r,6r,L | 0.27 | 0.29 | 0.24 | 0.30 | 0.30 | 0.28 | -1.46 |
| 9 | 2r,6r,L | 0.23 | 0.24 | 0.21 | 0.20 | 0.26 | 0.28 | -1.30 |
| 10 | 2r,6r,2r,L | 0.26 | 0.26 | 0.29 | 0.25 | 0.27 | 0.21 | -1.30 |
| 11 | 6r,2r,6r,L | 0.27 | 0.32 | 0.34 | 0.35 | 0.31 | 0.21 | -1.14 |
| 12 | 6r,6r,6r,L | 0.27 | 0.36 | 0.39 | 0.45 | 0.38 | 0.21 | -0.86 |
| 13 | 2r,2r,6r,L | 0.22 | 0.27 | 0.32 | 0.25 | 0.29 | 0.21 | -0.82 |
| 14 | 2r,6r,6r,L | 0.22 | 0.31 | 0.37 | 0.35 | 0.35 | 0.21 | -0.55 |

Average tip path curvature had the least weight since suturing is typically performed in a small region without gross steering. Optimization results are shown in Table 4, with data sorted in the order of decreasing optimality. The optimum AMMIS is comprised of three links among which the first and second links are normal and short links, respectively. In terms of actual (not normalized) data, this configuration has a workspace of 206cm^2 , dexterous workspace of 72cm^2 , force magnification of 28, backlash resulting from 4 mating gears, average path curvature of 29.4mm , and 60° maximum articulation angle per link.

2.4 Dexterous Articulated Linkage for Surgical Applications

2.4.1 Methodologies Explored

Tip rotation as well as articulation is necessary to position a suture needle in arbitrary orientations. Towards this objective, several methods for tip rotation in articulated configurations were explored (Minor and Mukherjee 1999). These include flexible shafts, miniature motors, hydraulic systems, tendons, and geared mechanisms. Flexible shafts encounter large cyclic stresses: a straight wire core wrapped with multiple layers of wires is too compliant and SEA tubes are prone to failure. Miniature motors of 3 and 5mm diameter are available, but their length and load capacity prohibits their usage. Hydraulic actuators were discounted because of leakage potential, additional hardware requirements, and control complexity. Tendon actuation was considered, but not used due to large actuation and pre-load forces.

Gearing was examined in two scenarios. In the first, a geared reduction unit at the tip of the instrument would reduce the impact of shaft compliance. While load capacity could be increased substantially, the effects of compliance were still appreciable. Alternatively, by placing a third layer of gears along the AMMIS linkage, the exiting compact structure

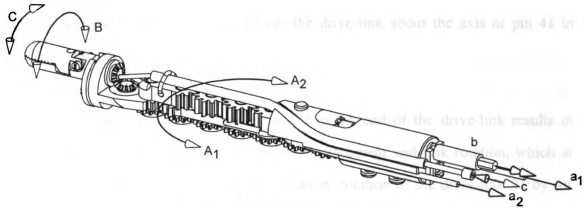


Figure 4. The DALSA Mechanism.

could also be used to transmit power to the tip. Viewed as the best alternative, this method uses very little additional space and allows routing of cables and accessories to the end-effector. The serial chain of gears introduces some backlash, but that can be minimized via tolerance control.

2.4.2 Description of Functionality

To describe our approach for tip rotation, refer to Figure 4. As shown in this figure, DALSA DOF include articulation A_1 and A_2 , tip rotation B , and end-effector actuation, C . Power for these DOF are transmitted through tendons a_1 and a_2 , a rotary shaft b , and a push-pull cable c , respectively. An exploded view of DALSA is shown in Figure 5. Rotation of the forceps at the tip of the instrument is accomplished via rotation of the drive shaft 17, which drives bevel gears 6 and 5. Bevel gear 5 is coupled to Gear 35 and drives gears 34 through 28. This ultimately drives bevel gear 4 and forceps 9. Actuation of the forceps is achieved by push-pull cable 1. Push-pull actuation of the cable pivots the upper jaw about the axis of screw 8. The cable rotates with the forceps and swivels freely via the cylinder 43. Articulation is provided by tendons 23 and 24, which wrap around the idler pulley 22 and around the end of the drive-link 21. They then pass through the holes in the drive-link where they are restrained. Tension applied to tendon

23 displaces the tendon and hence rotates the drive-link about the axis of pin 41 in a clockwise direction.

Wrapping the tendon about the pulley and then the end of the drive-link results in a constant linear relationship between tendon displacement and link rotation, which aids controllability. Identical to the AMMIS actuation, rotation of the drive-link 21 by some angle β causes the subsequent links to articulate by angle β relative to the previous link. Since this is a three-link mechanism, rotation β of the drive-link results in 3β net articulation of the tip-link. In an actual surgical instrument, the base-link 16 will be supported by a 10mm diameter tube, which will be coupled to a handle or motor drive at the exterior end. The tube will be aligned with the base-link by pin 42 and retained by the screws 36.

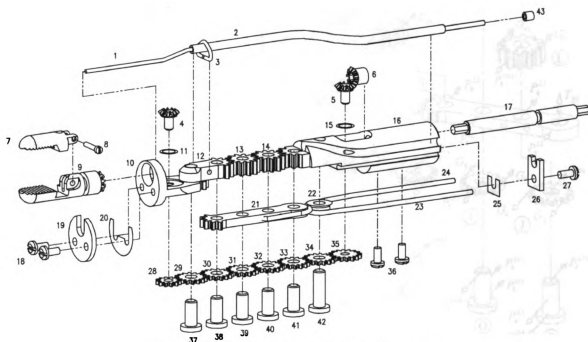


Figure 5. Exploded view of DALSA linkage.

2.4.3 Force Analysis

In addition to the forces discussed in Section 2.3.2, we consider the forces exerted by the bevel gears and additional gear pack for tip rotation. We examine DALSA in a straight configuration for the sake of simplicity, which is justifiable in light of the results of Section 3.2. Considering the free-body-diagrams of DALSA, in Figure 6, adopt the following notation,

- P_i^{Gj} force acting between the i^{th} pin and the j^{th} gear
- P_i^{Lj} force acting between the i^{th} pin and the j^{th} link
- G_i force acting on the i^{th} gear tooth.

The load, F_{TIP} , is applied to a needle tip with radius r_{TIP} orientated at angle θ relative to the horizontal plane of the mechanism. The bevel gear force B_T and the torque T_B

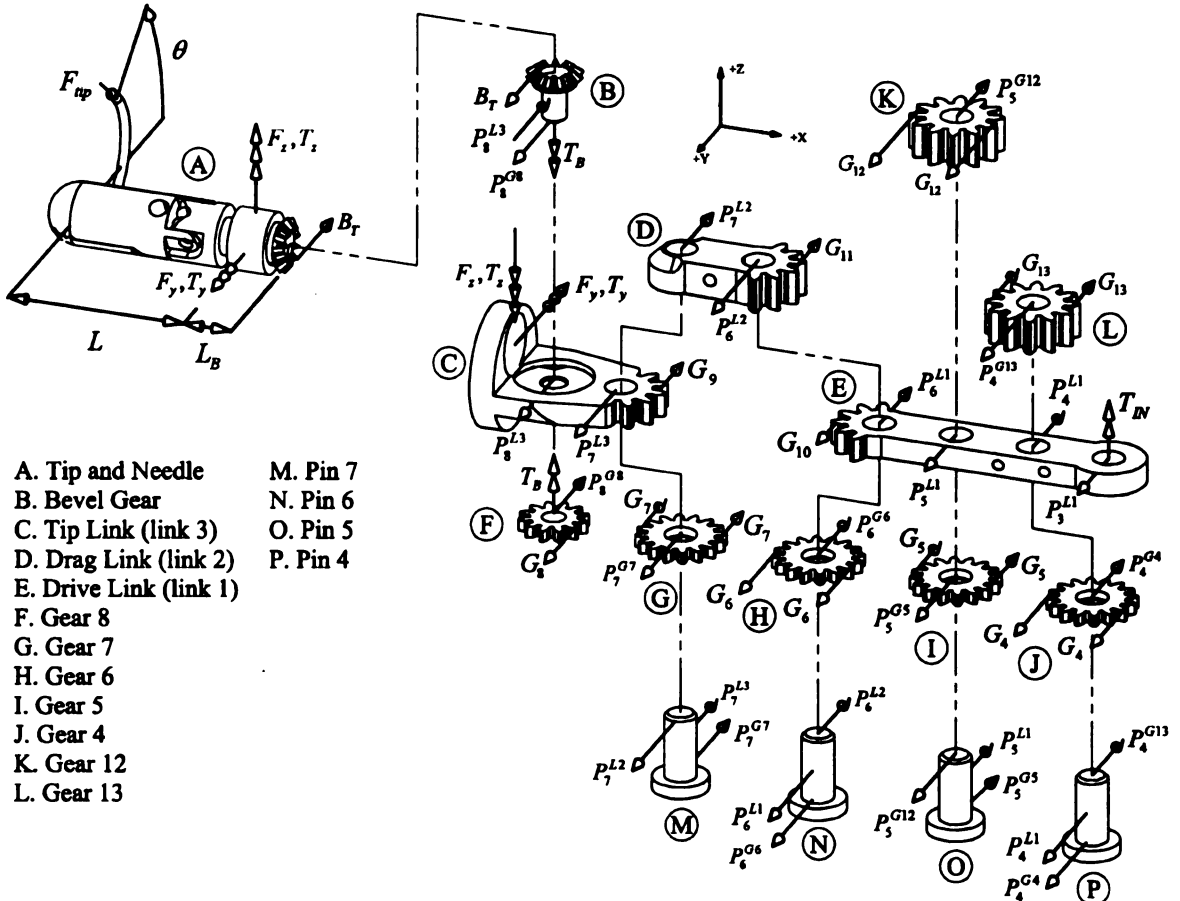


Figure 6. DALSA mechanism Free-Body-Diagrams.

balance the load. Taking moments about the x-axis of the Tip (labeled A), we have,

$$B_T = \frac{r_{TIP}}{r_B} F_{TIP} \quad (2.8)$$

where r_B is the bevel gear pitch radius. We can determine the torque T_B acting on the Bevel Gear (labeled B) as,

$$T_B = B_T r_B = r_{TIP} F_{TIP} \quad (2.9)$$

Neglecting axial and radial separation forces created by the bevel gears, it can be shown that the relevant forces supporting the tip are described by F_y and T_z where,

$$F_y = F_{TIP} \left(\sin(\theta) + \frac{r_{TIP}}{r_B} \right), \quad T_z = F_{TIP} \left(L \sin(\theta) - L_B \frac{r_{TIP}}{r_B} \right) \quad (2.10)$$

and L and L_B are defined in Figure 6. Neglect the contribution of gear pressure angle effects and bending moment and assume that D denotes the pitch diameter of all spur gears, except for gear 8, which is $\frac{12}{16}D$. The bevel gear is coupled to Gear 8 (labeled F) and the torque T_B produces the reaction forces G_8 and P_8^{G8} described by,

$$G_8 = P_8^{G8} = \frac{8}{3} \frac{r_{TIP} F_{TIP}}{D}$$

Gear 8 acts on Gear 7 (labeled G), producing reactions along the lower gear-pack (labeled H, I, J) of the mechanism. This results in forces G_i and P_i^{Gi} for $i=1\dots7$.

Neglecting friction and pressure angles, these forces can be determined as

$$G_i = \frac{8}{3} \frac{r_{TIP} F_{TIP}}{D}, \quad P_i^{Gi} = \frac{16}{3} \frac{r_{TIP} F_{TIP}}{D} \quad (2.11)$$

Considering the previously described forces acting on the Tip Link (labeled C), we can show that the forces G_9 and P_7^{L3} acting on the Tip Link are,

$$G_9 = 2 \frac{F_{TIP}}{D} \left[\left(L + L_B + r_B + \frac{11}{8} D \right) \sin(\theta) - \frac{4}{3} r_{TIP} \right] \quad (2.12)$$

$$P_7^{L3} = \frac{2F_{TIP}}{D} \left[\left(L + L_B + r_B + \frac{11}{8} D \right) \sin(\theta) - \frac{8}{3} r_{TIP} \right] \quad (2.13)$$

To determine the forces on the Drag Link (labeled D), we balance the forces on Pin 7 (labeled M) yielding,

$$\begin{aligned} P_7^{L2} &= P_7^{L3} + P_7^{G7} \\ &= 2 \frac{F_{TIP}}{D} \left[\left(L + L_B + r_B + \frac{11}{8} D \right) \sin(\theta) + \frac{1}{7} r_{TIP} \right] \end{aligned} \quad (2.14)$$

Applying force P_7^{L2} to the Drag Link (labeled D), we obtain the driving and support forces G_{11} and P_6^{L2} as,

$$G_{11} = 4 \frac{F_{TIP}}{D} \left(L + L_B + r_B + \frac{11}{8} D \right) \sin(\theta) \quad (2.15)$$

$$P_6^{L2} = 6 \frac{F_{TIP}}{D} \left(L + L_B + r_B + \frac{11}{8} D \right) \sin(\theta) \quad (2.16)$$

The force P_6^{L1} acting on Pin 6 (labeled N) and the Drive Link (labeled E) is

$$P_6^{L1} = P_6^{L2} - P_6^{G6} = 6 \frac{F_{TIP}}{D} \left[\left(L + L_B + r_B + \frac{11}{8} D \right) \sin(\theta) - \frac{16}{18} r_{TIP} \right] \quad (2.17)$$

Since $G_{11} = G_{12} = G_{13}$, we can show that the forces P_5^{L1} and P_4^{L1} acting on the Drive Link are,

$$P_4^{L1} = P_5^{L1} = P_5^{G12} - P_5^{G5} = 8 \frac{F_{TIP}}{D} \left[\left(L + L_B + r_B + \frac{11}{8} D \right) \sin(\theta) - \frac{2}{3} r_{TIP} \right] \quad (2.18)$$

Balancing moments applied to the Drive Link about the axis of T_{IN} , the driving torque is obtained as,

$$\begin{aligned} T_{IN} &= -3.5DG_{10} + 3DP_6^{L1} - 2DP_5^{L1} + DP_4^{L1} \\ &= F_{TIP} \left[\left(3L + 3L_B + 3r_B + \frac{61}{8} D \right) \sin(\theta) - \frac{4}{3} r_{TIP} \right] \end{aligned} \quad (2.19)$$

Forces pertinent to gear design are G_8 , G_9 , G_{11} , and T_{IN} , and are studied at $\theta = -\pi/2$ where the maximum amplitudes occur. Table 5 shows the maximum of these forces and their equivalent torque for typical system parameters. As expected, driving forces are larger near the base of the instrument. The tooth force representing T_{IN} is fictitious since the drive link does not have gear teeth on its driven end, but that force is shown for comparison to the force magnification, M_{max} , introduced in Section 2.3.2.1. Recalling the definition $M_{max}=(f_I/F)$, here we have,

$$M_{max} = \frac{188N}{5N} = 37.6 \quad (2.20)$$

which is larger than $M_{max} = 28$, obtained previously. This can be attributed to the increased tip length resulting from the forceps and gearing for tip rotation.

Table 5. Gear tooth forces and effective torque for a typical instrument configuration ($L=14.5\text{mm}$, $r_B=2.0\text{mm}$, $D=6.35\text{mm}$, $L_B=2.7\text{mm}$, $r_{TIP}=10\text{mm}$, $F_{tip}=5\text{N}$, Diametral Pitch = 64).

| Force Component | Tangential Tooth Force | Effective Torque | Initial Thickness (mm) |
|-----------------|------------------------|------------------|------------------------|
| G_8 | 21.0 N | 66.7 N-mm | 0.97 mm |
| G_9 | -60.0 N | -190 N-mm | 2.76 mm |
| G_{11} | -87.9 N | -279 N-mm | 4.05 mm |
| T_{IN} | -188 N | -597 N-mm | 8.66 mm |

2.4.4 Load Capacity Maximization

Decreased force magnification and optimized gear designs maximize load capacity. Reducing tip-link and forceps length decreases force magnification to the level mentioned above. Efforts to accomplish this include a compact forceps with integrated upper bevel gear, as shown in Figure 6 (labeled A), and a smaller diameter for Gear 8, labeled F. Nonetheless, force magnification is excessive and the gear designs must be optimized to maximize load capacity.

In order to understand how gear design parameters affect tooth capacity, we examine stress characteristics of an involute tooth profile. Based upon AGMA stress formulae, (Shigley and Mischke 1989) the maximum bending stress, σ , occurring at the root of the tooth is described in US units by,

$$\sigma = \frac{W_t K_a}{K_v} \frac{P_d}{F} \frac{K_s K_m K_B}{J} = 8.71 \frac{W_t P_d}{F} \quad (2.21)$$

where W_t is the load, P_d is the Diametral Pitch (DP), F (tooth thickness), $K_a=1.0$ (application factor), $K_v=0.95$ (dynamic loading factor), $K_s=1.0$ (size factor), $K_m=1.3$ (load distribution factor), and $J=0.22$ (geometry factor). To determine tooth capacity, we must first calculate allowable bending stress, which is determined by,

$$\sigma_{all} \leq \frac{S_t K_L}{K_T K_R} \quad (2.22)$$

where S_t is the endurable bending strength, K_L is the life factor, K_T is the temperature factor, and K_R is the reliability factor. We use high strength UNS S42000 stainless steel tempered at 400°F with an ultimate strength of 250ksi (ASM International Handbook Committee 1996) which has an endurance strength of $S_e=69ksi$, assuming 10^7 cycles (Shigley and Mischke 1989). Based on Eq. (2.22), the allowable stress is equivalent to

the endurance limit when we use $K_L=1.0$ (10^7 load cycles), $K_T=1.0$ (operating environments up to 250°F), and $K_r=1.0$ (reliability factor 0.99). Solving Eq.(2.21) for tooth load, W_t , and using $\sigma = 69ksi$ we have,

$$W_t \leq 7924 \frac{F}{P_d} \quad (2.23)$$

Using the original AMMIS tooth profile, 64 Diametral Pitch (DP) and 20° Pressure Angle (PA), the load capacity is $W_t=21.7F$ (N per mm tooth thickness, F). Tooth thickness is calculated to support the corresponding loads, both shown in Table 5. Notice that the face width for T_{IN} is much larger than that required by G_9 at the opposite end of the same link. Application of a tendon drive at T_{IN} eliminates the need for the thicker link at T_{IN} and permits more effective use of the space. Tensile forces on the tendons approach 199N, which is safely within the limits of a 1mm Vectran (Cortland Cable Company 1997) cable with a 800N capacity.

As equation (2.23) indicates, gear load capacity is determined by thickness, F , and diametral pitch, P_d , which are both limited. The instrument must be encased in a flexible tube, passing through a 10mm port, and hence the net gear thickness is limited by the 9mm annular space. Considering the major diameter of the gear profile to be 7.14mm (corresponding to a 0.25in pitch diameter), the maximum gear pack thickness fitting within the tube is 5.5mm, which is insufficient for the net 7.78mm thickness of G_8 , G_9 , and G_{II} indicated by Table 5.

The net 5.5mm thickness must be distributed such that load capacity is maximized. Prior to optimizing the thickness of the gears, we modify the tooth PA and DP to maximize capacity. A smaller DP implies larger teeth and increased load capacity whereas PA determines the minimum DP a gear of a particular diameter may possess. Standard 20°

and 25° PA prefer at least 18 and 12 teeth, respectively. Our largest feasible tooth profile with 48 DP and 25° PA has a tooth capacity of 28.9 (N/mm thickness) as compared to 21.7 (N/mm thickness) for a smaller 64 DP 25° PA tooth, as seen from Eq.(2.23). The former profile is used to strengthen the top two layers of DALSA, which is where the largest forces occur. The later is used in the bottom layer, which supports less load, to provide a smaller 12-tooth gear on the tip link (Figure 6, labeled F) to decrease tip length and force magnification.

Based on the above profiles, we distribute the 5.5mm thickness of material amongst the three gear layers optimally using standard gradient based techniques (Arora 1989). Given $\theta = -\pi/2$, the gear life parameters previously stated, and the linkage configuration as described, our optimization problem is to:

Find $\{t_1 \quad t_2 \quad t_3\}$ that maximizes $\{F_{TIP}\}$ subject to,

$$\begin{aligned} \frac{\sigma_1 - \sigma_{\max}}{\sigma_{\max}} &\leq 0 & \text{where } \sigma_1 &= 1486 \frac{r_{TIP} F_{tip}}{D t_1} = 2340 \frac{F_{TIP}}{t_1} \\ \frac{\sigma_2 - \sigma_{\max}}{\sigma_{\max}} &\leq 0 & \text{where } \sigma_2 &= 835 \left(L_B + r_B + L + \frac{7}{8} D + \frac{4}{3} r_{TIP} \right) \frac{F_{tip}}{D t_2} = 5012 \frac{F_{TIP}}{t_2} \\ \frac{\sigma_3 - \sigma_{\max}}{\sigma_{\max}} &\leq 0 & \text{where } \sigma_3 &= 1672 \left(L_B + r_B + L + \frac{11}{8} D \right) = 7350 \frac{F_{TIP}}{t_3} \\ t_1 + t_2 + t_3 &\leq 5.5 \end{aligned}$$

where $\sigma_{\max} = 69000$, and t_1 , t_2 , and t_3 are the bottom through top gear pack thicknesses.

Matlab results of the optimization are shown in Table 6. Using the optimal values, we are assured that in the worst case scenario the maximum stresses occur simultaneously in all three layers. In this case, the maximum infinite-life load supported by the tip of a 1cm

Table 6. Optimum gear thicknesses.

| Variable | Items Effected (Figure 6) | Optimum Value |
|----------|------------------------------|------------------|
| t_1 | F,G,H,I,J | 0.88 mm |
| t_2 | C, E | 1.88 mm |
| t_3 | D, K, L | 2.75 mm |

suture needle is evaluated to be 4.54 N. If an infinite life is not required, the instrument can support intermittent loads approaching 8.7N.

We must ensure that the bevel gears are also capable of supporting the loads in the worse case. From Eq.(2.8) , the tangential load, B_T , transmitted by the bevel gears is 23N for a 4.5N needle load and 44N for the intermittent 8.7N needle load. Based on bevel gear strength formulae found in the Machinery's Handbook (Oberg and Jones 1973), the maximum tangential tooth load, W_t , in pounds is,

$$W_t = \frac{\sigma_{all} FJ}{K_M P^{0.75}} \quad (2.24)$$

where $\sigma_{all} = 69ksi$ is the maximum allowable bending stress, $F=0.037in$ is the tooth width, $J= 0.15$ is the geometry factor, $K_M=1.0$ is the mounting factor, and $P=64$ is the DP. W_t is computed to be approximately 17 pounds ($\cong 75N$), which is sufficient to provide a safety factor of 1.7 even for the 8.7N needle load.

2.5 Manufacturing, Performance, and Practical Considerations

DALSA is made of hardened stainless steels that possess high strength and corrosion resistance, but that are difficult and expensive to machine. To achieve high precision in gear profiles, a gear is typically hobbled, heat treated, and ground. This eliminates residual heat treatment deformation and assures a precise tooth profile. Due to the small size of the gears and unusual geared links, precision grinding is quite difficult. This

leaves the machinist with the alternatives of shaping hardened materials or using methods such as wire EDM and lapping.

Stainless steel gears of like materials and equal hardness also present difficulties during operation. Specifically, micro-welding occurs at the pitch line when the gears mate under high pressure. During micro-welding, small amounts of material are typically removed, resulting in pitting. Pitting decreases smoothness of operation and induces premature tooth failure. To eliminate these problems, our design alternates material types (UNS S42000 and UNS S44003) and/or hardness between mating gears and pins.

Due to the number of meshing gears in DALSA, great care is paid to backlash minimization. If backlash is poor, accuracy and repeatability of instrument tip placement will suffer. Backlash is reduced by precise control of manufacturing tolerances, which increase costs. Towards this end, clearance providing a slip fit between the gears, links, and pins is allowed to vary between 0.0001" and 0.0007". Gear shapes are controlled to AGMA 12 standards with class E backlash allowance. As such, the backlash per mating gear is intended to be less than 0.0005" at the pitch diameter. Considering these allowances, we anticipate backlash of the articulation DOF at the tip to be 0.017" (0.4mm). Allowing 0.001" backlash in the bevel gears and considering backlash in the gear train, the backlash at the needle tip due to rotation is 0.028" (0.7mm). The composite backlash for articulation and rotation at the needle tip is 0.036" (0.9mm). Needless to state, backlash will be further diminished by friction between mating components and compliance of the flexible tube covering the mechanism.

2.6 Other Considerations

A key to advancing and improving the application of robotics is the design of mechanisms that provide sufficient dexterity, workspace, and load capacity in lieu of constraints on space and operability. This has been addressed via the design of a robotic arm for enhanced dexterity in minimally invasive surgery. It was found that innovative kinematics structures can assist in providing workspace, but engineering optimization is required to achieve the configuration that provides satisfactory performance. Additional DOF were also required to achieve necessary dexterity in placing the end-effector. In this case, dexterity was accomplished by augmenting the articulation structure with an additional gear arrangement. It was also found that this augmented structure required further optimization to achieve necessary load capacity. The augmented structure also resulted in coupled degrees of freedom where articulation also results in tip rotation, unless compensated. Compensation is not a problem since the kinematic structure is well known and proper control can counteract coupled DOF. The resulting instrument, DALSA, can thus be integrated as part of a surgical robotics system or to form a manual instrument. In summary, while innovative kinematics are extremely beneficial for achieving dexterity in lieu of constraints, engineering practice is mandatory to assure that proper load capacity, dexterity, workspace, and durability can be achieved. In the next chapter, mobility is also considered.

3. Design and Implementation of a Miniature Climbing Robot

3.1 Motivation

In this chapter we address the problem of designing an autonomous climbing robot that is a fraction of the size of any existing climbing robot in the literature. The robot must be sufficiently small to travel through confined spaces, such as ventilation ducts, and to minimize detection while traveling along the outside of a building. These environments require that the robot travel on surfaces with varying inclinations, such as floors, walls, and ceilings, and be able to traverse between such surfaces. Thus, the robot must be capable of adapting and reconfiguring for various environments and modes of operation, be self-contained, and be capable of carrying wireless sensors, such as a camera or microphone and their transmitters. The purpose of deploying such a robot would be for inspection, isolating the source of a biological hazard, or for gathering information about a hostile situation within a building (Tummala, Mukherjee, et al. 1999).

All of the above requirements pose a challenging problem in robot design. The system is substantially constrained by available space, weight, and power, and yet the robot must provide sufficient mobility to climb and traverse between a variety of surfaces. This problem is similar to the surgical mechanism of the previous chapter in that space constraints are crucial; both devices must pass through and operate in confined environments. The climbing robot, however, encounters weight and power limitations not considered during the design of the surgical instrument. Consequently, a conservative approach must be used for minimizing weight and maximizing mobility,

which is just the opposite of the surgical instrument where increased weight usually implies greater strength and load capacity.

3.2 Basic Structure

In response to aforementioned requirements, a biped Reconfigurable Adaptable Miniature Robot (RAMR1) has been designed, constructed, and evaluated [Dulimarta, 2000 #33; Minor, 2000 #30. During this first stage of the development process, the design focus has been on selection, development, and testing of a kinematics structure. RAMR1, shown in Figure 7, uses a biped format with four joints and five links. A revolute hip joint supports two legs and articulated ankles at the ends of the legs. A Smart Robotic Foot (SRF) (Dangi, Stam, et al. 2000) at the ends of the ankles provides the robot with the capability to grip climbing surfaces. Steering is provided by one of these ankles. An under actuated structure allows three motors to drive the robot and permits weight reduction, space savings, and power conservation. To expedite the prototype process,

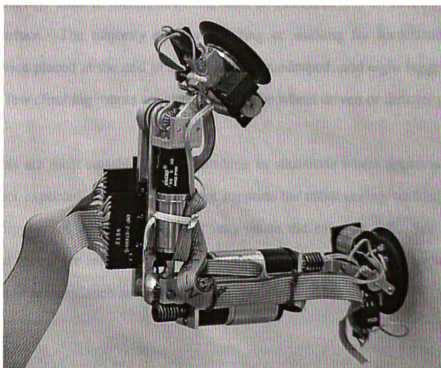


Figure 7. The Biped Climbing Adaptable Robot (RAMR1) scaling a vertical surface.

RAMR1 has been built twice as large as its desired size. The prototype, shown in Figure 7, measures approximately 45mm x 45mm x 248mm in its longest configuration, weighs 335grams, operates under tethered control, and provides video surveillance. The larger prototype has emphasized scale-related issues of the kinematics that result in increased actuator loads and power consumption. During the next stage, power consumption will be much less due to smaller size, but packaging of custom on-board electronics and actuators will provide greater challenges.

3.3 Existing Wall Climbing Robots

Numerous efforts have been undertaken to design mobile robots for climbing inclined surfaces such as walls or ceilings. Common motivations are inspection or maintenance of tall buildings, ship hulls, nuclear facilities, or pipelines where the presence of human life would be a risk, infeasible, or simply cost prohibitive. Due to the intended functionality of these robots, they are typically much larger than RAMR1, as we shall point out in the following survey. Like RAMR1, however, most of them also rely on suction to climb the inclined surface. The majority employ crawling or walking for locomotion, with the suction device placed at the end of a leg. Biped, quadruped, and eight legged robots are typical. A few climbing robots are also known to be wheel driven or thruster propelled.

Biped robots are most suitable to wall climbing in situations where appreciable external loads are not expected. Since a single foot supports the robot during walking, safety is a concern: slippage of the supporting foot may cause the robot to fall. For this reason, many biped robots are intended for inspection purposes only, where the payload consists of lightweight sensors, such as cameras.

Aircraft inspection is the intended application of the biped ROSTAM IV (Bahr, Li, et al. 1996). ROSTAM IV has ankle joints similar to RAMR1, allowing articulation at one ankle and both steering and articulation at the other ankle. The middle joint of ROSTAM IV is prismatic, which limits the robot to traversing between inclined surfaces with acute angles, such as the internal corner of a room. To its benefit, ROSTAM IV's center-of-gravity remains close to the climbing surface during walking. This reduces the bending moment applied to the feet and consequently increases the robot's load capacity and safety.

The biped robot ROBIN (Pack, Christopher, et al. 1997) features similar ankle joints to ROSTAM IV, but its middle joint is revolute rather than prismatic, which is actually stereotypical of biped robots. ROBIN uses opposing pneumatic actuators to control its link angles, but the current design is only capable of traversing surfaces with an inclination up to 60° from horizontal. The structure of the biped created by Nishi (Nishi 1992) for building inspection is very similar to ROBIN, but it features steering capability at both ankles and its joints are actuated by electric motors. Nishi's robot is capable of climbing vertical surfaces and traversing between planes with different inclination.

The joint structures of ROBIN and Nishi's robot are most similar to RAMR1, which uses revolute hip and ankle joints and a differential in one ankle to permit steering. RAMR1 is capable of climbing surfaces with any inclination and traversing between inclined planes. Steering capability permits RAMR1 to move to any point on a surface and also follow a prescribed path. Currently, RAMR1 operates in a tethered fashion, but future revisions will provide tether-less autonomous operation. The greatest difference between RAMR1 and the aforementioned robots is its size and weight. In its longest configuration, when the links are parallel, RAMR1 occupies an envelope 0.25m long by 0.05m wide by 0.05m

high with a mass of 335gr. The next version of RAMR1 will be less than half the current size.

A third style of biped developed by Yano (Yano, Suwa, et al. 1997) uses a central body and feet supported by two DOF ankles. One DOF is rotation of the foot about an axis orthogonal to the climbing surface and the other DOF is prismatic such that the foot raises and lowers. To walk, this robot swings its body about one foot and then the other. Yano's robot is not capable of traversing between surfaces of different inclination. It is the closest in size to RAMR1 since it measures 0.38m x 0.25m x 0.17m, but its 8kg mass is much greater. ROSTAM IV is the closest in mass, at 4kg.

Quadruped and higher legged robots are used more frequently when greater load capacity and stability are required. ROSTAM (Bahr, Li, et al. 1996), NINJA-1 (Hirose, Nagakubo, et al. 1991), and ROBUG II (Luk, Collie, et al. 1991) are all quadruped robots featuring multi-DOF legs protruding from a central body and supporting feet with suction pads. ROBUG III (Luk, Collie, et al. 1996) and MSIV (Ikeda, Nozaki, et al. 1992) are eight legged robots. While these greater numbers of legs provide greater safety and load capacity, they use more complicated mechanisms, which are more difficult to miniaturize and control.

A number of robots have been designed to crawl on walls. These robots usually possess bodies with several movable segment and suction cups on each segment. Like a caterpillar, these robots create locomotion by moving these segments relative to each other and applying suction to the corresponding segments, as in the robot by Gradetsky (Wilson 1990). Similar strategies have been used for underwater welding robots (Bach, Haferkamp, et al. 1996), inspecting hazardous ducts (White, Hewer, et al. 1998), and inspection in nuclear power plants (Briones, Bustamante, et al. 1994). The robot used in

the inspection of nuclear plants, known as ROBICEN, features an articulated segment for traversing between horizontal and inclined planes.

Another class of wall climbing robots, or more appropriately wall driving robots, features drive wheels for propulsion and a method of keeping the vehicle in contact with the inclined surface. Robots by Nishi (Nishi 1996) use a single large sucker, like an inverse hovercraft, or a series of thrusters to maintain contact with the wall. The robot Disk Rover (Hirose and Tsutsumitake 1992) uses magnetic disks for wheels to hold the robot on ferro-magnetic surfaces and provide propulsion.

3.4 Design Constraints

Factors governing the design of RAMR1 are determined by its intended application, namely, untethered gathering of sensory data in an environment where space will be limited and detection undesirable. As mentioned earlier, the robot may be sent through the ventilation ducts of a building, into the rooms of the building, or along the outside of a building or structure. In all of these environments, the robot will need to send wireless sensory data about that environment to a remote location and follow navigational instructions. To accomplish this goal, the robot will need to operate for extended periods with limited power supply. For these reasons, initial design efforts have focused on miniaturization and limiting weight to minimize power usage. In order to validate design concepts more efficiently, space constraints have been relaxed slightly to permit the use of standard miniature components wherever possible. Design and selection of the robot structure, actuators, and sensors have all been completed after considering all of the above factors. The following design constraints have thus been established:

1. **Mobility.** The robot must be capable of (a) walking and climbing on horizontal and vertical surfaces, (b) traversing between surfaces with varying inclinations, and (c) navigating between specified locations.

2. **Size.** In its largest configuration, the robot should occupy a space less than 20cm x 5cm x 5cm.
3. **Space Requirements.** The space required above the surface to maneuver the robot should be minimized to improve performance in confined locations.
4. **Weight.** The holding capacity of the suction feet, termed the Smart Robotic Foot (SRF), governs the maximum weight of the robot. Therefore weight minimization is critical for safe operation.
5. **Sensors.** Due to space requirements, sensors critical for operation are to be used. These include wireless video for reconnaissance, pressure sensors for sensing secure foot placement, and binary joint position sensors for calibrating motor encoders.
6. **Control.** Backlash in the joints and minimal sensing for foot placement require a controller capable of providing adaptability to a broad range of environmental conditions.

3.5 Robot Kinematics

3.5.1 General Form

Several candidate designs were considered prior to constructing RAMR1. As mentioned previously, the objective was small size, extended operation, and adaptability. Several variations of biped, quadruped, and wall driving robots were considered. While the quadrupeds, and higher legged robots, possess safety advantages and increased load capacity, they also require more actuators and increasingly complicated mechanisms. This translates to increased weight, power usage, and control complexity, which are not desirable. Thus, given limited package space and power supply, more complicated designs were considered to be infeasible and design efforts focused on simpler structural formats, such as the biped.

A biped robot can use a structure with fewer components and actuators. Thus, power usage is decreased, weight is reduced, and the design can be miniaturized more easily.

Reliability is also increased since there are fewer parts that can fail. Variations on the biped robot were primarily considered for these reasons. These include structures with a simple central body supporting two feet (the simple biped) and structures consisting of two legs joined by various types of hips (the revolute, prismatic, and hybrid-hip bipeds). Suction cup feet are used to support all of these formats.

3.5.2 Performance Criteria

To compare each of these configurations objectively, they are each evaluated based on their ability to provide mobility and operate in confined environments. Mobility is determined by the capability of the robot format to move between planes with relative inclination of -135° , -90° , -45° , 45° , 90° , and 135° . For each angle of inclination that the robot can cross, one point is awarded. These points are then summed together to

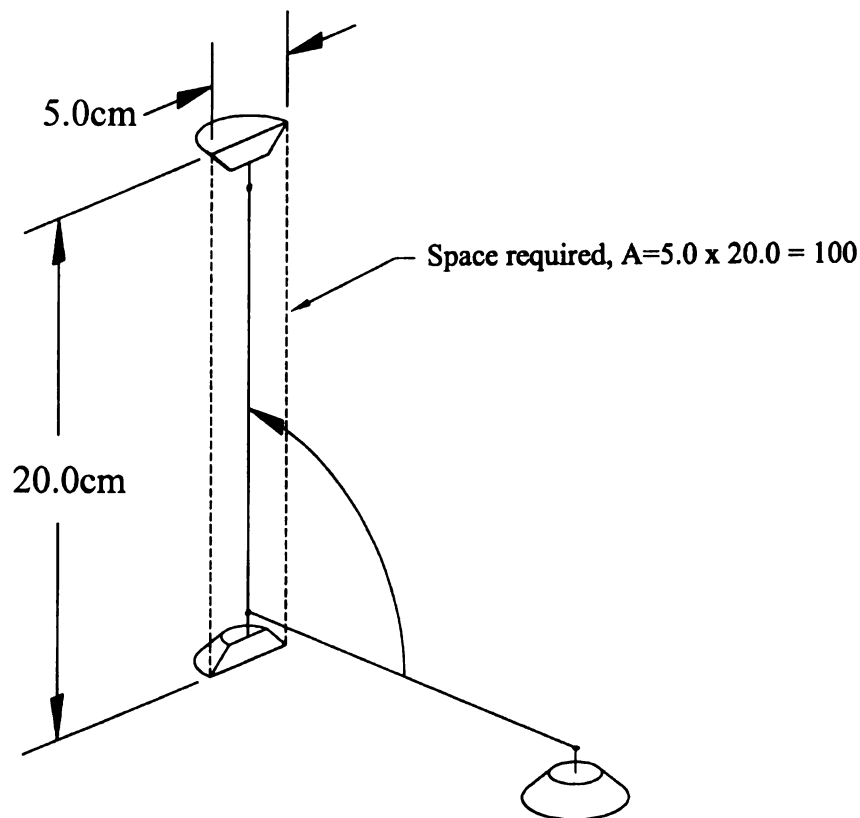


Figure 8. Space requirement typified by cross sectional area required for walking.

establish the mobility rating, M , for the particular kinematics structure. A larger mobility rating, M , indicates that a structure can traverse a broader range of obstacles.

Operability of a robot structure in confined environments is determined by the space that the robot requires for walking. This can be typified by considering cross sectional area that the robot passes through while completing a step, as indicated in Figure 8. Strides characterizing minimum and maximum space requirements for each format are evaluated to determine which strides are suited to a particular environment. Less required space indicates better operability in confined spaces.

3.5.3 Joint Structure: The Simple Biped

The simple biped structure is shown in Figure 9. The robot has a rigid central body with ankle joints at each end of the body that support suction cup feet. In order to traverse between inclined planes, as shown in Figure 9, it is necessary that each ankle provide articulation to the feet. Steering must be also be provided to at least one of the feet to permit the robot to move between arbitrary points on a plane and also to change its angle of approach to an inclined surface. Steering at both feet would simplify these matters, but would significantly increase weight. Thus, weight savings are balanced by increased motion planning.

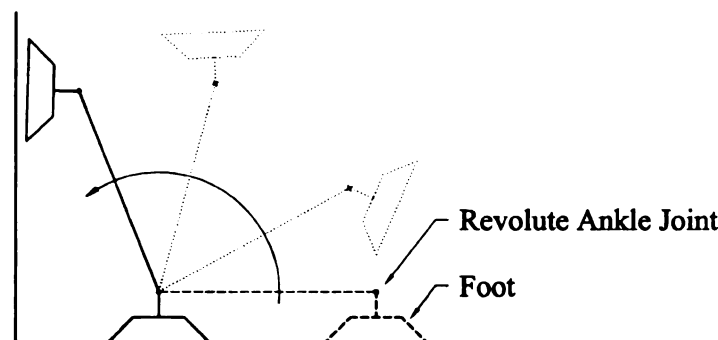


Figure 9. The Simple Biped robot.

The mobility evaluation of the simple biped is shown in Figure 10. As the figure indicates, it is unlikely that the simple biped would be capable of crossing between planes with relative inclinations of -135° , -90° , or -45° . This limitation is attributed to the rigid central body that prevents the structure from placing its foot around corners. Thus, the structure possesses limited dexterity. In situations where dexterity is less important, such as while crossing between planes with inclinations of 45° , 90° , and 135° , the robot performs satisfactorily. Thus the net mobility of the simple biped is $M = 3$.

The space requirement of the simple biped during flipping and crawling strides is illustrated in Figure 11. As the robot flips its entire body end-over end about one foot, as indicated, the flipping stride is achieved. For uniformity, it is assumed that the net length of the robot is the maximum 20cm and that its width is also the maximum 5cm. Thus during the flipping stride, the robot requires a space of 100cm^2 for locomotion. A crawling stride is also shown in Figure 11. In this stride, the robot lifts one foot slightly off the ground and spins its body about the other foot. Here it is also assumed that the robot occupies the maximum 5cm height, but since the foot is elevated slightly, it is







| Relative Inclination of Surfaces | | | | | |
|---|---|---|---|---|---|
| -135° | -90° | -45° | 45° | 90° | 135° |
| Fail | Fail | Fail | Pass | Pass | Pass |
|  |  |  |  |  |  |

Figure 10. Mobility of evaluation of the simple biped structure.

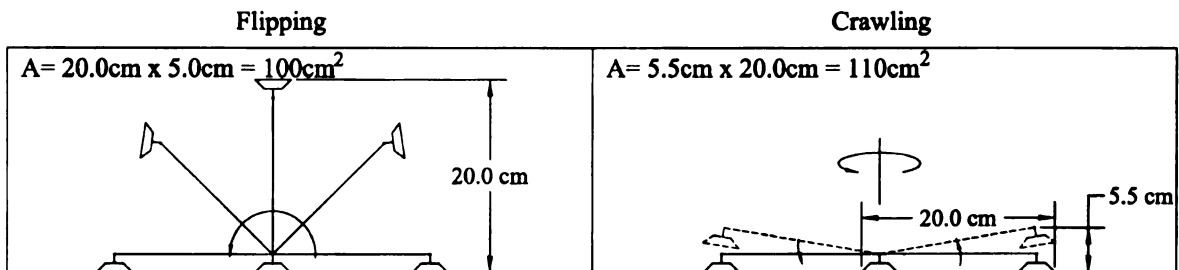


Figure 11. Space requirements of the simple biped structure during flipping and crawling strides.

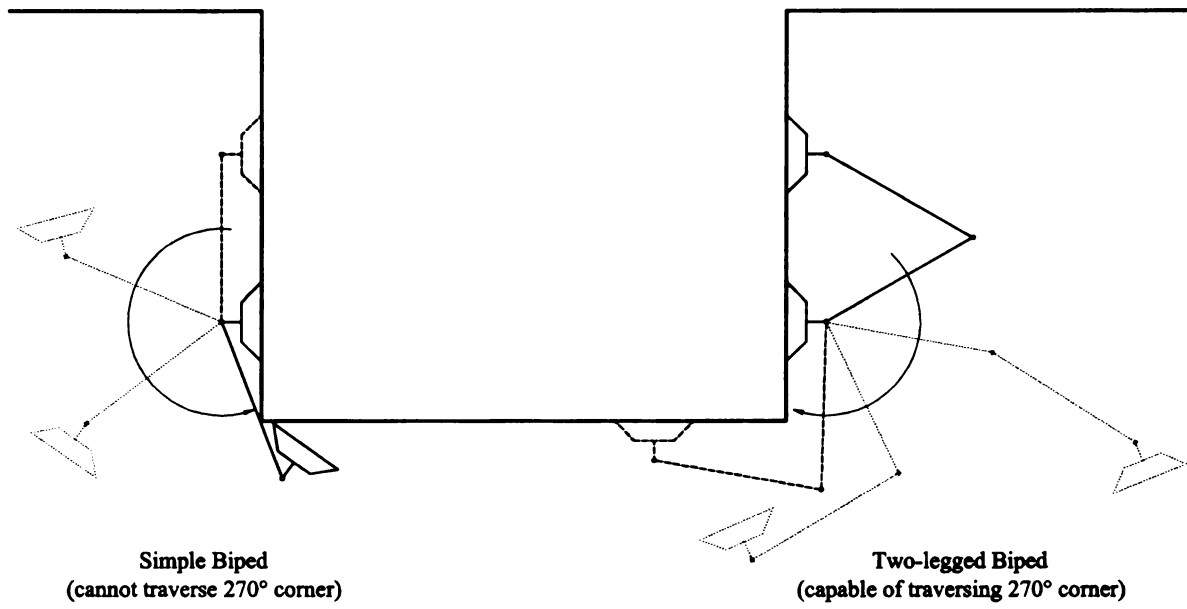


Figure 12. Simple biped and two-legged biped attempting to traverse a 270° corner.

assumed that a 5.5cm height is required. Thus, the net space required during the crawling stride is 110cm^2 .

3.5.4 Joint Structure: The Two-Legged Biped (revolute hip joint)

The two legged biped with revolute hip joint is shown in Figure 12 adjacent to the simple biped. Similar to the simple biped, this two-legged robot requires articulation at both ankles to cross between inclined surfaces and a minimum of steering at one ankle to move between specified locations. Thus, the balance of weight reduction and motion planning complexity can be argued here as well. Enhanced dexterity is the dominant feature provided by the revolute hip joint. This permits the robot to reach around obstacles and place its foot.

The enhanced dexterity of the revolute hip format is evident when we examine its mobility, as illustrated in Figure 13. Unlike the simple biped, the revolute hip biped is capable of ascending all six of the inclined surfaces. Thus, the mobility of the revolute hip two legged biped is $M = 6$.

Depending on stride, the revolute hip also effects space requirements during walking. If we again consider a robot that requires the maximum cross sectional area, Figure 14 indicates that the space required by the flipping locomotion of the revolute hip robot is identical to the simple biped, which is 100cm^2 . During crawling, however, the revolute hip robot is able to substantially reduce its space requirement to 47.5cm^2 by folding its body in half.

Crawling and Flipping strides each have advantages and disadvantages. The crawling stride, for example, is slower and requires more complex joint movements, which also requires more actuators. However, it requires less space above the robot during locomotion and helps maintain a lower profile. The flipping stride requires twice as much space above the robot during locomotion and creates a greater moment arm when the robot “flips” while moving up a vertically inclined surface. Increased actuator loads and foot holding requirements are a direct result. Crawling, on the other hand, maintains a lower profile to the surface, which helps balances the weight added by increased

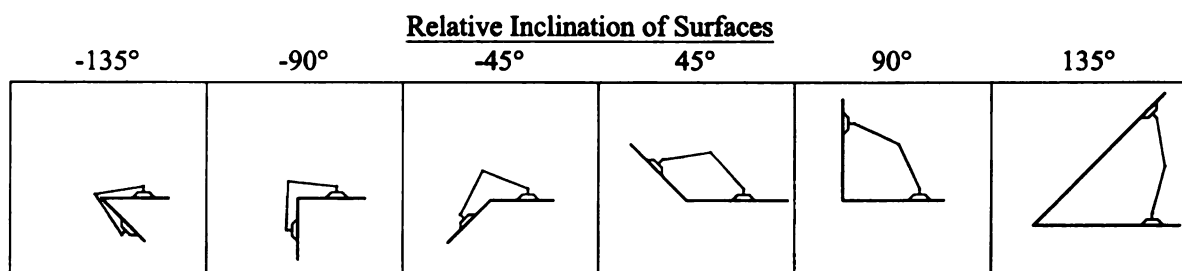


Figure 13. Mobility evaluation of the revolute hip two legged biped.

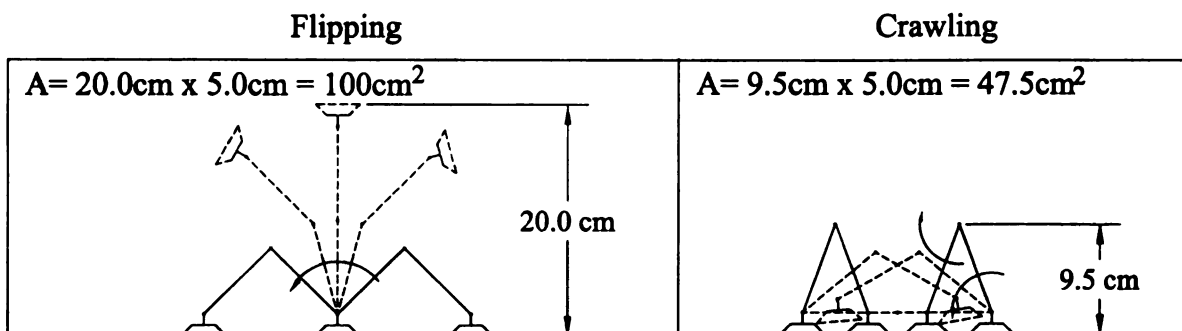


Figure 14. Space requirements of the revolute hip two-legged biped during flipping and crawling strides.

numbers of actuators. Hence, the crawling locomotion has a marginally detrimental effect on stability on an inclined surface and permits the robot to travel through confined spaces.

3.5.5 Joint Structure: The Two-Legged Biped (prismatic hip joint)

The two-legged biped robot with the prismatic hip joint is shown in Figure 15. As indicated, collinear portions of the body sliding relative to each other form the two legs of the robot. At the end of each leg are suction cup feet supported by articulated ankles. They permit the robot to walk between planes with varying inclinations. Steering is provided by at least one of these ankles to allow the robot to walk between arbitrary locations.

The prismatic hip impacts mobility while walking between inclined surfaces. Unfortunately, the prismatic hip joint possesses many of the same limitations as the simple biped since the robot cannot reach around obstructions, as indicated in Figure 16. Thus the robot is likely to not be useful on inclinations of -135° , -90° , or -45° . Using the mobility rating outlined earlier, the net mobility of the prismatic hip biped is then $M = 3$.

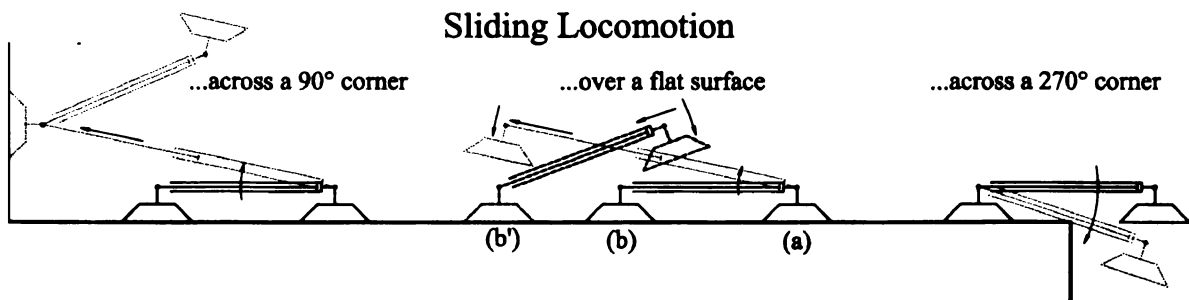


Figure 15. Locomotion of a Two-Legged Biped robot using a prismatic hip joint.

The benefits of the prismatic hip are evident when we examine the space requirements for walking, shown in Figure 17. Assuming that the robot can decrease its length from 20cm to 13.5cm, which is somewhat arbitrary, the flipping stride only requires 67.5cm^2 . While walking in a crawling stride, the space requirement is decreased substantially to 27.5cm^2 . Thus, it is apparent that the prismatic hip joint is well adapted to operation in confined spaces, but at the cost of decreased mobility.

3.5.6 Joint Structure: the Two-Legged Biped (hybrid hip joint)

A re-configurable middle joint that is a hybrid between the prismatic and revolute joints should provide the robot with superior mobility. Such a joint would permit the robot to reconfigure itself such that it could behave as a revolute or prismatic joint as required by the environment and terrain. As indicated earlier, the revolute hip is best for dexterous foot placement whereas the prismatic joint is ideal for confined locations. Thus, if the hybrid joint can behave as both a revolute and prismatic joint, mobility and space requirements will improve. Discrete regimes of revolute or prismatic behavior would

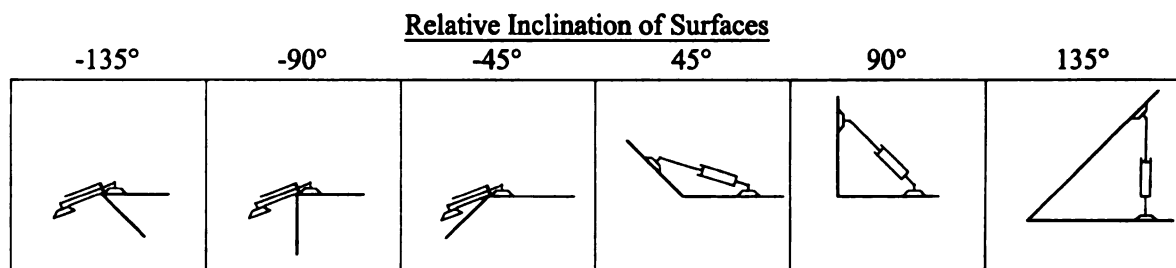


Figure 16. Mobility evaluation of the prismatic hip two-legged biped robot.

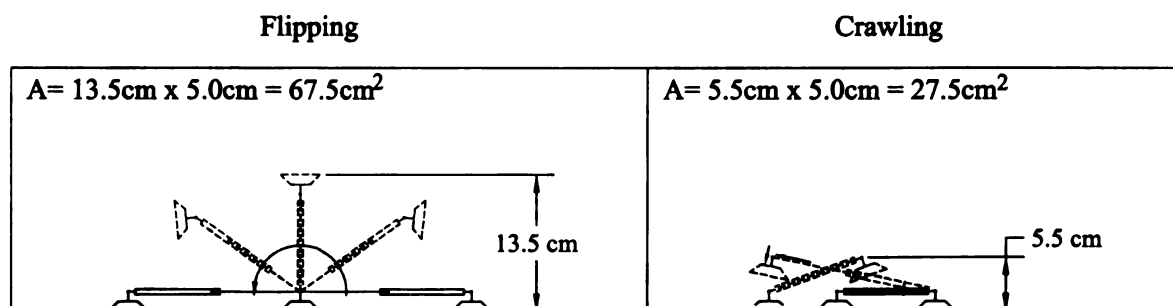


Figure 17. Space requirements of the prismatic hip two-legged biped during flipping and crawling strides.

also make control of the joint easier and permit it to be driven by a single actuator for space and weight savings.

Numerous versions of a hybrid prismatic-revolute joint can be conceived. One realization is shown in Figure 18. The hybrid mechanism consists of a movable link that uses pins to guide its motion via slotted guide links. These pins, Guide Pins 2 & 3 in Figure 18, travel in Guide Slots 2 & 1 on the Guide Links, respectively. The Moving Link is driven via the Thrust Link, which travels in Guide Slots 1 & 2 via Guide Pins 1 & 2, respectively. The motion of the Thrust Link, and hence the Moving Link, is driven via the Drive Block and Drive Rod, which are essentially a lead screw and mating tackle.

Notice that Guide Slot 2 possesses a straight segment that allows the mechanism to act as a prismatic joint and a curved portion that permits the mechanism to function as a

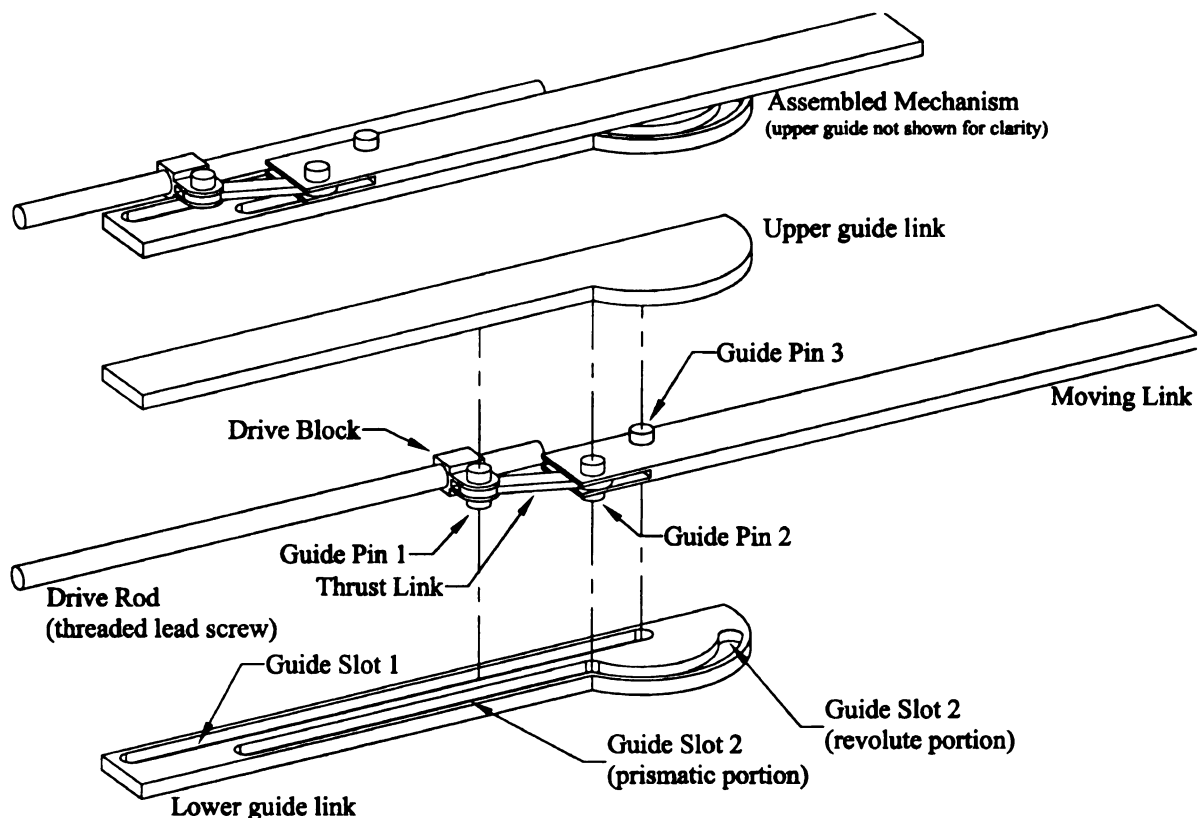


Figure 18. A hybrid revolute and prismatic joint shown assembled and in exploded view.

revolute joint. The transition between prismatic and revolute behavior occurs when Guide Pin 3 reaches the limit of Guide Slot 1, as shown in the exploded view. As the Thrust link continues to drive the Moving link, Guide Pin 2 is forced to travel in the revolute portion of Guide Slot 2. Hence, via a single actuator, such as a coreless DC motor, the hybrid mechanism is capable of behaving as either a prismatic and revolute joint. Examples of these distinct modes of operation are shown in Figure 19.

As Figure 19 indicates, the hybrid mechanism is capable of exhibiting prismatic or revolute behavior. The particular design shown is capable of expanding from a net length of 100mm in the closed position to 150mm in the open position. As the thrust link continues to drive the mechanism, revolute behavior ensues and the link can actuate from the straight configuration, denoted as 0° articulation, to a 120° counter-clockwise articulation. A 30° articulation is shown in Figure 19. Thus, the hybrid joint is fully

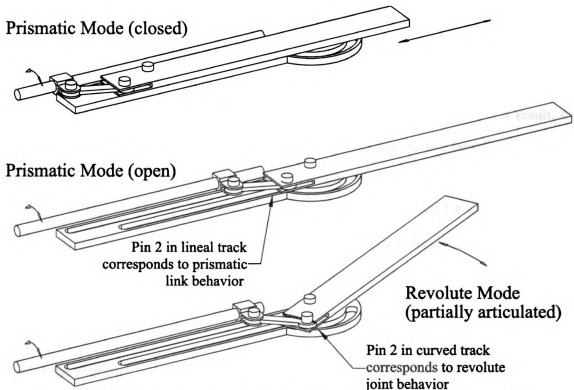


Figure 19. The hybrid revolute and prismatic joint shown in several positions.

capable of behaving as either a prismatic joint, or to a limited degree as a revolute joint.

The limited articulation provided by hybrid joint must be debated since it constrains the motion of the robot. The articulation provided by the joint is certainly sufficient to allow the robot to perform a crawling stride similar to that of the revolute hip joint, shown in Figure 14. The flipping stride, also shown in that figure, is not achievable since that stride requires at least $\pm 90^\circ$ hip articulation, which the hybrid cannot provide in the design presented. However, the design can be modified to provide bi-directional articulation in addition to prismatic motion.

The hybrid is also limited while crossing planes of various inclinations. This is because the robot must first approach the inclined surface in a manner such that its limited articulation can be exploited. If the robot can maneuver into such an orientation, it is then limited in its capability to cross between the surfaces since it is forced to use the crawling stride. This stride predisposes the robot to place its trailing foot behind the leading foot, and thus the ability of the robot to cross between planes of -135° , -90° , or -45° is entirely dependent upon the leading foot being placed sufficiently far onto the inclined surface such that there is room for the trailing foot behind it. As a result, the limited articulation of the hybrid joint does not entirely realize the benefits of revolute hip. Whereas the revolute hip received a mobility score of 6, the hybrid joint only receives a rating of $M = 3 + 3(0.5) = 4.5$. Full marks are awarded for crossing between inclinations of 45° , 90° , and 135° where the hybrid can behave as a prismatic joint. Half points are awarded for crossing between planes of -135° , -90° , or -45° due to the limited capability of the robot in these situations.

Despite the mobility limitations of the hybrid joint, it capable of minimizing space usage during locomotion. When the joint is in its prismatic regime, the robot uses the very

minimal 27.5cm² as in the case crawling with the prismatic joint. In the revolute crawling mode, the robot only requires 47.5cm². So despite mobility limitations realized by the current hybrid design, it does capture the best space requirements of both the revolute and prismatic hips.

3.5.7 Selection of Kinematics Structure

The mobility and space requirement data derived in the previous sections is presented in Table 7. The data is indexed and identified by hip joint style and walking stride. For analysis purposes, the data is normalized relative to the average performance of the designs. Normalized mobility is determined by,

$$M_i^N = \frac{M_i - M_{avg}}{M_{avg}} \quad \text{where} \quad M_{avg} = \frac{1}{n} \sum_{i=1}^n M_i .$$

and the normalized space requirements are calculated by,

$$A_i^N = \frac{A_i - A_{avg}}{A_{avg}} \quad \text{where} \quad A_{avg} = \frac{1}{n} \sum_{i=1}^n A_i .$$

Table 7. Data indicating space requirements and mobility of various robot joint structures and strides.

| Configuration | | | Space Requirement | | Mobility | |
|---------------|---------------|-----------------|-------------------|---------|-----------|---------|
| index, i | HIP Structure | Walking Stride | A_i | A_i^N | M_i | M_i^N |
| 1 | Simple | Flip | 100 | 0.52 | 3 | -0.27 |
| 2 | Simple | Crawl | 110 | 0.67 | 3 | -0.27 |
| 3 | Revolute | Flip | 100 | 0.52 | 6 | 0.45 |
| 4 | Revolute | Crawl | 47.5 | -0.28 | 6 | 0.45 |
| 5 | Prismatic | Flip | 67.5 | -0.02 | 3 | -0.27 |
| 6 | Prismatic | Crawl | 27.5 | -0.58 | 3 | -0.27 |
| 7 | Hybrid | Revolute crawl | 47.5 | -0.28 | 4.5 | 0.09 |
| 8 | Hybrid | Prismatic crawl | 27.5 | -0.58 | 4.5 | 0.09 |
| | | | Avg: 68.4 | | Avg: 4.13 | |

These normalized expressions are designed such that positive values indicate better than average performance and negative values indicate lower than average performance. The prismatic ($i = 6$) and hybrid ($i = 8$) hips possess the best normalized space requirement rating of 0.58. The revolute hip formats ($i = 3, 4$) have the best mobility rating of 0.45.

To evaluate each joint structure and walking stride in different environments, a weighted sum of the normalized mobility and space requirement data is formed. The weighted value of a configuration is thus calculated from,

$$\sigma_i = -A_i^N w_A + M_i^N w_M$$

where three sets of weightings were selected to emphasize operation in unconfined ($w_A=0.5$, $w_M=1.5$), confined ($w_A=1.5$, $w_M=0.5$), and mixed ($w_A=1.0$, $w_M=1.0$) environments. These weighted calculations are shown in Table 8. The data indicates that operation in an open environment is best achieved by #4, which is the revolute hip with crawling stride, which received the highest rating of 0.59. Operation in a confined environment is best achieved by #8, the hybrid hip with prismatic crawling stride, with a rating of 0.92. This is followed very closely by #6, which received a rating of 0.74. In an environment where equal emphasis is placed on mobility and space requirement, the revolute hip with crawling stride ($i = 4$) performs best with a rating of 0.73. This is

Table 8. Weighted performance evaluations of the robot configurations operating in open, confined, and mixed environments.

| Configuration | | | Environment | | |
|---------------|-----------|-----------|-------------|----------|-------|
| index, i | Structure | Stride | Open | Confined | Mixed |
| 1 | Simple | Flip | -0.53 | -0.91 | -0.79 |
| 2 | Simple | Crawl | -0.61 | -1.14 | -0.94 |
| 3 | Revolute | Flip | 0.20 | -0.55 | -0.06 |
| 4 | Revolute | Crawl | 0.59 | 0.65 | 0.73 |
| 5 | Prismatic | Flip | -0.28 | -0.17 | -0.30 |
| 6 | Prismatic | Crawl | 0.02 | 0.74 | 0.31 |
| 7 | Hybrid | Revolute | 0.23 | 0.46 | 0.37 |
| 8 | Hybrid | Prismatic | 0.38 | 0.92 | 0.67 |

followed distantly by the hybrid hip joint with prismatic stride ($i = 6$) with a rating of 0.67.

The revolute middle joint is selected for several reasons. First, the capability of the hybrid joint is not entirely satisfactory in its current form, and it is believed that improvements can be made to achieve bi-directional articulation. Since this robot is in its first phase of construction, and a prototype must be constructed within the first year, these improvements are left as the subject of later research. Secondly, the revolute joint is a much simpler mechanism, which inevitably will be more reliable since it has fewer parts and mechanisms that could fail. Reliability was deemed paramount since success of this first prototype would be largely responsible for renewed funding, and hence the revolute hip joint was selected based on its superior performance and anticipated reliability. The development of an improved hybrid joint is the subject of the later research. Details of the revolute hip design will now be presented.

3.5.8 Coupled DOF and the Two-Legged Biped

The revolute hip structure is used as a platform for the robot. To reduce the number of actuators, and hence weight, consider the concept of coupling the DOF of the robot. As shown in Figure 20, the Two-Legged Biped, with a revolute middle joint, has four DOF. At one ankle, which consists of Link 1, Joint 1, Link 2, and Joint 2, there is one DOF for steering (Joint 1), described by angle γ , and one DOF for pivoting (Joint 2), described by angle α . At the other ankle, Link 5, there is only a single DOF for articulation (Joint 4), described by angle β . At the hip joint, Joint 3, there is a revolute DOF for controlling the angle between the legs, described by angle λ . Each DOF powered individually would require four actuators. Coupling the motion of two of these DOF would reduce the

number of actuators by 25% and hence decrease the weight of the robot significantly since the actuators are one of largest contributors to the robot's net weight.

Obviously, the steering DOF at Joint 1 must remain uncoupled. However, coupling between Joints 2 and Joint 3 is practical because the hip and ankle joints tend to function in unison. A belt drive coupling the joints, conceptually illustrated in Figure 20, can accomplish this. Assuming symmetric foot and link sizes, as illustrated in the figure, the change in link angles during a flip motion will be $\Delta\lambda = 180^\circ$ and $\Delta\alpha = 90^\circ$. Selecting the pulley diameter at Joint 2 twice as large as the pulley diameter at Joint 3 guarantees that this relationship will be maintained. Hence, by driving the middle joint, Joint 3, the ankle joint, Joint 2, will be driven appropriately.

Coupled DOF also produces side effects that may not be desirable. Once the joints are coupled, they then function as one DOF and capabilities that were based upon their independent actuation no longer exist. For example, the coupling designed above allows the robot to perform the flipping stride, Figure 14, but the crawling stride is no longer possible because the relative rotations of the hip and ankle joints are not the same for both strides. Another complication is encountered when aligning Foot 1 with the surface

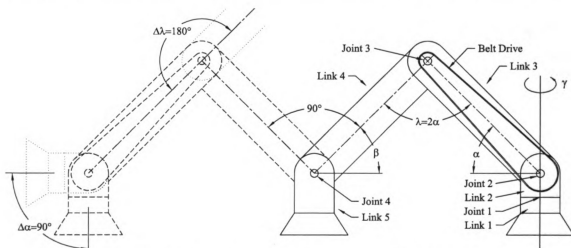


Figure 20. Joint and link structure of the Two-Legged Biped with coupled DOF.

because independent control of Joint 2 is not feasible. Rather, Joints 3, 4, and 5 must all be actuated simultaneously to align the foot with the surface. Hence, slightly increased control complexity and decreased operability are compromises that must be made with coupled DOF. As mentioned earlier, though, if these compromises are acceptable, a few lines of computer code weigh much less than an additional actuator!

3.6 Robot Design

3.6.1 Biped Structure

Figure 21 contains illustrated pictures of the current climbing robot. This figure is a little cluttered by wiring on the robot and an exploded diagram of the robot has been included in Figure 22. Full detail drawings of the components shown in Figure 22 are available in Appendix B. As described in the previous sections, the current format of the biped climbing-robot consists of a two-legged structure using a revolute hip joint to support two legs of equal length. At the end of each of these legs are ankle joints supporting suction cup feet. Ankle #1 consists of Joint 1 and Joint 2 which provide DOF for steering and articulation. Ankle #2 provides only articulation via Joint 4.

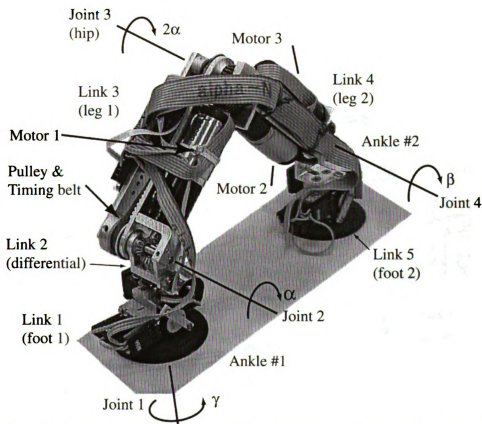


Figure 21. Illustrated pictures of the Biped Climbing robot with a revolute hip joint.

Coupling between the hip, Joint 3, and Joint 2 is accomplished via belt driven pulleys, shown in Figure 22 and Figure 21. This reduces the DOF of the robot and three motors are used to drive the four joints. Motor #2 drives the Hip Joint by a worm gear system and rotation of the Hip Joint is coupled to articulation of Joint #2. Motor #2 is supported by Link #3, Figure 22, and the shaft of the geared motor unit supports the worm. The worm is made of hardened steel and has a Diametral Pitch (DP) of 48, a single 14.5° lead, and a .38" Outside Diameter (OD). As indicated in Figure 22 the worm gear (48 DP, 16 tooth) is pressed into Links #1 and #5 with a filleted raised shoulder to provide stability and improved coupling between the gear and link. The revolute hip joint under consideration is created by Shaft #3, which is firmly retained by the motor bracket integral to Link #4. The shaft provides a bearing surface for the worm gear and thus relative rotation between Link #3 and Link #4 is achieved when the worm rotates.

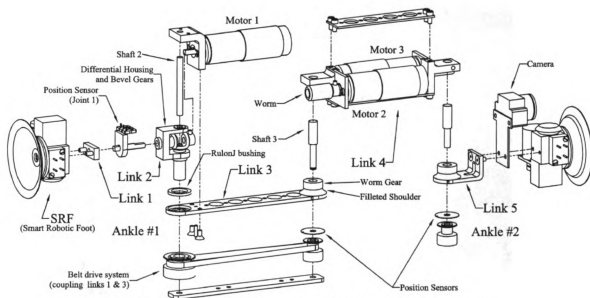


Figure 22. An exploded diagram of the Biped Climbing Robot with Smart Robotic Feet (Dangi, Stam, et al. 2000).

Coupling between articulation of the Hip joint and Ankle #1 is achieved via the belt-pulley system, shown in Figure 22 and Figure 23. A pulley clamped to the end of Shaft 3 drives the coupled DOF and retains Link #3. Rotation of Link #3 causes the relative motion between the fixed pulley and the link, and this drives the belt motion. At Ankle 1, there is a mating pulley clamped to the Differential Housing and the belt motion causes it to rotate. The amount of rotation between the hip joint is half as much as the rotation of the differential joint by design of the 2:1 sizing of the pulleys. Timed belts and pulley were used to guarantee consistent relative position of the joints and a slight preload was used to prevent slipping.

As mentioned before, as the hip joint articulates it simultaneously causes articulation of Joint #2 via the belt drive system, indicated in Figure 23. This motion is also coupled to the rotation of Joint #1 via the bevel gears indicated in Figure 22 and Figure 24. To help understand this phenomenon, assume that Motor #1 is not allowed to rotate and realize that this motor controls the rotation of the bevel gears. Also note that the bottom bevel gear rotation is not coupled to articulation of the differential joint. Hence, the bottom

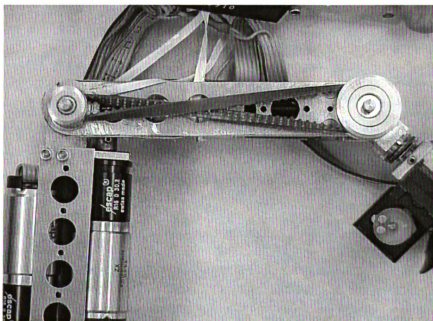


Figure 23. Belt drive system coupling articulation of Ankle #1 and the hip joint.

bevel gear in the differential will not rotate as the differential articulates. However, as the differential articulates it does displace Foot #1, and this displacement causes the foot and its bevel gear to circle travel in a circle about the stationary bevel gears. Because of the mating bevel gears, this motion is necessarily coupled to the rotation of the foot about Shaft 1, and thus the coupled articulation DOF are actually coupled to the steering DOF, too. Motor #1 is responsible for driving the bevel gears of the differential, and hence must compensate for this coupling during actuation of the hip joint.

The differential is supported via a RulonJ bearing in Link #3, indicated in Figure 22, and also by Shaft #2, which is clamped into the bracket supporting Motor #1. RulonJ is a Teflon embedded polymer that provides the lubricant qualities of Teflon without the undesirable malleability of Teflon. Shaft #2 is responsible for supporting the upper portion of the differential housing as well as the bottom bevel gear of the differential. A brass bushing is used in the upper portion of the differential to reduce friction. At assembly, spacers must be placed below the bottom bevel gear to control its mating

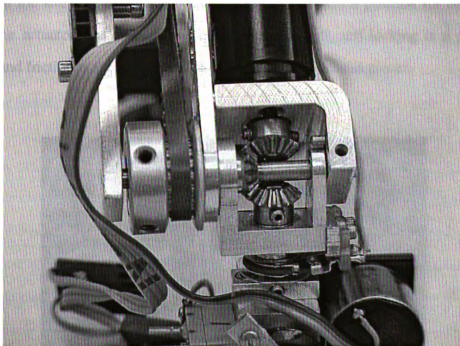


Figure 24. Ankle #1 and the differential.

relationship with the bevel gear driving the foot. The bevel gear is brass, so its friction with the shaft and steel spacers is minimal. Similarly, spacers placed between the motor bracket and Link #3 control the interaction between the lower bevel gear and the bevel gear mounted to Motor #1. A double set of miniature ball bearings support Shaft #1 and the foot. They are pressed and retained in the differential housing. Such a durable and low-friction support for Shaft #1 is especially important since the entire load of the robot is supported as a cantilever by this joint.

Motor #3 drives articulation of Ankle #2 via a worm drive identical to the one used in the hip joint. There are three motivators for selecting a worm drive at these joints. The first is that the worm gear compactly provides additional gear reduction to allow for smaller gear boxes. As important, the worm drive allows the actuator to be mounted transversely to the joint axis and reduced the size of the robot. Hence, the actuators become integral parts of Link #4, as shown in the figures, rather than a large object protruding out the side of the robot. The last motivator is the self-locking characteristic present in most worm drives. In the situation that the robot may have to maintain a position for an extended period, the actuators may sit idle. Unfortunately though, self-locking is a product of friction, and friction is synonymous with inefficiency and wasted power.

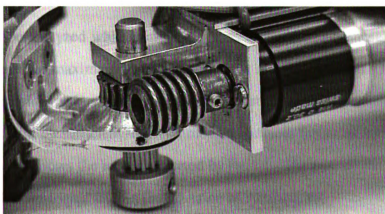


Figure 25. The worm drive at joint 4.

To counteract friction effects, a combined MbS_2 and Graphite coating was applied to the worm, worm gear, and shafts. These components, which all featured polished steel rubbing against brass, typically possess a coefficient of friction of about 0.3. The application of the MbS_2 and Graphite coating reduces the friction to a rated value of about 0.07 (Dow-Corning 1999). The coating is quite durable, with a rated life of 71 hours under 1000lb per the federal pin and vee-block test method 791a-3807, so it provides suitable dry lubrication for the prototype. Liquid lubricants were not used because of the open joint structure and undesirable messiness.

3.6.2 Force Analysis: climbing a vertical surface supported by foot 1

The purpose of performing this force analysis is to determine the feasibility of different actuators for Motor #2. A static force analysis is performed on the robot in the configurations that apply the largest forces on the actuators. This will help determine the ideal actuator among numerous alternatives. All given actuators under consideration are geared DC motor units with position encoders. Each model weighs a different amount, and has its own geometric properties and load capacities. These variations change the load requirements from unit to unit, and thus each unit must thus be considered independently to determine feasibility of its application. Of course, the selection of Motors #1 and #3 both have direct consequence on Motor #2, and vice versa.

The robot will be analyzed while climbing a vertical surface in a straight, cantilevered, orientation where the maximum moments and loads are encountered. Feasibility of an actuator will be confirmed by a safety factor of at least 2.0 at this operating point. Such a safety factor should be sufficient to accommodate dynamic forces as well as unexpected friction. Figure 26 shows the robot supported by Foot 1. The case of the robot supported by Foot 2 will be considered later in the selection of Actuator #3.

The robot supported by Foot #1 is shown assembled and as Free-Body-Diagrams (FBD) in Figure 26. The following notation is used in the figure:

F_B = Belt force acting on the pulley

F_{WT_i} = Tangential worm load

F_{WR_i} = Radial worm load

L_i = Length of the i^{th} link between joints i and $i + 1$

P_{x_i} = Force on the i^{th} joint in the x - direction

P_{y_i} = Force on the i^{th} joint in the y - direction

T_{F_i} = Static friction torque on the i^{th} joint

W_i = Total weight of the i^{th} body

d_i = Distance to the center of mass of the i^{th} body from its support point.

r_g = Pitch radius of worm gear

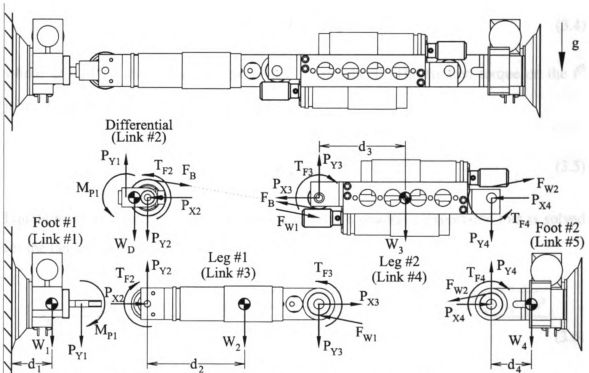


Figure 26. Free body diagrams of the climbing robot supported by Foot #1 on a vertical surface (some forces omitted for clarity).

r_{si} = Radius of shaft supporting the i^{th} joint

α = angle of belt between pulleys

λ = worm lead angle

ψ = worm gear pressure angle

μ = Static coefficient of friction

Using the above notation while examining Foot #2, the tangential worm force, F_{WT2} , and pin forces, P_{X4} and P_{Y4} , are determined to be:

$$F_{WT2} = \frac{1}{r_g} (W_4 d_4 + T_{F4}) \quad (3.1)$$

$$P_{X4} = F_{WT}^2 \quad (3.2)$$

$$P_{Y4} = W_4 + F_{WR2} \quad (3.3)$$

The radial force on the worm drive, F_{WRi} , is generically determined by (Meritt 1971),

$$F_{WRi} = F_{WTi} \tan \psi \quad (3.4)$$

where $\psi = 14^\circ$ is the pressure angle of the worm wheel. The friction torque on the i^{th} joint, T_{Fi} , is then generically determined by,

$$T_{Fi} = r_{si} \mu \sqrt{P_{Xi}^2 + P_{Yi}^2} \quad (3.5)$$

Equations (3.1) through (3.5) are then used to form a quadratic expression that is solved for the tangential worm wheel force, F_{WT2} :

$$F_{WT2} = \frac{-r_G W_4 d_4 - W_4 \tan(\psi) r_s^2 \mu^2 - W_4 \sqrt{2 d_4 r_G \tan(\psi) r_s^2 \mu^2 - r_s^4 \mu^4 + r_s^2 \mu^2 d_4^2 + \tan(\psi)^2 r_s^2 \mu^2 d_4^2 + r_G^2 r_s^2 \mu^2}}{r_s^2 \mu^2 + \tan(\psi)^2 r_s^2 \mu^2 - r_G^2} \quad (3.6)$$

Similarly, the forces supporting Link #3 are F_{WT1} , P_{X3} , and P_{Y3} . They are calculated as follows,

$$F_{WT1} = \frac{1}{r_G} (W_3 d_3 + T_{F3} - T_{F4} + F_P r_{p1} + F_B r_{p1} + (F_{Sy}^4 - F_{WR}^2) L_3) \quad (3.7)$$

$$\begin{aligned} P_{X3} &= F_{WT1} - F_{BX} - P_{X4} + F_{WT2} \\ &= F_{WT1} - F_{BX} \end{aligned} \quad (3.8)$$

$$\begin{aligned} P_{Y3} &= W_3 + P_{Y4} - F_{WR2} + F_{WR1} - F_{BY} \\ &= W_3 + W_4 + F_{WR1} - F_{PY} \end{aligned} \quad (3.9)$$

where

$$F_{BX} = F_B \cos \alpha \quad (3.10)$$

$$F_{BY} = F_B \sin \alpha \quad (3.11)$$

and α is the angle of the belt between the pulleys, determined by,

$$\tan \alpha = \frac{r_{P1} + r_{P2}}{L_2} \quad (3.12)$$

Before an expression for F_{WT1} can be formed, the pulley force F_B must be evaluated via analysis of Link. Keep in mind that the pulley force acts as a torque on the Differential, which then creates relative rotation between Link #2 and the Differential. This torque is essentially the input required to rotate Link #2 and will be determined from this link. The forces supporting Link #2 are determined as,

$$\begin{aligned} P_{X2} &= F_{WT1} - P_{X3} \\ &= F_{BX} \end{aligned} \quad (3.13)$$

$$\begin{aligned} P_{Y2} &= W_2 + P_{Y3} - F_{WR1} \\ &= W_2 + W_3 + W_4 - F_{BY} \end{aligned} \quad (3.14)$$

$$F_B = \frac{1}{r_{P2}} [W_2 d_2 + T_{F2} - T_{F3} + F_{WT1} r_G + (P_{Y3} - F_{WR1}) L_2] \quad (3.15)$$

Equations (3.7) and (3.15) each form non-linear equations in their fully expanded form which must be solved numerically for F_B and thus F_{WT1} . Once these equations have been solved, sufficient information exists for determining the load applied to Actuator #2. Since the force F_{WT1} is created by a worm drive system, we first realize that the force is equivalent to a torque applied to the worm gear, denoted by M_{WG1} :

$$M_{WG1} = F_{WT1} r_G \quad (3.16)$$

and that a worm torque, M_{w1} is required to create the worm gear torque. Considering that torque loss due to friction in worm drives can be substantial, we first consider the efficiency of the worm drive (Meritt 1971):

$$EFF = \frac{\tan \lambda}{\tan(\lambda + \arctan \mu)} = 0.38 \quad (3.17)$$

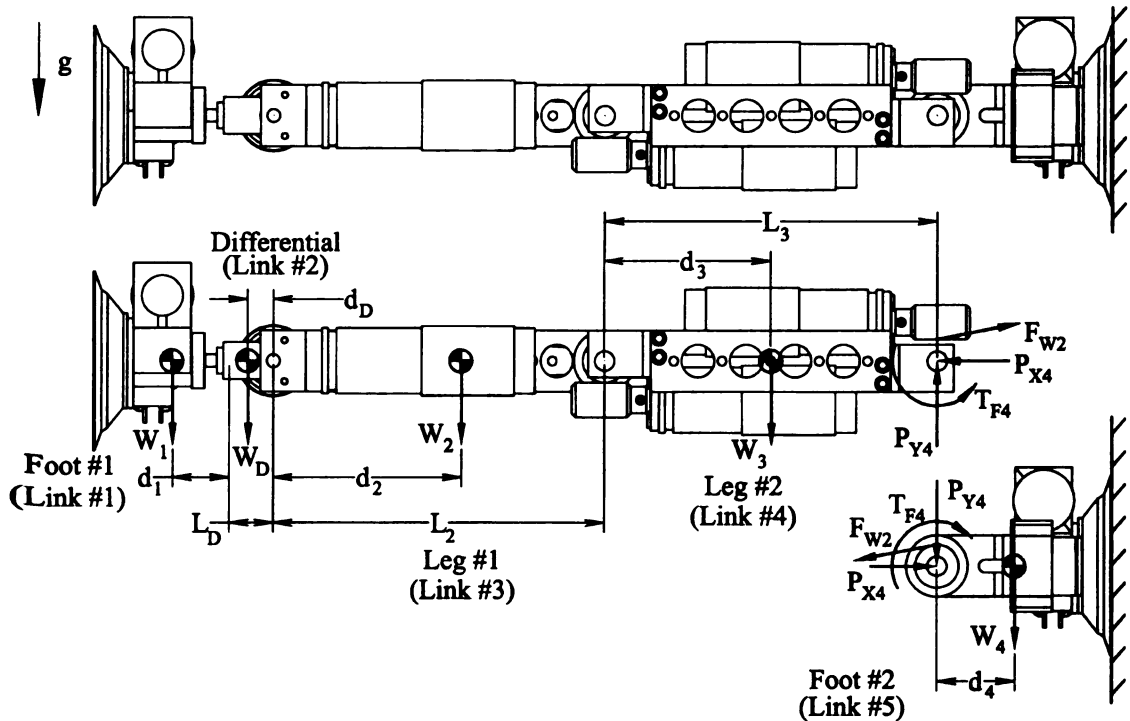


Figure 27. Free body diagrams of the climbing robot supported by Foot #2 on a vertical surface (some forces omitted for clarity).

Given that the reduction ratio of the worm drive is 20:1, the required worm torque is then,

$$M_{w1} = \frac{M_{WG1}}{20EFF} \quad (3.18)$$

Selection of Actuator #1 is made based upon the capability of the actuator to provide this torque while operating near a preferred joint speed. This will be considered further in Section 3.6.6 after the worst-case loads for the other actuators have been determined.

3.6.3 Force Analysis: climbing a vertical surface supported by Foot 2

In this section the robot is again considered while climbing a vertical surface, Figure 27, but now Foot #2 supports it. The robot is again in a straight, cantilevered, configuration where the maximum load on Foot #2 occurs. In this situation, however, the forces due to the other bodies can be considered cumulatively since the coupling created by the belt drive does not affect Actuator #3. Essentially, those forces are internal to the rest of the robot. The forces acting on Foot #2 and affecting the actuator are determined to be,

$$P_{X4} = F_{WT2} \quad (3.19)$$

$$P_{Y4} = W_4 + W_3 + W_2 + W_D + W_1 + F_{WR2} \quad (3.20)$$

$$T_{F4} = r_{s4} \mu \sqrt{P_{X4}^2 + P_{Y4}^2} \quad (3.21)$$

$$F_{WR2} = F_{WT2} \tan \psi \quad (3.22)$$

$$F_{WT2} = \frac{1}{r_G} \left[W_3(L_3 - d_3) + W_2(L_3 + L_2 - d_2) + W_1(L_3 + L_2 + L_D + d_1) + W_D(L_3 + L_2 + d_D) + T_{F4} \right] \quad (3.23)$$

Equations (3.19) thru (2.3) are then used to form a quadratic equation for the driving force F_{WT2} , which is not shown here because of its extreme length. Once F_{WT2} is calculated, then the effective torque on worm gear is determined by,

$$M_{WG2} = F_{WT2} r_G \quad (3.24)$$

The worm torque can then be determined by,

$$M_{w1} = \frac{M_{WG1}}{20EFF} \quad (3.25)$$

where the efficiency, *EFF*, is determined by Equation (2.22). This worm torque will then **be** used in Section 3.6.6 for selecting Actuator #3.

3.6.4 Force Analysis: Steering on a vertical surface while supported by Foot 2

The maximum loads for steering the climbing robot will now be examined. These forces occur when the robot is steering on a vertical surface. If independent articulation of Joints #2 and #3 were possible, this maximum would occur when the hip joint and ankle joint #2 were straight, ankle joint #1 was bent 90°, and the orientation was such that the robot was perpendicular to the gravitational field. Rather, articulation of Ankle #1 is directly coupled to the hip joint, and the aforementioned configuration cannot be achieved. Instead, as the hip joint bends, so does Ankle #1, and the effective moment created by steering the robot changes. The maximum of that moment, denoted by T_1 , occurs when the robot is in the configuration shown in Figure 28, and is calculated as,

$$T_1 = W_2 d_2 \cos 45^\circ + W_3 (L_2 + d_3) \cos 45^\circ + W_4 (d_4 + (L_2 + L_3) \cos 45^\circ) \quad (3.26)$$

This equation will also be used in Section 3.6.6 for actuator selection.

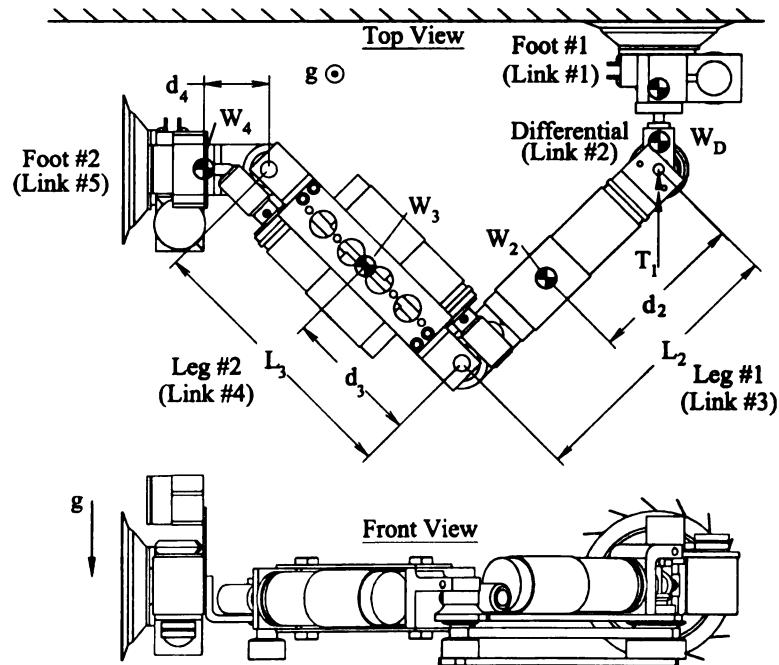


Figure 28. Diagram of the climbing robot steering via Foot #1 on a vertical surface.

3.6.5 Actuator Selection Criteria

We now consider the force analysis conducted in the previous sections to determine the **viability** of various actuators applied to the climbing robot. There are a number of **criteria** that the optimal actuator must satisfy. They are summarized in the order that they **were** examined during the design process:

1. Torque Safety Factor (TSF). The actuators must be able to provide a safety factor of at least 2.5 to compensate for unanticipated friction affects and for dynamic forces, which are anticipated to be quite small due to small joint velocities. The TSF is calculated based on the worst-case joint torques, described in the previous sections, and the maximum continuous torque that the motor unit can supply to the joint. A generic expression for TSF is,

$$TSF_i = \frac{T_i}{n_i T_{cont,i} / \epsilon_{net}} = \frac{T_i \epsilon_{net}}{n_i T_{cont,i}} \quad (3.27)$$

where T_i is the worst case joint torque, n_i is the gear reduction, ϵ_{net} is the net efficiency of the gear reduction, and $T_{cont,i}$ is the maximum continuous torque of the motor.

2. Packing Length Constraint (PLC). The actuators must fit within the allotted space, where net length is the primary concern. Variations in the design could accommodate excess length to some degree, but as rule the length of Actuator #1 should be less than 55mm and the length of Actuators #2 and #3 should be less than 52mm. The PLC is formulated as the amount of available space, or unavailable as the case may be, when the actuator is incorporated in to the robot. In the case of Actuator #1, PLC is formulated as,

$$PLC_1 = 55 - L_1 \quad (3.28)$$

where L_1 is the net length of the actuator. Similarly, the PLC for Actuators #2 and #3 are formulated as,

$$PLC_{2,3} = 52 - L_{2,3} \quad (3.29)$$

Obviously, a feasible actuator has a positive PLC.

3. **Shaft Load Safety Factor (SLSF).** The compactness of the robot necessitates that the gear boxes attached to the motors support the anticipated gear forces. Gear forces applied to the output shaft of the transmission include radial force and subsequent torque. In either case, the SLSF should be at least 1.5 if an infinite life rating is provided by the transmission manufacturer, or 2.5 if only an intermittent transmission rating is provided. In the case of Actuator #1, which drives steering, the SLSF is calculated by,

$$SLSF_1 = \text{minimum} \left(\frac{M_B}{M_R}, \frac{F_r}{F_R} \right) \quad (3.30)$$

where M_B and F_r are the moment and normal loads created by the bevel gear, and M_R and F_R are the rated moment and radial loads of the motor unit. The moment load is calculated as,

$$\begin{aligned} M_B &= d_B F_r \\ &= 7.0 F_r \text{ [mNm]} \end{aligned} \quad (3.31)$$

where $d_B=7.0mm$ is the distance from the bevel gear pitch circle to the gearbox face. The force F_n is determined by,

$$F_r = F_t \tan \psi = \frac{2M_{s1}}{d} \left(\frac{2C}{2C-f} \right) \tan \psi \quad (3.32)$$

$$= 0.11M_{s1} \text{ [N]}$$

M_{s1} (mNm) is the shaft load applied by the motor, $d=7.9mm$ is the pitch diameter of the gear, $f=1.8mm$ is the face width of the gear, and $C=6.5mm$ is the distance from the apex of the bevel gear pair to the far edge of the gear tooth.

Similarly, the shaft load safety factor for Actuators #2 and #3 are determined by the normal forces created by the worm drives. The expression for SLSF for the middle joint is,

$$SLSF_2 = \text{minimum} \left(\frac{M_{BW1}}{M_R}, \frac{F_{rW1}}{F_R} \right) \quad (3.33)$$

Again, M_R and F_R are the rated moment and radial loads of the motor unit, and M_{BW1} and F_{rW1} are the bending moment and normal load created by the worm drive. They are calculated by,

$$M_{BW1} = F_{rW2}d_{w2} \quad (3.34)$$

$$F_{rW2} = \frac{2M_{s2}}{d} \tan \psi \quad (3.35)$$

where $d_{w2}=11mm$ is the axial distance along the worm from the face of the motor unit perpendicular to the center of the worm, $\psi=14.5^\circ$ is the pressure angle of the worm, M_{s2} is the shaft torque created by the motor, and $d=8.5mm$ is the worm pitch diameter. This expression can also be expressed as a function of the required joint torque, M_{w2} , if we also consider the efficiency of the worm drive, $\varepsilon \approx 0.3$, and its reduction ratio $n=20$. The resulting expression is,

$$\begin{aligned}
F_{rw2} &= \frac{2 M_{w2}}{d \epsilon n} \tan \psi \\
&= .010 M_{w2} \text{ [N]}
\end{aligned}
\tag{3.36}$$

This expression also applies to ankle joint 2.

4. **Maximum Power Consumption (MPC).** Assuming that several actuators satisfy the above specifications, final selection of an actuator will be based on a robot with minimal MPC. Power consumption is based on the power requirement necessary for the worst case load conditions at the prescribed JAV. Since DC motors are considered, power consumption, P , is calculated by,

$$P = VI$$

where V is the necessary voltage to achieve the desired output speed. It is determined by required joint speed, and the Speed Constant and gear reduction of the motor under consideration. The current, I , necessary to achieve the joint torque is determined by the efficiency and reduction ratio at the joint, and by the Torque Constant of the motor.

The aforementioned criteria are evaluated with common joint velocities. The joint velocities are determined by the desired walking speed of the robot. During this initial prototype stage where investigative value has overshadowed performance, it has been established that the robot should be capable of completing a complete flipping step in at least than 7.5 seconds. This corresponds to the hip joint moving at 4 RPM, the steering joint moving at 2 RPM, and Ankle #3 moving at 2RPM. Since most actuators are capable of these performance levels, they will serve as an operating point where power consumption is evaluated. The net weight is also evaluated to assure adequate holding capacity of the suction cup feet. It is calculated by summing the weight of all of the robot

components, including the feet, actuators, structural components, and fasteners. Wiring has not been considered. The above criteria will now be applied during the evaluation and selection of actuator units for the climbing robot.

3.6.6 Actuator Selection

Several groups of actuators will now be examined. The analysis will start with the smallest actuators and proceed to larger devices in order to determine a range of feasible units. Groups of actuators with similar size amongst each group will be examined to minimize the number of permutations that must be considered. Units that were totally unrealistic, that is, they could not satisfy the TSF criterion or were far too large, are not discussed.

The size of motors considered range from 10mm diameter to 17mm diameter, and 0.75watts to 3.2watts, respectively. Motor manufacturers with a broad product range, including motor selection, gear heads, and encoders, were the primary concern. These include API Portescap (API-Portescap 1998), Maxon Precision Motors Inc (Maxon-Precision-Motors 1999), and Micro Mo Electronics (Micro-Mo-Electronics 1997). All of these companies provide thorough product data, which is critical during the design stage. Units available through API and Maxon were primarily considered since the units offered by Micro Mo were quite similar to those from Maxon, and Micro Mo's engineering units used throughout their catalog were mixed.

The smallest units examined were the Maxon RE010. They are 10mm diameter, 0.75 watt, planetary-gear (plastic housing) DC motors with digital magnetic encoders. Since joint level feedback was not incorporated into this first prototype, the encoders

Table 9. Maxon motor performance (10mm, .75w, plastic planetary gearbox).

Error! Objects cannot be created from editing field codes.

were necessary to control joint position indirectly. This allowed the use of packaged motor controllers ready to interface with a computer serial port. Using these motors, the net mass of the robot is 235gr, and as Table 9 indicates, they motors satisfy the TSF and PLC. Unfortunately, the plastic housing is unable to support the shaft loads.

The next units examined were the Maxon RE013. They are 13mm diameter DC motors, also with magnetic encoders, and planetary gearboxes with metal housings for higher load capacity. This characteristic is indicated by Table 10 which shows a that the unit has satisfactory TSF and SLSF. In this case, however, the motor unit is too long, as indicated by the negative PLC values, and is not feasible. The 13mm diameter Portescap units shown in Table 11 also have similar capability and also suffer from excess length demonstrated by their PLC values.

Table 10. Maxon motor performance (13mm, 1.2w, metal planetary gearbox).

| Data | Motor #1 | Motor #2 | Motor #3 |
|---------------------------------|---------------|---------------|---------------|
| Model Information | RE013 6V 1.2W | RE013 6V 1.2W | RE013 6V 1.2W |
| Weight, gr | 38 | 35 | 35 |
| Diameter, mm | 13 | 13 | 13 |
| Net Length, mm | 58.4 | 55 | 55 |
| Gear Ratio | 1119 | 275 | 275 |
| Max Radial Load, N | 40 | 40 | 40 |
| Max Shaft Moment, mNm | 240 | 240 | 240 |
| Torque Constant, mNm/A | 3.4 | 3.4 | 3.4 |
| Speed Constant, RPM/volt | 2820 | 2820 | 2820 |
| Torque Safety Factor (TSF) | 4.5 | 5.5 | 6.2 |
| Package Length Constraint (PLC) | -3.4 | -3 | -3 |
| Shaft Load Safety Factor (SLSF) | 1.48 | 12.92 | 14.44 |
| Max. Power Consumption (MPC) | 0.07 | 0.57 | 0.26 |

Table 11. Portescap motor performance (13mm, 2.5w, metal planetary gearbox).

| Data | Motor #1 | Motor #2 | Motor #3 |
|---------------------------------|----------------|----------------|----------------|
| Model Information | 13N88 12V 2.5W | 13N88 12V 2.5W | 13N88 12V 2.5W |
| Weight, gr | 33 | 30 | 30 |
| Diameter, mm | 13 | 13 | 13 |
| Net Length, mm | 67.6 | 63.5 | 63.5 |
| Gear Ratio | 352 | 88 | 88 |
| Max Radial Load, N | 20 | 5 | 5 |
| Max Shaft Moment, mNm | 40 | 40 | 40 |
| Torque Constant, mNm/A | 9.1 | 9.1 | 9.1 |
| Speed Constant, RPM/volt | 1053 | 1053 | 1053 |
| Torque Safety Factor (TSF) | 3.2 | 4.4 | 5.8 |
| Package Length Constraint (PLC) | -12.6 | -11.5 | -11.5 |
| Shaft Load Safety Factor (SLSF) | 0.90 | 1.96 | 2.21 |
| Max. Power Consumption (MPC) | 0.08 | 0.55 | 0.21 |

Table 12. Portescap motor performance (17mm, 3.2w, metal planetary gearbox).

| Data | Motor #1 | Motor #2 | Motor #3 |
|---------------------------------|---------------|---------------|---------------|
| Model Information | 17N88-208P 6V | 17N88-208P 6V | 17N88-208P 6V |
| Weight, gr | 43 | 43 | 43 |
| Diameter, mm | 17 | 17 | 17 |
| Net Length, mm | 53.8 | 49.7 | 49.7 |
| Gear Ratio | 166 | 30.2 | 30.2 |
| Max Radial Load, N | 20 | 20 | 5 |
| Max Shaft Moment, mNm | 160 | 160 | 40 |
| Torque Constant, mNm/A | 7.2 | 7.2 | 7.2 |
| Speed Constant, RPM/volt | 1333 | 1333 | 1333 |
| Torque Safety Factor (TSF) | 2.8 | 2.8 | 3.1 |
| Package Length Constraint (PLC) | 1.2 | 2.3 | 2.3 |
| Shaft Load Safety Factor (SLSF) | 0.81 | 7.10 | 8.00 |
| Max. Power Consumption (MPC) | 0.07 | 0.52 | 0.23 |

Since the larger units available from Maxon continue to violate the PLC constraint, larger units from Portescap were examined. The next units evaluated were 17mm Portescap 17N88 geared DC motors with metal planetary gearing and optional ball bearing or bushing output shaft support. As Table 12 indicates, these units satisfy the TSF and PLC requirements very well. The optional ball bearing shaft support is used on Motor #2 for a SLSF of 7.1 and the bushing SLSF is used on Motor #3 for a SLSF of approximately 2.0. The ball bearing support is also used on Motor #1, but due to the high loads on the bevel gearing, the SLSF is only 0.8, which is risky for short term operation even though these ratings are based on infinite life. The only motor that had a reasonable SLSF=1.5 on this joint was the Maxon RE013 with metal gearbox, but it was 4mm too long.

A compromise had to be made for the sake of producing a prototype rapidly, and the Portescap 17N88 actuators were selected. The weakness of the steering actuator was deemed acceptable for short term operation, and the design could be perfected during the next stage of research.

3.6.7 Structural Optimization

Now that the final actuators have been established, the structure of the robot can be examined to assure that it can support the given loads and to determine if its weight can be further minimized. The holes that have been shown on the structure until this point are actually a product of these efforts. Prior to the analysis, however, the joint loads must be examined one last time for the purpose of applying Finite Element Analysis (FEA) to the structure.

The robot is once again considered climbing a vertical surface in a straight, cantilevered, orientation as shown in Figure 29. Unlike the case of the actuator investigations, shown in Figure 26, the robot is turned 90° about its longitudinal axis such that the bending moments are applied to the links to exploit their weakest bending strength. This configuration and corresponding boundary conditions are shown in Figure 29. The boundary conditions consist of the Joint loads and appropriate anchor points created by

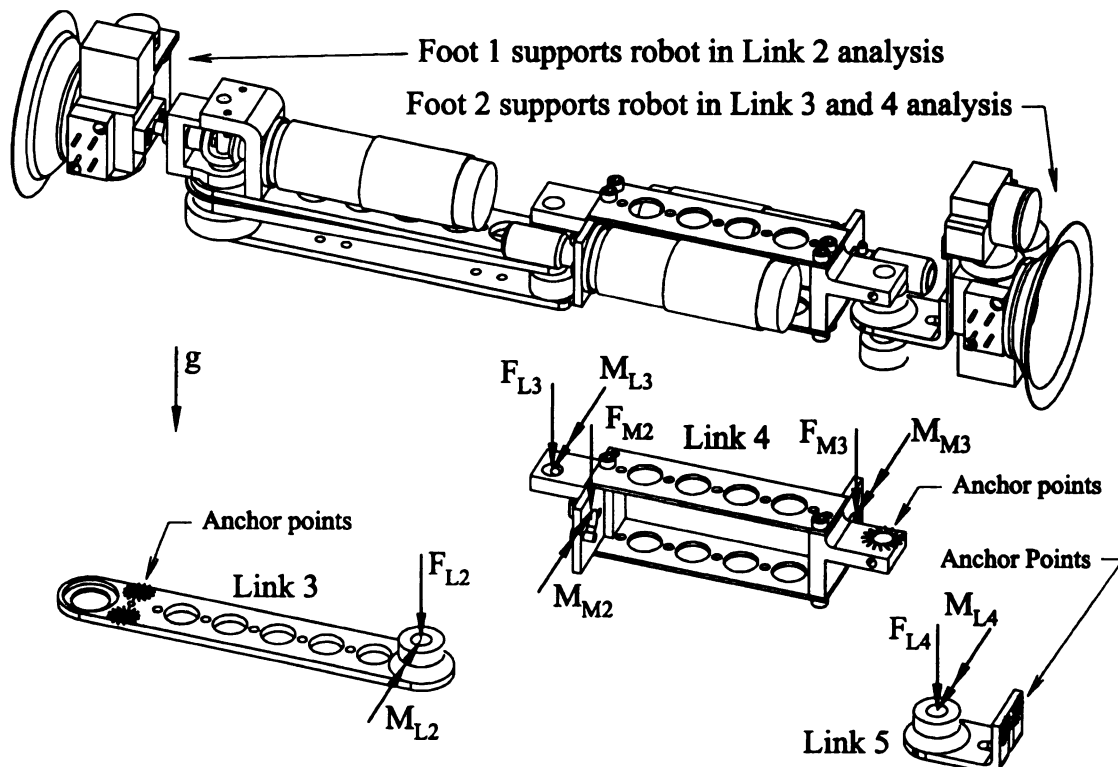


Figure 29. Diagram of robot Boundary Conditions used for Structural Analysis

the structure. For the sake of worst-case load conditions, it is assumed during the analysis of Link #2 that the robot is supported by Foot #1, that the strut provides no support, all resistance to bending is provided by the motor mount locations, and that the preload of the belt has no effect. Supporting the robot by Foot #1 creates the largest bending moments in the link.

Based on structural components manufactured from Aluminum 6061 with an untempered yield strength of 8 ksi, the effective force, F_{L2} , and moment, M_{L2} , applied to Link 3 are determined to be,

$$F_{L2} = W_3 + W_4 = 1.94 \text{ N} \quad (3.37)$$

$$M_{L2} = W_3 d_3 + W_4 (L_3 + d_4) = 136 \text{ mNm} \quad (3.38)$$

In the analysis of Links 4 and 5, it is assumed that Foot #2 supports the robot. This creates the largest forces on these members. Contributions of the motors to the loading of Link 4 have been depicted as F_{M1} , F_{M2} , M_{M1} , M_{M2} where,

$$F_{M1} = F_{M2} = 0.42 \text{ N} \quad (3.39)$$

$$M_{M2} = M_{M3} = 11.3 \text{ mNm} \quad (3.40)$$

The external force and moments applied to Link #4 are,

$$F_{L3} = W_1 + W_D + W_2 = 1.41 \text{ N} \quad (3.41)$$

$$M_{L3} = W_2 (L_2 - d_2) + W_1 (L_2 + d_1) + W_D (L_2 + d_D) = 99.7 \text{ mNm} \quad (3.42)$$

and the external forces and moments applied to Link #5 are,

$$F_{L4} = W_1 + W_D + W_2 + W_3 = 2.63 \text{ N} \quad (3.43)$$

$$M_{L4} = W_2(L_2 + L_3 - d_2) + W_1(L_2 + L_3 + d_1) + W_D(L_2 + L_3 + d_D) + W_3(L_3 - d_3) = 263 \text{ mNm} \quad (3.44)$$

The final analysis of Link #3 is shown in Figure 30. As the image indicates, the largest stresses occur near the motor bracket mount location, which is anticipated because that is the anchor location, indicated in , for the link. There are five 7.9mm diameter holes in the link to reduce the weight of the link by 1.4gr, a 19% decrease in mass of the link. The maximum stress is 1.9 ksi, which provides a safety factor of 4.2.

The final analysis of Link #4 is shown in Figure 31. Eight 7.9mm diameter holes have been added to the upper and lower plates to decrease the weight by 1.1gr, an 8% decrease in structural weight of the link. The maximum stress of 2.7 ksi occurs in the motor brackets near the joint supports. This provides a safety factor of 3.0 with Aluminum

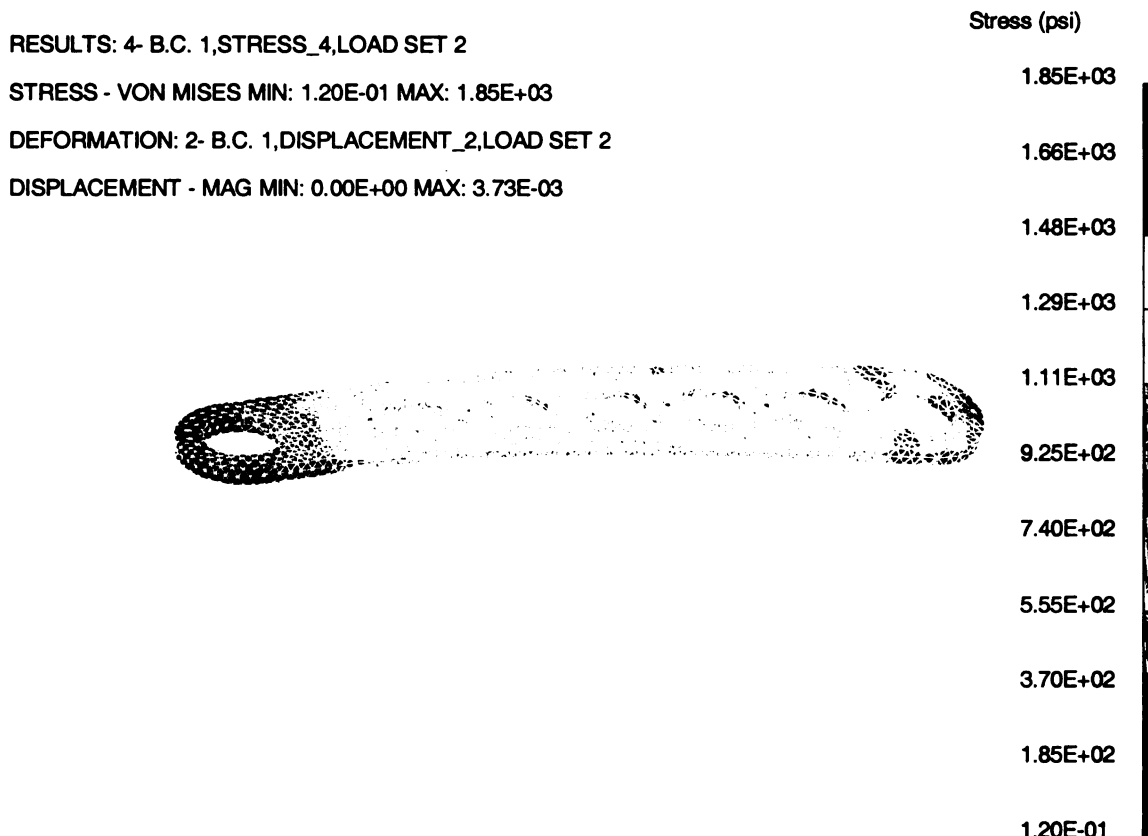


Figure 30. FEM analysis of Link 3 subjected to maximum loading.

6061, or a safety factor of 5.6 using stronger Aluminum 7075 with an un-tempered yield strength of 15ksi.

The final analysis of Link 5 is shown in Figure 32. It has a maximum stress of 7.6 ksi for a safety factor of 1.97 using Aluminum 7075, which is necessary with this part. Some large stresses are shown near the worm gear mounting pocket, but those can be attributed to the application of point loads. Maximum stresses occur at the opposite end of the link, near the foot. These are due to large bending moments. These could be averted by webbed side structures added to the link, if the aforementioned stresses result in deformation. Deflection in all of these results was determined to be minimal, with at most .004".

RESULTS: 2- B.C. 1,STRESS_2,LOAD SET 1

STRESS - VON MISES MIN: 5.11E+00 MAX: 2.63E+03

DEFORMATION: 1- B.C. 1,DISPLACEMENT_1,LOAD SET

DISPLACEMENT - MAG MIN: 0.00E+00 MAX: 2.87E-03

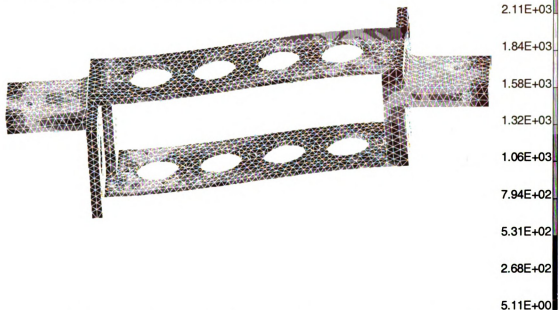


Figure 31. FEM analysis of Link 4 subjected to maximum loading.

RESULTS: 2- B.C. 1,STRESS_2,LOAD SET 1

STRESS - VON MISES MIN: 8.04E+01 MAX: 7.56E+03

FRAME OF REF: PART

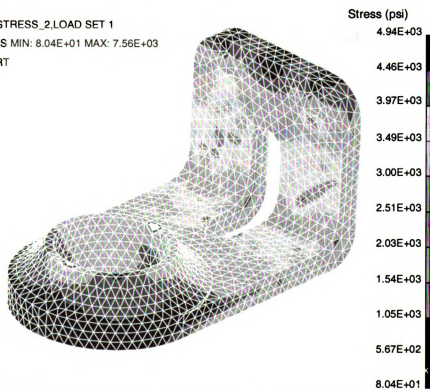


Figure 32. FEM analysis of Link 5 subjected to maximum loading.

3.7 Testing

The robot was tested climbing on a vertical surface, walking on a horizontal surface, walking between a horizontal and vertical surfaces (crossing a 90° corner), and walking between specified locations on a vertical surface (Minor et al 2000, Dulimarta et al. 2000). During the walking and climbing tests on horizontal and vertical surfaces, respectively, the robot started from an initial position and walked a specified number of steps. A sequence of pictures of the robot climbing a vertical surface is shown in Figure 33, Figure 34, and Figure 35. The robot performed these tasks with no difficulties. Only a small amount of uncertainty was encountered when placing the foot at the end of the step, and varying the joint angle slightly until the foot was secured on the surface counteracted this.

One of the most difficult tasks was walking between specified locations on a vertical surface. While walking between points, the robot was to follow a path on the surface to a final destination. This task involved walking vertically up the surface, turning 90°, walking across the surface several steps, turning 90°, and walking up the surface another two steps. Uncertainty of the steering angle played a major role while the robot was walking across the surface since gravity tended to turn towards the ground. A joint level potentiometer was incorporated to offset this effect.

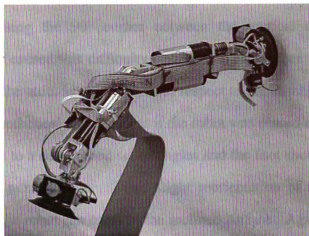
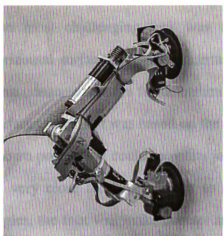


Figure 33. Biped climbing a vertical surface. Start position and beginning of motion.



Figure 34. Biped climbing a vertical surface, halfway through step.

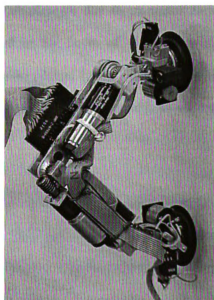
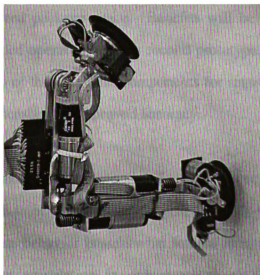


Figure 35. Biped climbing a vertical surface. Near end of step and final position.

The most challenging task was crossing the 90° corner between the vertical and horizontal surfaces. Again, uncertainty caused this difficulty because the robot does not have adequate sensors for determining the attitude of its feet with respect to the climbing surfaces. Our test was based on the hypothetical situation that if the robot was placed in a known position, it could move its joints to a determined set of angles and the foot should be very close to perpendicular to the next surface. With slight reorientation of the angles, the foot will make contact and the robot can cross to the inclined surface. Again, however, since joint level control is not used, backlash affects the joint angles and the final position of the foot will not quite be perpendicular. The affects of gravity and compliance in the feet also add to this problem. Hence, until sensors such as feelers or proximity sensors, are incorporated into the robot, climbing between surfaces will be difficult.

3.8 Future Work

Research during the next stage of this project will proceed in two directions. One focus will be the further miniaturization of the aforementioned climbing robot to about half its current size. This will provide formidable design challenges due to miniaturization and restricted package space. Benefits will be reaped in the form of weight savings and extended operability. This second prototype will also permit further exploration into the design of the structural components for improved rigidity and efficiency, as well as joint level sensors for improved accuracy.

The second, and more significant, research focus will be on the development of the hybrid joint. While the proposed joint permits prismatic and revolute behavior, its revolute behavior is somewhat limited in range of motion. In fact, the hybrid joint only permits articulation in one direction, albeit between zero and 120°. This limited

articulation allows the robot to cross 90° and 270° corners satisfactorily and perform the crawling and sliding walking strides. It does not, however, permit the robot to perform the flipping stride effectively. Incorporation of joint level sensors into this design will be very challenging.

3.9 Other Considerations

In this chapter, design of a climbing robot for superior mobility under significant limitations on available space and power has been studied. The robot developed is capable of adapting to walking or climbing on vertical or horizontal surfaces, traversing between surfaces with various inclinations, and also steering to any point on a surface. The robot designed is motivated towards being the smallest robot of its nature and possessing an adaptable structure to allow the robot to traverse confined spaces as well as rapidly across surfaces. A conceptual hybrid prismatic-revolute joint was presented for this purpose. The initial robot, however, for the sake of rapid exploration, was built two times scale and with only a revolute hip joint. This allowed a prototype to be built rapidly and reliably, and to permit the exploration of coupled DOF for reduced weight. An analysis of the force in the robot was then conducted to determine the set of feasible actuators, and then a FEM analysis of the structure was performed to assure adequate strength and provide further weight reductions.

Design of the robot emphasized many important points, only some of which were encountered during design of the surgical instrument. Like the surgical instrument design, the climbing robot design required design innovations combined with engineering analysis and optimization to determine the most adaptable and trustworthy kinematics structure. Unlike the surgical instrument, however, weight, actuation, and power usage are major issues for the climbing robot. This is partially attributed to limited holding

capacity of the suction feet, which in turn limit space and weight available for the power supply and actuators. Also unlike the surgical instrument, the actuators themselves play a major role in the design; both in terms of the weight that they contribute and the loads that they can support. As such, a balance between actuator weight and capacity had to be achieved, which ultimately resulted in the actuators contributing to almost 50% of the robot weight, whereas the robot frame only contributed to 10% of the weight. While this may not be the case with less constrained robots, it certainly was an issue here. This application of mobile robotics makes it very clear that actuator weight is one of the major issues in designing mobile robots and we pursued designs based on under actuation. Future advances in mobile robot design will be accomplished with further research on under-actuated mechanisms and development of actuators with higher power to weight ratios.

4. Control of a Spherical Robot for Enhanced Mobility

4.1 Motivation

In the previous chapters, the focus was design for dexterity and mobility given constraints on space, weight, and power. In this chapter, an equally important limitation is addressed during the design of a mobile robot: control of a robot for maximized mobility given limited computational ability. Since the wall-climbing robot possesses straightforward kinematics, computational usage for control and motion planning is not an issue. To address computational usage directly, a particular system is chosen with substantial nonlinear constraints that do not readily present a solution. The task at hand is point-to-point reconfiguration of a spherical robot. Such a robot has highly nonlinear nonholonomic rolling constraints, and traditional non-linear control techniques are not applicable. Several techniques have been presented in the literature, but in this chapter we develop a simpler and less computationally demanding algorithm for controlling the sphere. We now examine the problem closely.

Traditionally, mobile robots have employed multiple wheels for locomotion and stability. In contrast, the spherical robot discussed here relies on its outer shell for mobility and support. The robot, named Spherobot, is shown in a sectional view in Figure 36. Notice that the robot uses a central body with reciprocating masses supported on radial spokes in a tetrahedral arrangement. These masses cause the robot to roll when their position and accelerations impart a reactive moment on the robot body. In this conception, the robot also provides a retractable camera for reconnaissance purposes and retractable limbs that provide stability while the camera is in use. Additional end-effectors and sensors can be incorporated to provide functionality for retrieving specimens or detecting

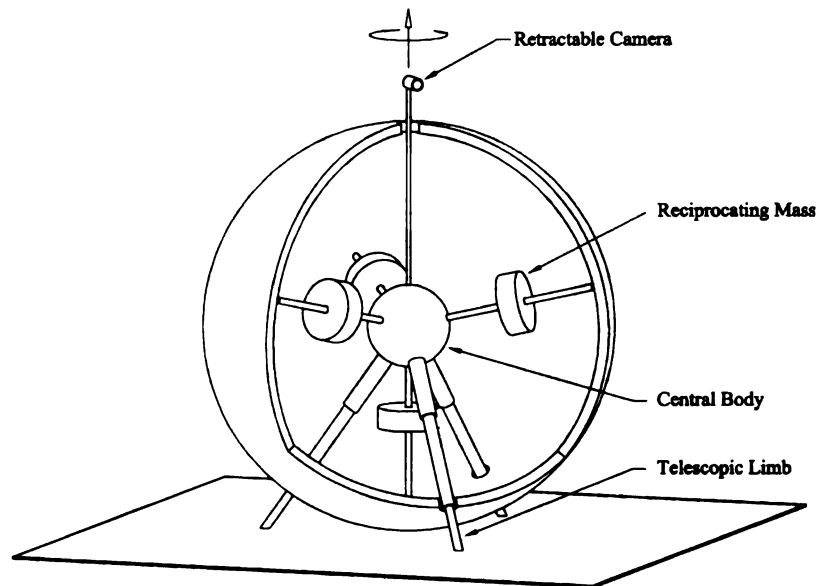


Figure 36. Spherobot Mobile Robot.

chemical/nuclear threats. The sturdy exoskeleton provides protection for the robot in hostile conditions.

Spherobot is not the first spherical robot to be conceived. To date in the literature, this honor belongs to (Halme, Schonberg, et al. 1996), whose spherical robot contains a single-wheeled device that drives around inside the sphere to create a rolling moment by offsetting the sphere's center of gravity. A similar concept was soon after exploited by the Sphericle (Bicchi, Balluchi, et al. 1997), which uses a car driving around inside the sphere to create the propelling moments. Because of the rolling nature of the mechanisms used to drive the counterweights, both robots have additional nonholonomic constraints that limit mobility and complicate control strategies. The reciprocating masses used in Spherobot can shift their cumulative center of gravity and acceleration in any direction at any time, which provides superior mobility.

In this chapter, our endeavor is to create simple control strategies for moving Spherobot to a specified location and orientation. The challenge of this task is created by the non-slip rolling constraints, referred to as nonholonomic constraints, which prevent direct

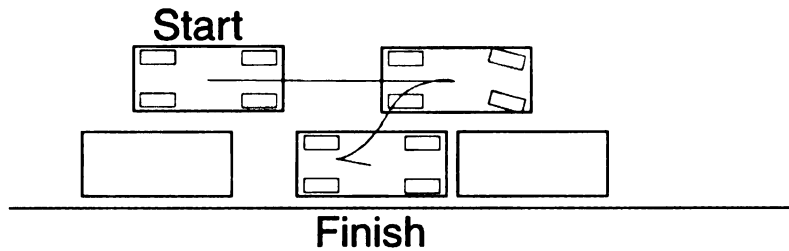


Figure 37. Nonholonomic constraints: parallel parking.

linear motion to the prescribed final position and orientation. The parallel parking of an automobile, shown in Figure 37, is a simple example of nonholonomic constraints. The tires of the automobile prevent the vehicle from moving directly sideways into the parking space. Rather, the vehicle must steer along a complex curve to reach its parallel parking space. While rolling SpheroBot to its final destination, similar, but more complicated, constraints are encountered. This subject has even gained a classical name in the literature: the ball and plate problem.

In recent years, numerous researchers have studied the ball and plate problem. In 1990, Li and Canny (Li and Canny 1990) considered the problem in the context of rolling surfaces. They showed that the system was controllable and they also defined a three step algorithm for completing the task. The first step converges the position coordinates. The second step converges two of the three orientation coordinates using Lie Bracket motions, which create a spherical triangle on the surface of the sphere. The last step uses a circular trajectory to converge the third orientation variable. More recently, Bicchi (Bicchi, Prattichizzo, et al. 1995) investigated a technique, with limited success, that applied a series of piecewise independent controls and then integrated the state equations to solve for the magnitude of each of the pieces. Mukherjee (Mukherjee and Minor 1999; Mukherjee, Minor, et al. 1999) later presented two algorithms based on spherical trigonometry and on the geometry created by the motion of the sphere on the plane to achieve controllability. The later will be discussed further in this chapter. Optimal

control, in the sense of control effort minimization, of the open loop problem has been addressed by Jurdjevic (Jurdjevic 1993).

As the parallel parking example points out, direct motion between initial and final configurations is not likely, and the first question that must be answered is whether a path exists between the specified orientations. This will be one of the first subjects that are addressed. A proof of existence of a path requires a mathematical model of the sphere's kinematics, which will first be developed in Section 4.2. The existence of a path between configurations will be discussed in Section 4.3. In section 4.4, other kinematics models in the literature are reviewed. Then the application of traditional nonholonomic control techniques are discussed in Section 4.5. We present our motion planner in Section 4.6. Simulation results are presented in to demonstrate the efficacy of the motion planner in Section 4.6.4.

4.2 Kinematics Model

Consider Spherobot on the x - y plane, shown in Figure 38. The position of the sphere is determined by the point Q , at the center of the sphere, relative to a globally fixed Cartesian coordinate system with its origin at point O . It is assumed that the sphere rolls on the $\{x, y\}$ plane without slipping or spinning. Orientation of the sphere is determined relative to point P on the surface of the sphere. A new Cartesian system $\{x', y'\}$ is established by rotation about the z axis by angle α , $-\pi \leq \alpha \leq \pi$, such that P lies in the x' - z plane directly above the x' axis. The elevation of point P is described by the angle θ , $0 \leq \theta \leq \pi$, measured about the y' axis relative to the z -axis. Control inputs consisting of angular velocities, ω'_x and ω'_y , are aligned with the x' and y' axis, respectively. The position of the sphere is described in the x - y plane by the vector, \mathbf{R}_{OQ} ,

$$\mathbf{R}_{OQ} = \{x, y\} \quad (4.1)$$

As indicated by Figure 39 the sphere contacts the plane at point R , and the velocity of

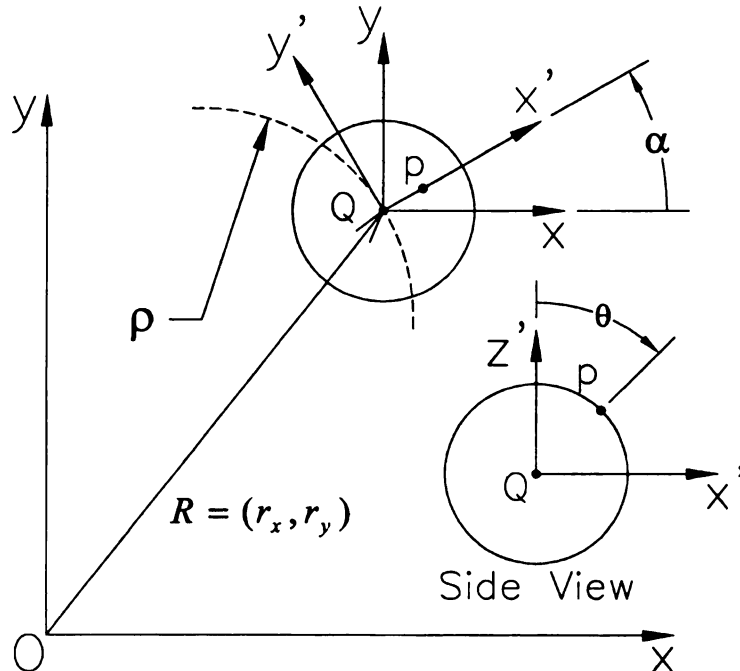


Figure 38. Spherobot Coordinate System.

point Q relative to the plane can be determined by,

$$\dot{R}_{OQ} = \begin{Bmatrix} \dot{x} \\ \dot{y} \end{Bmatrix} = \dot{R}_{QR} = \omega \times R_{RQ} = \begin{Bmatrix} \omega_y \\ -\omega_x \end{Bmatrix} \quad (4.2)$$

where $\{(x, y) \in \mathbb{R}^2\}$. The control inputs ω_x and ω_y can then be expressed relative to the x' and y' axis by the transformation:

$$\begin{Bmatrix} \omega_x \\ \omega_y \end{Bmatrix} = \begin{bmatrix} \cos \alpha & -\sin \alpha \\ \sin \alpha & \cos \alpha \end{bmatrix} \begin{Bmatrix} \omega'_x \\ \omega'_y \end{Bmatrix} \quad (4.3)$$

Applying this transformation to Equation (4.2) yields,

$$\begin{bmatrix} \dot{x} \\ \dot{y} \end{bmatrix} = \begin{bmatrix} \sin \alpha \\ -\cos \alpha \end{bmatrix} \omega'_x + \begin{bmatrix} \cos \alpha \\ \sin \alpha \end{bmatrix} \omega'_y \quad (4.4)$$

State equations for α and θ are derived from the position vector R_{QP} ,

$$R_{PQ} = \{\sin \theta \cos \alpha \quad \sin \theta \sin \alpha \quad \cos \theta\}^T \quad (4.5)$$

Taking the time derivative of the position vector yields the relative velocity vector,

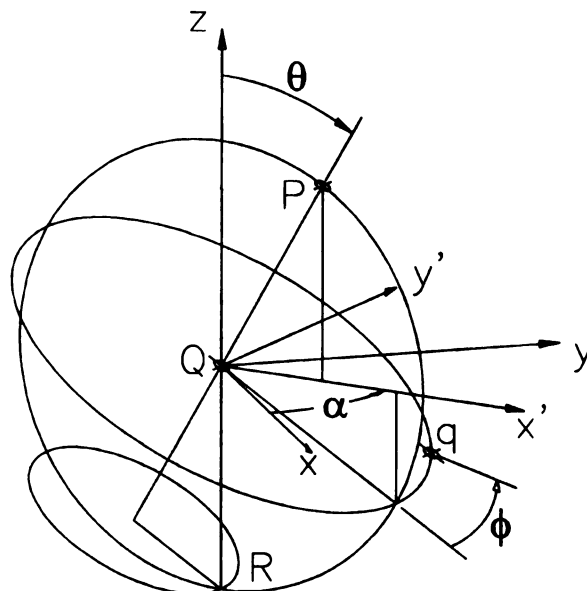


Figure 39. Spherobot Orientation Variables.

$$\dot{R}_{PQ} = \begin{Bmatrix} \dot{\theta} \cos \theta \cos \alpha - \dot{\alpha} \sin \theta \sin \alpha \\ \dot{\theta} \cos \theta \sin \alpha - \dot{\alpha} \sin \theta \cos \alpha \\ -\dot{\theta} \sin \theta \end{Bmatrix} \quad (4.6)$$

Note, however, that these velocities are created by the control inputs ω'_x and ω'_y . The velocity vector can then be expressed as a function of the control inputs as,

$$\dot{R}_{PQ} = \omega \times R_{PQ} = \begin{Bmatrix} \omega'_x \sin \alpha \cos \theta + \omega'_y \cos \alpha \cos \theta \\ \omega'_x \cos \alpha \cos \theta + \omega'_y \sin \alpha \cos \theta \\ -\omega'_y \sin \theta \end{Bmatrix} \quad (4.7)$$

Equating terms of Equations (4.6) and (4.7) yields,

$$\dot{\theta} = \omega'_y \quad (4.8)$$

$$\dot{\alpha} = -\omega'_x \cot \theta \quad (4.9)$$

where $\{\theta \in \mathbb{R}^1 \mid -\pi < \theta < \pi, \theta \neq 0\}$ and $\alpha \in \mathbb{R}^1$. The input ω'_x also causes the sphere to rotate about the axis QP, which results in a change of the orientation variable ϕ determined by,

$$\dot{\phi} = \omega'_x \frac{1}{\sin \theta} = \omega'_x \csc \theta \quad (4.10)$$

Together, the position and orientation variables then form a state model, which completely describes the sphere rolling on a plane:

$$\begin{bmatrix} \dot{x} \\ \dot{y} \\ \dot{\theta} \\ \dot{\alpha} \\ \dot{\phi} \end{bmatrix} = \begin{bmatrix} \sin \alpha \\ -\cos \alpha \\ 0 \\ -\cot \theta \\ \csc \theta \end{bmatrix} \omega'_x + \begin{bmatrix} \cos \alpha \\ \sin \alpha \\ 1 \\ 0 \\ 0 \end{bmatrix} \omega'_y \quad (4.11)$$

$$\equiv X_1 \omega'_x + X_2 \omega'_y.$$

Note that as $\theta \rightarrow 0$ or $\pm\pi$, three things occur. First, the rate of change of α and ϕ become extremely sensitive to input in the ω'_x direction. This is demonstrated by,

$$X_1(\theta \approx 0) = [\sin \alpha \quad -\cos \alpha \quad 0 \quad -\infty \quad \infty]$$

To maintain boundedness of α and ϕ near this point, control $u_1 = \omega'_x$ must become very small and actually go to zero at $\theta = 0$ or $\pm\pi$. This could be accomplished by a coordinate transformation such as,

$$\omega'_x = \hat{\omega}_x \sin \theta \tag{4.12}$$

Secondly, note that the orientation of ω'_x is defined by the angle α formed by the position of point P above the x-y plane, Figure 39. The angle α becomes undefined when $\theta = 0$ since P is directly above, or below, the center of the sphere. As a mathematical state variable, however, α will retain its value when $\theta = 0$ as long as $\omega'_x = 0$. Hence, in a practical application, there is no reason why ω'_x could not be used to drive $\theta \rightarrow 0$ or $\pm\pi$. In fact, since α is not clearly defined when $\theta = 0$, α could just as conveniently be assigned to a new value that might define a more desirable orientation of ω'_x and ω'_y . This point will be exploited in Section 4.6.3 for the definition of a full reconfiguration motion-planning algorithm. Thus, the limitations of set M will actually be exploited rather advantageously.

A third consideration, and probably most important, regarding $\theta = 0$ or $\pm\pi$ must also be discussed. Consider the point P on the surface of the sphere. Normally, when $\theta \neq 0$ or $\pm\pi$, both variables α and θ are required to describe the longitude and latitude of point P. However, when $\theta \rightarrow 0$ or $\pm\pi$, the point P is at the topmost, or bottommost, position of the sphere, and α becomes poorly defined. Note, however, that when P is at these extreme positions α is not necessary for describing the point's position. Hence, at

these two extreme locations, the α state variable is unnecessary, and the system could be reduced to a four state model! This aspect is key in the complete reconfiguration algorithm discussed in Section 4.6.3 where the point P is brought to the topmost position during the algorithm.

The sphere's path curvature on the plane is determined by

$$\begin{aligned}\rho^2(t) &= \frac{[\dot{x}^2 + \dot{y}^2]^3}{[\dot{x}\ddot{y} - \dot{y}\ddot{x}]^2} \\ &= \frac{[\omega_x'^2 + \omega_y'^2]^3}{[-\omega_x'^3 \cot \theta + \omega_x' \dot{\omega}_y' - \omega_y' \dot{\omega}_x' - \omega_y'^2 \omega_x' \cot \theta]^2}\end{aligned}\tag{4.13}$$

If $\omega_y' \neq 0$ and $\omega_x' = 0$, then the curvature is infinite which is the case of linear motion in the x' direction. Conversely, if $\omega_x' \neq 0$ and $\omega_y' = 0$, it can be shown that curvilinear motion is created, indicated in Figure 38, and is described by,

$$\rho = \tan \theta\tag{4.14}$$

Motion planning strategies presented later exploit these curved and linear paths to derive methods for converging the sphere to a specified final orientation and position. When applying such independent controls, the α and ϕ states can be expressed as dependent functions,

$$\dot{\phi} = -\dot{\alpha} \sec \theta\tag{4.15}$$

and the state model can be reduced for simplicity to,

$$\begin{aligned}
\dot{x} &= \omega'_y \cos \alpha + \omega'_x \sin \alpha \\
\dot{y} &= \omega'_y \sin \alpha - \omega'_x \cos \alpha \\
\dot{\theta} &= \omega'_y \\
\dot{\alpha} &= -\omega'_x \cot \theta
\end{aligned} \tag{4.16}$$

where a desired change in ϕ can be determined as a function of α and θ during the motion planning stages.

4.3 Reachability of Arbitrary Configurations

Since we assume that no slip is present in the sphere's motion, the state model of the sphere is of the form of a drift free system. Reachability of arbitrary configurations of such a system is determined by first considering a generic drift free system with multiple inputs of the form,

$$\dot{p} = \sum_{i=1}^m u_i X_i(p) = u_1 X_1(p) + u_2 X_2(p) + \dots + u_m X_m(p) \tag{4.17}$$

Herman and Krener (Halme, Schonberg, et al. 1996; Hermann and Krener 1977) discuss many valuable concepts regarding controllability of such a system. In the context of a system in the form of Equation (4.17) defined on a set $M \subseteq \mathfrak{R}^n$, define $A(p_0)$ as the set of points that are accessible from an initial point, $p_0 \in M$. If $A(p_0) = M$, it is said that the system is controllable at x_0 , and if $A(p) = M \forall p \in M$, it is said that the system is controllable over the set. Controllability is determined by Hermann and Krener (Halme, Schonberg, et al. 1996; Hermann and Krener 1977) and elsewhere in the literature using Chow's Theorem (Chow 1939), with some modifications (Li and Canny 1990).

The theorem begins with a drift free system of the form of Equation (4.17) where $p \in M \subseteq R^n \equiv R^5$, $U = [u_1 \dots u_m] \in N \subseteq R^m \equiv R^2$. Then, based on the control vectors

X_i , establish the lie distribution $\nabla(p)$. In the case of a two input five state model, we have,

$$\begin{aligned}\nabla(p) &= \text{span}[X_1 \quad X_2 \quad X_3 \quad X_4 \quad X_5] \\ X_3 &= [X_1, X_2] = \frac{\partial X_2}{\partial p} g_1 - \frac{\partial X_1}{\partial p} g_2 \\ X_4 &= [X_1, X_3] \\ X_5 &= [X_2, X_3]\end{aligned}\tag{4.18}$$

If the $\text{rank}(\nabla(p)) = n \forall p \in M$, then the controllability rank condition is satisfied and the system is weakly controllable over the set M . Loosely speaking, weak controllability over a set will guarantee that a path exists between points in the set, but that the time required for completing that path may not be finite. Of course it is also required that the system (4.17) be well defined over M such that a solution to the differential equations exists.

Recall from Equation (4.11) that the model of Spherobot is controlled by the vectors

$$\begin{aligned}X_1 &= [\sin \alpha \quad -\cos \alpha \quad 0 \quad -\cot \theta \quad \csc \theta] \\ X_2 &= [\cos \alpha \quad \sin \alpha \quad 1 \quad 0 \quad 0]\end{aligned}$$

where

$$M = \{[x, y, \alpha, \theta, \phi] \in \mathbb{R}^5 \mid -\pi < \theta < \pi, \theta \neq 0\}.\tag{4.19}$$

Note that M is defined in a way such that X_1 is bounded over the set and its integral is well defined. In practicality, however, this restriction does not mean that $\theta = 0$ or $\pm \pi$ cannot be reached by the system. Clearly the control vector X_2 permits full control of θ , regardless of its value, but a few subtle points must be considered. First, as pointed out in Section 4.4, the primary purpose in limiting M is to assure that the state model, in

particular α , is well defined. This is easily managed by assuring that $\omega'_x = 0$ when $\theta = 0$ or $\pm\pi$, as prescribed in Section 4.4 via Equation (4.12). Secondly, the limitation that $\omega'_x = 0$ does not necessarily mean that the system can only be steered in a single direction. Recall that α is not well defined in this situation, implying that it could take on any value, and hence it can be arbitrarily assigned such that ω'_y has a desirable direction. This property is exploited later in the full reconfiguration algorithm, Section 4.6.3, to steer the sphere in a new direction when $\theta = 0$. It can thus be argued that the application of Chow's theorem, will provide proof of controllability over M , but that set M will not necessarily be the only controllable region.

Per application of Chow's Theorem, controllability over M can be proven by examining the dimension of the lie distribution described by Equation (4.18). First calculate X_3 via the Lie bracket of X_1 and X_2 ,

$$\begin{aligned} X_3 &\equiv [X_1, X_2] \\ &= [\sin \alpha \cot \theta \quad -\cos \alpha \cot \theta \quad 0 \quad -1 - \cot^2 \theta \quad \csc \theta \cot \theta]^T \end{aligned} \quad (4.20)$$

then X_4 is calculated similarly by the Lie bracket of X_1 and X_3 ,

$$X_4 \equiv [X_1, X_3] = [\cos \alpha \quad \sin \alpha \quad 0 \quad 0 \quad 0]^T \quad (4.21)$$

and then finally X_5 ,

$$\begin{aligned} X_5 &\equiv [X_2, X_3] \\ &= [-2\sin \alpha(1 - \cot^2 \theta), 2\cos \alpha(1 + \cot^2 \theta), \\ &\quad 0, 2\cot \theta(1 + \cot^2 \theta), -2\csc \theta(1 + \cot^2 \theta)]^T \end{aligned} \quad (4.22)$$

Using these vectors, the distribution ∇ is formed:

$$\nabla = \begin{bmatrix} \sin \alpha & \cos \alpha & \sin \alpha \cot \theta & \cos \alpha & -2 \sin \alpha (1 + \cot^2 \theta) \\ -\cos \alpha & \sin \alpha & -\cos \alpha \cot \theta & \sin \alpha & 2 \cos \alpha (1 + \cot^2 \theta) \\ 0 & 1 & 0 & 0 & 0 \\ -\cot \theta & 0 & -(1 + \cot^2 \theta) & 0 & 2 \cot \theta (1 + \cot^2 \theta) \\ \csc \theta & 0 & \csc \theta \cot \theta & 0 & 2 \csc \theta (1 + \cot^2 \theta) \end{bmatrix} \quad (4.23)$$

and the determinant of the distribution is,

$$\det \nabla = -\csc \theta \quad (4.24)$$

Since (4.24) is well defined and non-zero over M , it is concluded that ∇ maintains full rank. According to Chow's theorem, the system is controllable between any prescribed configurations in M . A similar conclusion follows for the reduced order system described by Equation (4.16). The Lie distribution for this system is,

$$\nabla_{reduced} = [X_1 \quad X_2 \quad X_3 \quad X_4] = \begin{bmatrix} \sin \alpha & \cos \alpha & \sin \alpha \cot \theta & \cos \alpha \\ -\cos \alpha & \sin \alpha & -\cos \alpha \cot \theta & \sin \alpha \\ 0 & 1 & 0 & 0 \\ -\cot \theta & 0 & -1 - \cot^2 \theta & 0 \end{bmatrix} \quad (4.25)$$

which has full rank over M , as the determinant indicates:

$$\det \nabla_{reduced} = 1 \quad (4.26)$$

Thus, the reduced order system is also controllable over M . It can be argued further that the reduced order system can also be used for complete reconfiguration of the system. Recall Equation (4.15), which demonstrates coupling between α and ϕ when the system is subjected to ω'_x alone:

$$\dot{\phi} = -\dot{\alpha} \sec \theta \quad (4.15)$$

Later in this chapter, section 4.6.3, an algorithm will be specified that exploits this property to drive the system from some random initial configuration to one with $\theta = 0$

where the value of α is irrelevant for describing the sphere's orientation. Since α is unnecessary for describing this final position, the variable α can be used with Equation (4.15) to yield a desired final ϕ . Thus, the system can be completely reconfigured via the reduced order system. Reconfiguration to final positions with $\theta \neq 0$ can be accommodated via a coordinate transformation in θ and ϕ that would place a different point, say P' , to the topmost position on the sphere.

4.4 Kinematics Models in the Literature

The rolling constraints imposed above are identical to those in the controls literature referring to the classical ball and plate problem (Bloch and Crouch 1995; Brockett and Dai 1993; Jurdjevic 1993), and the more general rolling contact of rigid bodies problem (Bicchi, Prattichizzo, et al. 1995; Li and Canny 1990). In the ball and plate problem, locomotion is achieved by relative motion of two parallel plates on opposite sides of the sphere in non-slip contact. The rolling contact problem typically does not discuss actuation. In the case of Spherobot, locomotion is achieved by positioning internal masses such that an unbalance is generated, which creates a driving moment and rolling motion on the plane is achieved.

In these other works, different methods have been used to describe the orientation of the sphere. As the reader will recall from Section 4.2, the definition of the kinematics model can yield very beneficial behavior that can be exploited for control design. The formulation used by Li and Canny (Li and Canny 1990) tracks the contact point between the surfaces of the sphere and plane in \mathbb{R}^4 and establishes a fifth variable ψ for contact angle. Spherical coordinates $\{u_1, v_1\}$ and Cartesian coordinates $\{u_2, v_2\}$ determine the contact point on the surface of the sphere and plane, respectively. Angle ψ measures the angle between the x-axis of the spherical and Cartesian systems. This formulation is

quite similar to our own, with a few exceptions. Whereas we track the point P, which we wish to drive to a final orientation, they track the contact point between the sphere and ground. They also measure the inclination of the point from the x-y plane, where we measure the inclination from the z-axis. The unit sphere formulation of the kinematics model is (Li and Canny 1990):

$$\begin{bmatrix} \dot{u}_1 \\ \dot{v}_1 \\ \dot{u}_2 \\ \dot{v}_2 \\ \dot{\psi} \end{bmatrix} = \begin{bmatrix} 0 \\ \sec u_1 \\ -\sin \psi \\ -\cos \psi \\ -\tan u_1 \end{bmatrix} \omega_x + \begin{bmatrix} -1 \\ 0 \\ -\cos \psi \\ \sin \psi \\ 0 \end{bmatrix} \omega_y \quad (4.27)$$

where, similar to above, the inputs ω_x and ω_y are oriented to the moving frame of the sphere. Similar controllability of this realization is demonstrated by its Lie distribution,

$$\nabla_{Li,Canny} = \begin{bmatrix} 0 & -1 & 0 & 0 & 0 \\ \sec u_1 & 0 & \sec u_1 \tan u_1 & 0 & -\sec u_1 (1 + 2 \tan^2 u_1) \\ -\sin \psi & -\cos \psi & -\sin \psi \tan u_1 & -\cos \psi & 2 \sin \psi (1 + \tan^2 u_1) \\ -\cos \psi & \sin \psi & -\cos \psi \tan u_1 & \sin \psi & 2 \cos \psi (1 + \tan^2 u_1) \\ -\tan u_1 & 0 & -(1 + \tan^2 u_1) & 0 & 2 \tan u_1 (1 + \tan^2 u_1) \end{bmatrix}$$

which has full rank over $M = \{u_1, v_1, u_2, v_2, \psi\} \in \mathcal{R}^5 \mid -\pi/2 < u_1 < \pi/2, -\pi < u_2 < \pi\}$

as demonstrated by the determinant,

$$\det \nabla_{Li,Canny} = \sec u_1 \quad (4.28)$$

and hence controllability is proven over M . Since M does not cover the complete surface of the sphere, Li and Canny define a second model, which is supposedly controllable at the remaining points not contained in M , but this fact has not been able to be confirmed.

The kinematics formulation of (Bicchi, Prattichizzo, et al. 1995) is fundamentally similar to the (Li and Canny 1990) model, with the exception that the inputs ω_x and ω_y are relative to the fixed x-y axis, respectively. Such a formulation is,

$$\begin{bmatrix} \dot{x} \\ \dot{y} \\ \dot{u} \\ \dot{v} \\ \dot{\psi} \end{bmatrix} = \begin{bmatrix} 0 \\ -1 \\ \sin \psi / \cos v \\ \cos \psi \\ \tan v \sin \psi \end{bmatrix} \omega_x + \begin{bmatrix} 1 \\ 0 \\ \cos \psi / \cos v \\ -\sin \psi \\ \tan v \cos \psi \end{bmatrix} \omega_y \quad (4.29)$$

where $\{x, y\}$ is the location of the sphere on the plane, $\{u, v\}$ is the location the point on the surface of the sphere, and ψ is the contact angle. This model is then reformulated by transforming the inputs according to,

$$\omega = \begin{bmatrix} \cos v \sin \psi & \cos \psi \\ \cos v \cos \psi & -\sin \psi \end{bmatrix} \hat{\omega} \quad (4.30)$$

to generate the system model,

$$\begin{bmatrix} \dot{u} \\ \dot{v} \\ \dot{\psi} \\ \dot{x} \\ \dot{y} \end{bmatrix} = \begin{bmatrix} 1 \\ 0 \\ \sin v \\ \cos \psi \cos v \\ -\sin \psi \cos v \end{bmatrix} \hat{\omega}_1 + \begin{bmatrix} 0 \\ 1 \\ 0 \\ -\sin \psi \\ -\cos \psi \end{bmatrix} \hat{\omega}_2 \quad (4.31)$$

which, similar to models (2), (4), and (5), permits direct control over the sphere orientation variables. More importantly, Bicchi (Bicchi, Prattichizzo, et al. 1995) uses this formulation to solve the state equations analytically given a series of piecewise independently applied constant controls, $\hat{\omega}_1$ and $\hat{\omega}_2$, which are then solved for numerically to drive the system to a desired trajectory. These equations are very computationally intensive to solve and not well suited to real time control.

4.5 Traditional Nonholonomic Control Techniques

To date, the best understood class of nonholonomic systems is the canonical chained form. First and second order examples of such systems are, respectively:

$$\begin{array}{lll} \dot{x}_1 = u_1 & & \dot{x}_1 = u_1 \\ \dot{x}_2 = u_2 & \text{and} & \dot{x}_2 = u_2 \\ \dot{x}_3 = x_2 u_1 & & \dot{x}_{21} = x_2 u_1 \\ & & \dot{x}_{211} = x_{21} u_1 \\ & & \dot{x}_{212} = x_{21} u_2 \end{array}$$

where u_1 and u_2 are control inputs. Extensive research in the literature has been dedicated to controlling systems in this form, and to converting systems to this form for that very purpose. The method of steering such systems by sinusoidal inputs was studied initially by Brockett (Brockett 1981) and in more detail by Murray and Sastry (Murray and Sastry 1993). Steering these systems using piecewise constant inputs was investigated by Bicchi (Bicchi, Prattichizzo, et al. 1995), Jacob (Jacob 1992), and Lafferriere (Lafferriere and Sussmann 1991). Exponential feedback stabilization has been accomplished by Sordalen (Samson 1995) using a non-smooth time varying feedback law, by Morin (Morin and Samson 1997) using backstepping techniques, and by Tayebi (Tayebi, Tadjine, et al. 1997) via an invariant manifold approach, to only name a few.

Feedback techniques for converting noncanonical systems to chained form have been presented by Murray (Murray and Sastry 1993) and Sordalen (Sordalen 1993). Both use a constructive proof based on the differential properties of a canonical system to determine a feedback transformation to convert the system to chained form. Thus, the techniques prescribe a set of sufficiency conditions that such a function should satisfy as

guidelines for selecting a transformation. Hence, the process requires intuition and trial and error, on the behalf of the user.

Fortunately, a test is known for determining if a transformation to chained canonical form exists (Murray, Zexiang, et al. 1994). This test is based upon the controllability filtration of the system, Γ_i ,

$$\begin{aligned}\Gamma_0 &= \text{span}(X_1, X_2) \\ \Gamma_1 &= \Gamma_0 + [\Gamma_0, \Gamma_0] \\ \Gamma_2 &= \Gamma_1 + [\Gamma_1, \Gamma_0] \\ &\vdots \\ \Gamma_k &= \Gamma_{k-1} + [\Gamma_{k-1}, \Gamma_0]\end{aligned}\tag{4.32}$$

The growth vector, γ , formed by the controllability filtration is,

$$\gamma = [\dim \Gamma_1, \dim \Gamma_2, \dots, \dim \Gamma_k]\tag{4.33}$$

Which is then used to define the relative growth vector, σ . For five-state two-input systems, the relative growth vector must be of the form,

$$\sigma = (2,1,1,1)$$

for a transformation to chained form to exist (Murray, Zexiang, et al. 1994). For the sphere, the corresponding growth vector is,

$$\gamma = [2, 3, 5, 5]\tag{4.34}$$

which corresponds to a relative growth vector,

$$\sigma = (2,1,2,0)$$

Clearly, the system cannot be converted to chained form and the aforementioned techniques are not applicable.

4.6 Simple Geometric Motion Planning

In this section we define geometric algorithms that exploit independent actuation of ω'_x and ω'_y for establishing a path between initial and final configurations. These control actions are defined as,

- a) $\omega'_x = 0$ and $\omega'_y \neq 0$
- b) $\omega'_x \neq 0$, $\omega'_y = 0$, and $\theta \neq 0, \pm\pi$.

Control action (a) results in linear motion along the x' axis and varies θ . Define point F , as shown in Figure 40, as the point along the x' axis where the sphere stops when $\theta \rightarrow 0$. Note that control action (b) causes the sphere to travel along a curve orthogonal to the x' axis with radius ρ as determined by Equation (4.14), repeated here for convenience,

$$\rho = \tan \theta$$

As $\theta \rightarrow 0$, note that the radius of curvature approaches zero, but that as $\theta \rightarrow \pm\pi/2$, the curvature becomes infinite, which corresponds to linear motion. Control action (a) is used to modulate the radius of the path, since $\dot{\theta} = \omega'_y$. This moves point C along the x' axis. When control action (b) is applied, the sphere then travels along the curved path, as indicated in Figure 40. Note that during action (b) the variation of α and ϕ are dependent on θ (see Equation (4.11)), but that θ is constant. Since θ is unchanged the distance CF remains constant, and F travels in a circular path concentric with the paths of the points Q and P .

4.6.1 Partial Reconfiguration Algorithm

These properties will now be exploited to design an algorithm for moving the sphere to a specified point with a desired orientation. For simplicity, let that point be the origin of the coordinate system and let the orientation be such that $\theta = 0$. Reconfiguration with the final values of α and ϕ also considered will be discussed in the next section. Alternate final positions, and values of θ , can be accomplished by coordinate transformations.

The steps of the algorithm are now defined with reference to Figure 40. Assume the sphere is in the initial position $\{x_0 \ y_0 \ \alpha_0 \ \theta_0\}$ with fixed point F and pivot point C as indicated in Figure 40. The partial reconfiguration the steps are as follows:

1. Define the unique circle passing through the points O and F, and with its center on the line CF at point C'. Assuming that the sphere is initially at point Q with $\theta = \theta_0$. Apply control action (a) to drive $\theta \rightarrow \theta'$ and $C \rightarrow C'$.

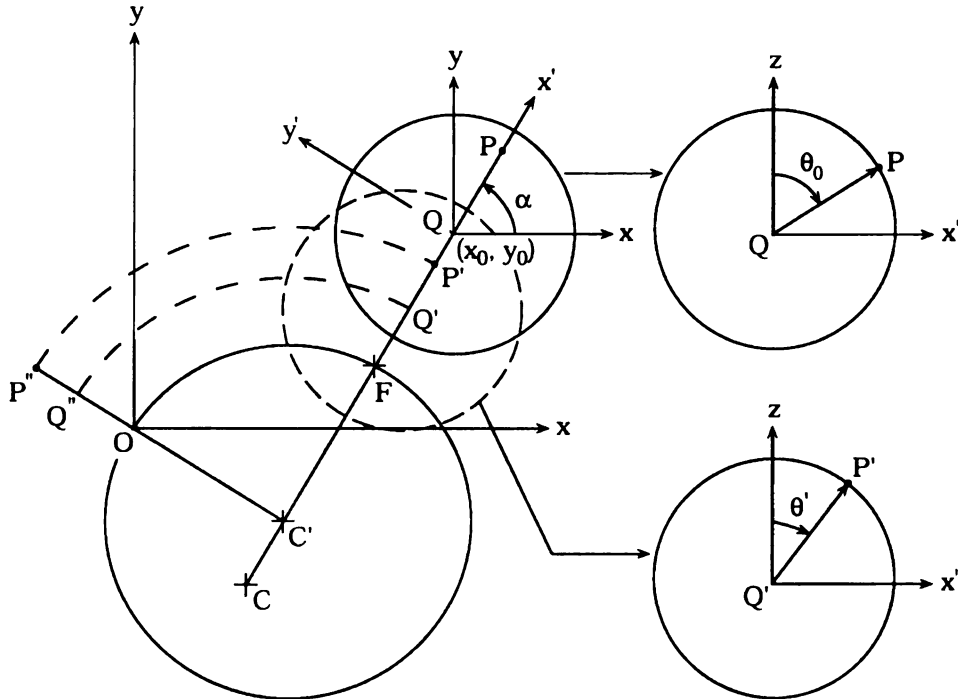


Figure 40. Partial Reconfiguration of the sphere.

2. Apply control action (b) such that the sphere travels along the circle and $F \rightarrow O$, $Q' \rightarrow Q''$, and $P' \rightarrow P''$.
3. Apply control action (a) such that $\theta \rightarrow 0$, $Q'' \rightarrow O$, and P'' returns to its topmost position. This completes the reconfiguration maneuver.

Several calculations must be completed prior to executing this procedure. The equation of the circle passing through points $O \equiv (0,0)$ and

$$F \equiv (x_F, y_F) = (x_0 - \theta \cos \alpha, y_0 - \theta \sin \alpha)$$

must be determined. The center of the circle, $C' \equiv (a, b)$, lies along the line with slope α passing through point (x_0, y_0) , which is defined by,

$$b = a \tan \alpha_0 + (y_F - x_F \tan \alpha_0) = (a - x_F) \tan \alpha_0 + y_F \quad (4.35)$$

Equating the distances OC' and $C'F$, we have

$$a^2 + b^2 = (a - x_F)^2 + (b - y_F)^2 \quad (4.36)$$

Equations (4.35) and (4.36) are then solved for a ,

$$a = \frac{x_F^2 - y_F^2 + 2x_F y_F \tan \alpha_0}{2(x_F + y_F \tan \alpha_0)} \quad (4.38)$$

and then Equation (4.35) is used to solve for b . The angle θ' , $0 < \theta' \leq \pi/2$, is then determined from,

$$\tan \theta' - \theta' = \sqrt{a^2 + b^2} \quad (4.39)$$

The angle of segment CO , corresponding to the final angle α_f of the x' axis, is,

$$\alpha_f = \arctan\left(\frac{-b}{-a}\right)$$

4.6.2 Simulation of Partial Reconfiguration Algorithm

Simulation of the partial reconfiguration process will now be demonstrated. Let the sphere the sphere begin at the initial condition:

$$\{x \ y \ \alpha \ \theta \ \phi_G\}^T = \{4.33 \ 2.50 \ \pi/3 \ \pi/6 \ 0\}^T$$

The final conditions are required to be,

$$\{x \ y \ \theta\} = \{0 \ 0 \ 0\}$$

where α and ϕ are allowed to vary freely. Figure 41 shows the reconfiguration process viewed from directly above and Figure 42 shows the variables as functions of time.

The sphere starts at point Q with the camera opening at point P and the point q on the equatorial circle orthogonal to QP. The fixed point, F, is determined to be $F = (x_F, y_F) = (4.07, 2.05)$. Point C, the center of the concentric paths traveled by points Q and P, is calculated via sequential application of Equations (4.38) and then

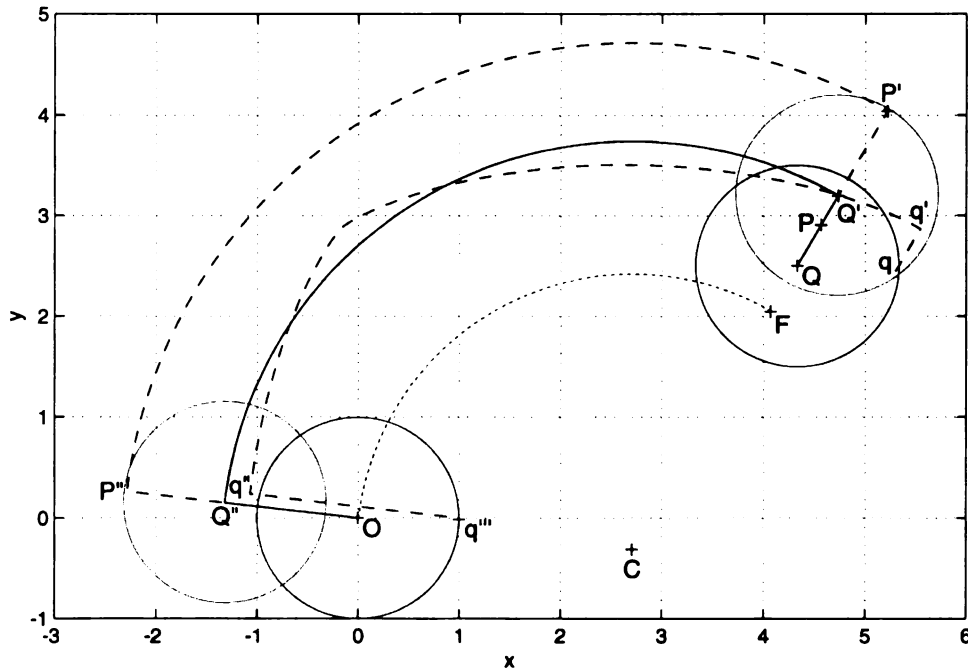


Figure 41. Partial reconfiguration simulation: top view.

(4.35) to be $C = (a, b) = (2.71, -31)$. Angle θ' , which defines the radius of the concentric paths about point C, is calculated via Equation (4.39) to be $\theta' = 1.33 = 76.1^\circ$.

During Step 1 of the partial reorientation process, the sphere rolls in the α_0 direction, via control action (a), until $\theta' = 1.33$ as indicated in Figure 42. Control action (b) is then applied during Step 2 point F reaches point O (Figure 41), which occurs when $\alpha = \alpha_f = 3.03 = 173^\circ$ (Figure 42). At this location, the center of the sphere is 1.33units away from the final point O. Application of control action (a), Step 3, completes the process by driving $\theta \rightarrow 0$, $Q \rightarrow O$, and $q'' \rightarrow q'''$. Notice that coincidentally the reorientation of point q is $\Delta\phi_G = -2\pi$, which means that point q maintains the same orientation in the x-y plane.

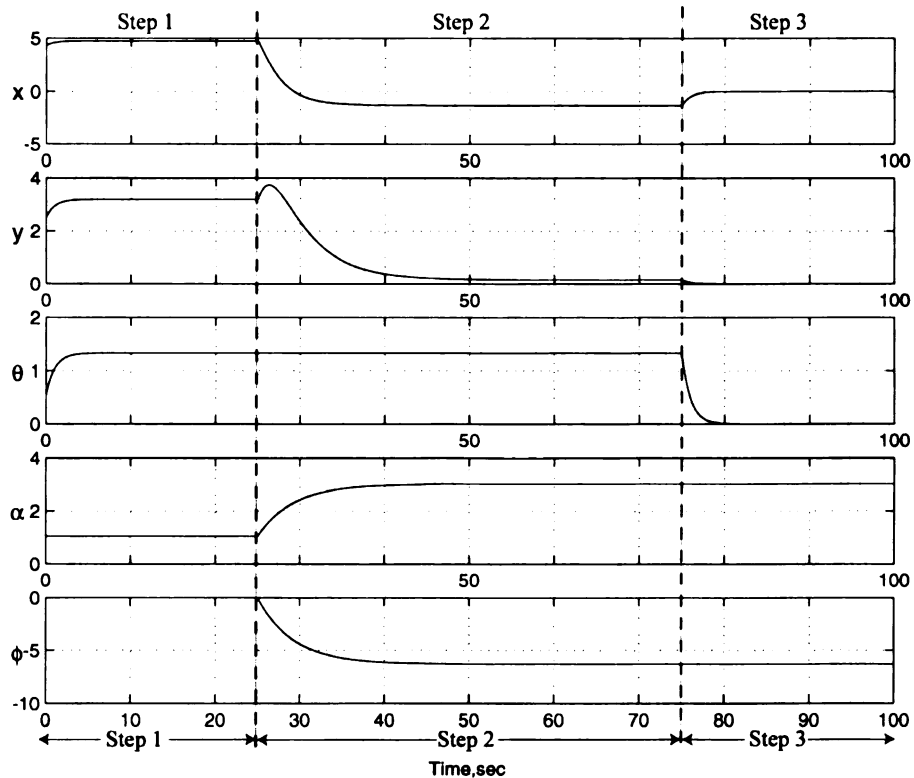


Figure 42. Partial reconfiguration simulation: chart view.

4.6.3 Complete Reconfiguration Algorithm

The previous algorithm can be modified to also move the angle ϕ , defined in Figure 39, to a specified final value as well as x , y , and θ . This modified algorithm will drive $\theta \rightarrow 0$ when the sphere reaches its final position and the point P to its topmost position on the sphere. At this location, P is directly above the center of the sphere and α becomes undefined. Hence, α is not mentioned as a specified output of this algorithm. The variable ϕ , however, defines the location of a point q on the equatorial circle of the sphere perpendicular to line QP. Thus, specification of ϕ is actually required to complete the description of the sphere's final orientation. The variable α does play a role in defining the algorithm for complete reconfiguration since α and ϕ are coupled by Control Action (b), as indicated by Equation (4.15), shown below for convenience.

$$\dot{\phi} = -\dot{\alpha} \sec \theta \quad (4.15)$$

Recall that control action (b) does not affect θ , but actually causes the sphere to travel on the x - y plane along a curved path with radius $\rho = \tan \theta$. While traveling this path, control action (b) integrates the value of α if $\theta \neq \pm\pi/2$ and results in a net change of α denoted as $\Delta\alpha$. Equation (4.15) can then be reduced to,

$$\Delta\phi = -\Delta\alpha \sec \theta' \quad (4.40)$$

where θ' is the value θ of while control action (b) is applied. This relationship indicates that a desired $\Delta\phi$ can be accomplished by an appropriate selection of θ' and $\Delta\alpha$. First recall, however, that ϕ is defined relative to the x' axis, as indicated in Figure 39, which rotates by $\Delta\alpha$ during this algorithm. If we define $\Delta\phi_G$ as the change in ϕ relative to the globally fixed x - y coordinate frame resulting from the orientation process, we then have:

$$\Delta\phi_G = \Delta\alpha(1 - \sec \theta') \quad (4.41)$$

The complete reconfiguration algorithm will now be defined so as to provide a basis for discussing Equations (4.40) and (4.41) further. Referring to Figure 43 and Figure 44, let the initial and final values of the states $(x, y, \theta, \alpha, \phi)$ be $(x_0, y_0, \theta_0, \alpha_0, \phi_0)$ and $(0, 0, 0, 0, \phi_f)$, respectively.

1. The sphere starts at the initial position (x_0, y_0) with point P oriented by θ_0 and α_0 , which also defines the x' axis. Apply control action (a) to make $\theta \rightarrow 0$, which takes P to its topmost position and the center of the sphere from $(x_0, y_0) \rightarrow F \equiv (x_F, y_F) = (x_0 - \theta_0 \cos \alpha_0, y_0 - \theta_0 \sin \alpha_0)$.
2. Since α is undefined when $\theta = 0$, α can be specified such that sphere will roll in a new direction α' when control action (a) is applied. Apply control action (a) such that $\theta \rightarrow \theta'$ and $Q \rightarrow Q'$, $P \rightarrow P'$ and $C \rightarrow C'$. Note that this step defines a unique circle passing through points O and F with its center at C' . Variables α' and θ' , which determine the location of C' , and hence the circle, are calculated in part by either Equations (4.40) or (4.41), such that $\Delta\alpha = \alpha' - \alpha_f$ and $\Delta\phi = \phi_0 - \phi_f$ will be satisfied.

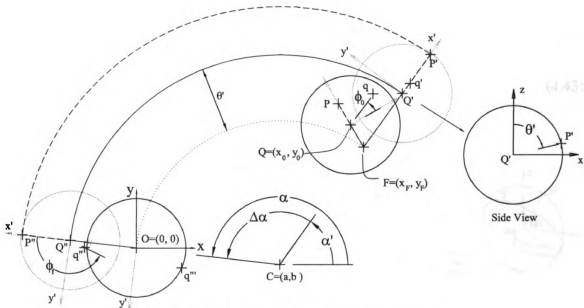


Figure 43. Complete reconfiguration process, top view.

3. Apply control action (b) to drive $F \rightarrow O$ along the circular segment designed in the previous step. Note that Q' and P' travel along concentric segments such that $Q' \rightarrow Q''$, $P' \rightarrow P''$, $\alpha' \rightarrow \alpha_f$, and $\phi_0 \rightarrow \phi_f$. Note that ϕ and α have converged to their final values!
4. Now apply control action (a) to drive $\theta \rightarrow 0$ which brings $Q'' \rightarrow 0$ and hence $(x, y) \rightarrow (0,0)$. Note that control action (a) neither affects α or ϕ , and complete reconfiguration is complete.

The reconfiguration algorithm hinges on the calculation of the circle created during step 2. Since points F and O are pre-determined, the circle is dependent on the coordinates of $C' \equiv (a, b)$, which are calculated based on the choice of $\Delta\alpha = \alpha_f - \alpha'$ and θ' which create a desired $\Delta\phi$. The angle $\Delta\alpha$ is traversed by the robot during step 3 when $F \rightarrow O$. By inspection of Figure 43 and the application of trigonometry, the locations of points O, C' , and F reveal,

$$\Delta\alpha \equiv \alpha_f - \alpha' = 2 \arcsin \left(\frac{1}{2} \sqrt{\frac{x_F^2 + y_F^2}{a^2 + b^2}} \right) \quad (4.42)$$

This equation can be expressed as a function of θ' . To do this, recall that the radius of the circular path through O and F is expressed as $\rho = \tan \theta'$. Inspection of Figure 43 then yields the following expression since the sphere has unit radius:

$$\rho = C'Q' = \tan \theta' = \sqrt{a^2 + b^2} + \theta' \quad (4.43)$$

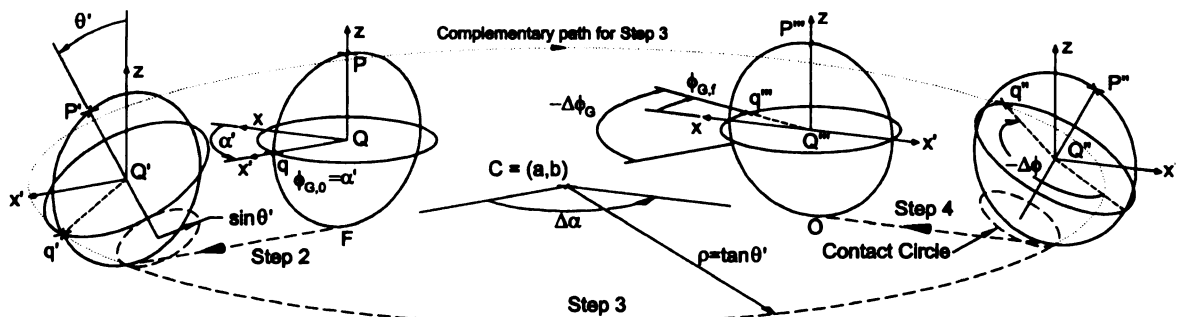


Figure 44. Complete reconfiguration process, perspective view.

Terms in θ' are then moved to the right hand side to provide,

$$\tan \theta' - \theta' = \sqrt{a^2 + b^2} \quad (4.44)$$

Substituting this expression into the denominator of Equation (4.42) reveals,

$$\Delta\alpha = 2 \arcsin \left(\frac{\sqrt{x_F^2 + y_F^2}}{2(\tan \theta' - \theta')} \right) \quad (4.45)$$

which can then be substituted into Equation (4.41) to solve numerically for θ' given a desired $\Delta\phi_G$:

$$\Delta\phi_G = -2 \arcsin \left(\frac{\sqrt{x_F^2 + y_F^2}}{2(\tan \theta' - \theta')} \right) (1 - \sec \theta') \quad (4.46)$$

The calculated θ' is then substituted back into (4.41) to determine $\Delta\alpha$. Based on the angle of line OF, we can then determine α_f and α' according to the following relationships that can be confirmed by inspection of the geometric properties of Figure 43,

$$\alpha' = \arctan \left(\frac{y_F}{x_F} \right) + \frac{\pi}{2} - \frac{\Delta\alpha}{2} \quad (4.47)$$

$$\alpha_f = \arctan \left(\frac{y_F}{x_F} \right) + \frac{\pi}{2} + \frac{\Delta\alpha}{2} \quad (4.48)$$

While not necessary for the algorithm, the location of $C' \equiv (a, b)$ can be determined by considering the line passing through O with slope α_f ,

$$b = a \tan \alpha_f \quad (4.49)$$

The center of the circular path lies on the segments OC' and FC', and their lengths can be equated to show,

$$a^2 + b^2 = (x_F - a)^2 + (y_F - b)^2 \quad (4.50)$$

which is then used in conjunction with Equation (4.49) to solve for a and b ,

$$a = \frac{x_F^2 + y_F^2}{2(x_F + y_F \tan \alpha_f)} \quad (4.51)$$

$$b = \frac{x_F^2 + y_F^2}{2(x_F + y_F \tan \alpha_f)} \tan \alpha_f \quad (4.52)$$

4.6.4 Simulation of Complete Reconfiguration Algorithm

Simulation of the full reconfiguration algorithm will now be demonstrated. For comparison purposes, let the initial conditions be identical to those used in the simulation of the partial reconfiguration algorithm. That is, let the initial conditions be:

$$\{x \ y \ \alpha \ \theta \ \phi_G\}^T = \{4.33 \ 2.50 \ \pi/3 \ \pi/6 \ 0\}^T$$

The final conditions will also be similar, with the exception that ϕ_G is also specified:

$$\{x \ y \ \theta \ \phi_G\}^T = \{0 \ 0 \ 0 \ -1.5\pi\}^T$$

As in the previous example, point Q represents the initial position of the sphere, and points P and q are used to orient the sphere's surface, as shown in Figure 45. During Step 1, control action (a) is applied and the sphere rolls such that $Q \rightarrow F$ and $P \rightarrow F$, which corresponds to $\theta \rightarrow 0$ as shown in Figure 46. Since P is directly above the center of the sphere, the angle α is poorly defined. A new angle $\alpha' = 1.90 = 109^\circ$ is then determined by Equation (4.47) such that a net $\Delta\alpha = 0.266 = 15.3^\circ$ is achieved during Step 2, as illustrated by Figure 45 and Figure 46. The desired $\Delta\alpha$ is calculated by Equation (4.45), which is based on a desired $\theta' = 1.52 = 86.9^\circ$ as calculated by Equation (4.46) to

achieve the initially specified $\Delta\phi_G = -3\pi/2 = -270^\circ$. Recall that $\Delta\phi_G$ measures the net rotation of the point q in the equatorial plane \perp to line QP when QP is aligned with the z -axis. Hence, specification of $\Delta\phi_G$ is equivalent to specifying the position of point q on the equator of the sphere.

As Figure 45 and Figure 46 indicate, step 2 results in $\alpha_f = 2.17 = 124^\circ$, via Equation (4.48), and $Q' \rightarrow Q''$, $P' \rightarrow P''$, and $q' \rightarrow q''$. Angle α_f is also used to calculate the center of the concentric paths, $C = (9.68, -14.17)$ via Equations (2.9) and (2.8). Step 3 rolls the sphere such that $Q'' \rightarrow O$, $P'' \rightarrow O$, $q'' \rightarrow q'''$, and thus $(x, y, \theta) \rightarrow (0, 0, 0)$. Note that point q has rotated a net of $\Delta\phi_G = -3\pi/2 = -270^\circ$ between point F with q_F and point O with q''' . Hence, complete reconfiguration has been completed, and by only using a few simple initial calculations.

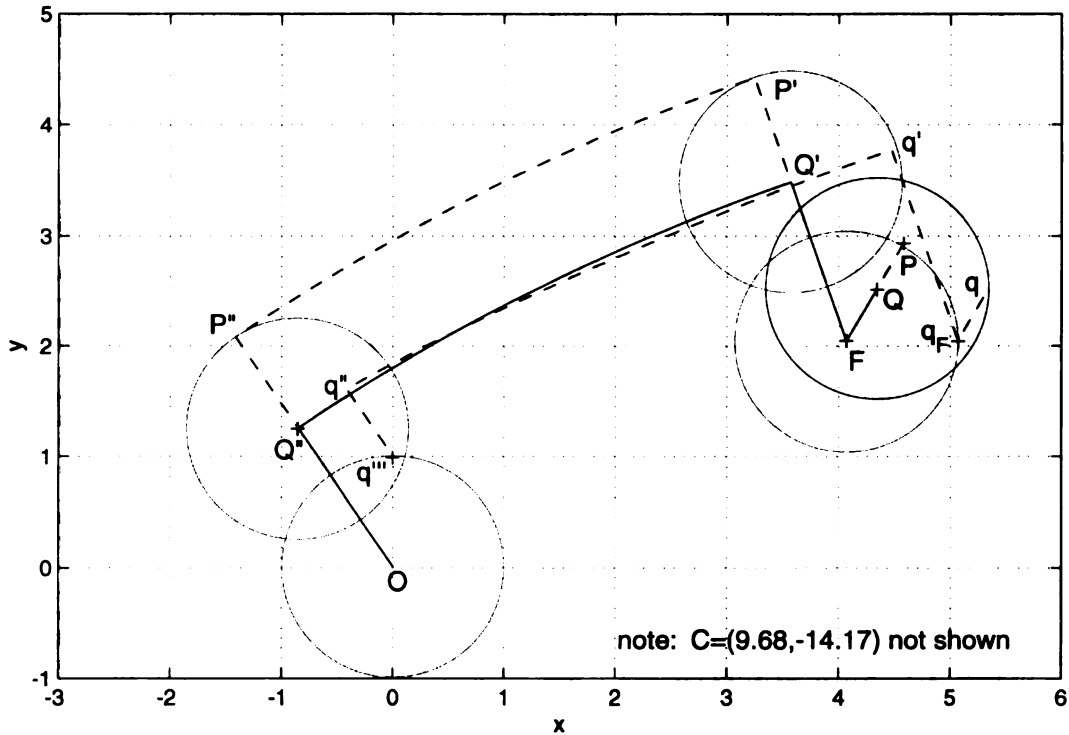


Figure 45. Complete reconfiguration simulation: top view.

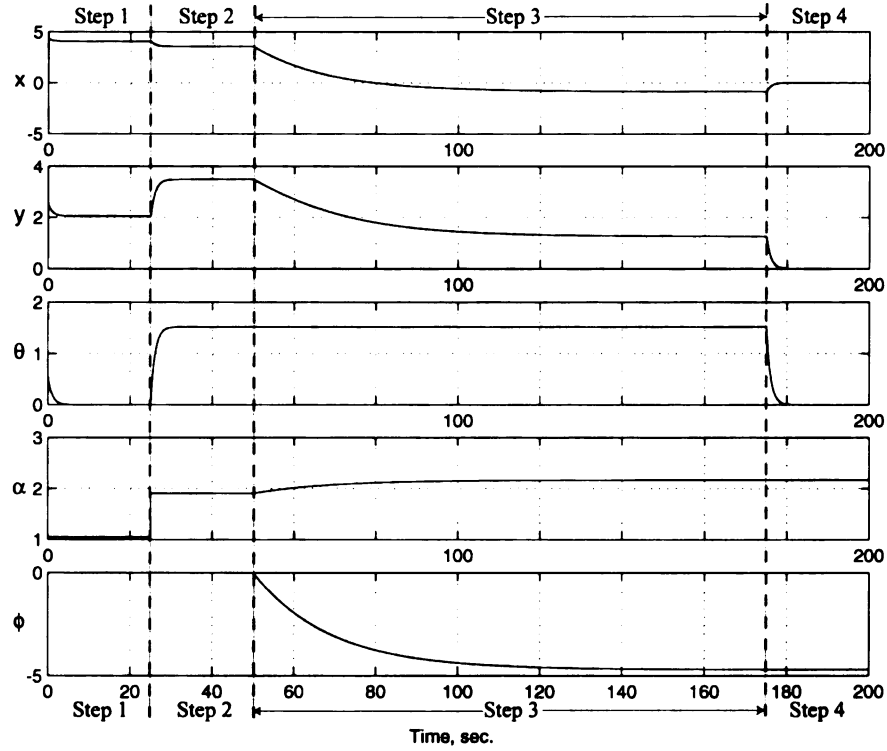


Figure 46. Complete reconfiguration simulation: chart view.

4.6.5 Reachability of All orientations

In Section 4.3, Chow's theorem was applied to the system model to prove that a path exists between any initial and final configurations of the sphere. The question that remains is whether the complete reconfiguration algorithm presented in 4.6.3 is capable of this. Based on the partial reconfiguration algorithm, it is obvious that the sphere can be brought to the point O with the point P at the topmost position. In that example, the result was $(x, y, \theta) \rightarrow (0, 0, 0)$. Full reconfiguration is accomplished when the point q also moves to a specified final location on the equator of the sphere. The ability to place point q is determined by the achievable $\Delta\phi_G$ calculated by Equation (4.41) from Section 4.6.3 for the sphere traveling in a Counter-Clock-Wise (CW) path along the arc:

$$\Delta\phi_G = \Delta\alpha(1 - \sec \theta') \quad (4.41)$$

This equation indicates that the achievable $\Delta\phi_G$ are dependent upon $\Delta\alpha$ and θ' . As indicated in Figure 47, the range of $\Delta\alpha$ that can be attained is dependent on whether the

center of the path is above or below OF. If the center of the path is below the line, as indicated by point C_2 , the range of $\Delta\alpha$ is $0^\circ \leq \Delta\alpha \leq 180^\circ$. The lower limit of $\Delta\alpha = 0^\circ$ occurs when the radius of the path is infinite and $\theta' = 90^\circ$. This corresponds to the minimum $\Delta\phi_G$ achieved, $\Delta\phi_G = -r$, shown in Figure 48, where r is the length of OF determined by,

$$r = \sqrt{x_F^2 + y_F^2} \quad (4.53)$$

The upper limit of $\Delta\alpha = 180^\circ$ occurs when the point is at the midpoint of OF. As the center of the path moves above the line OF, as indicated by Path 3 with center C_3 in

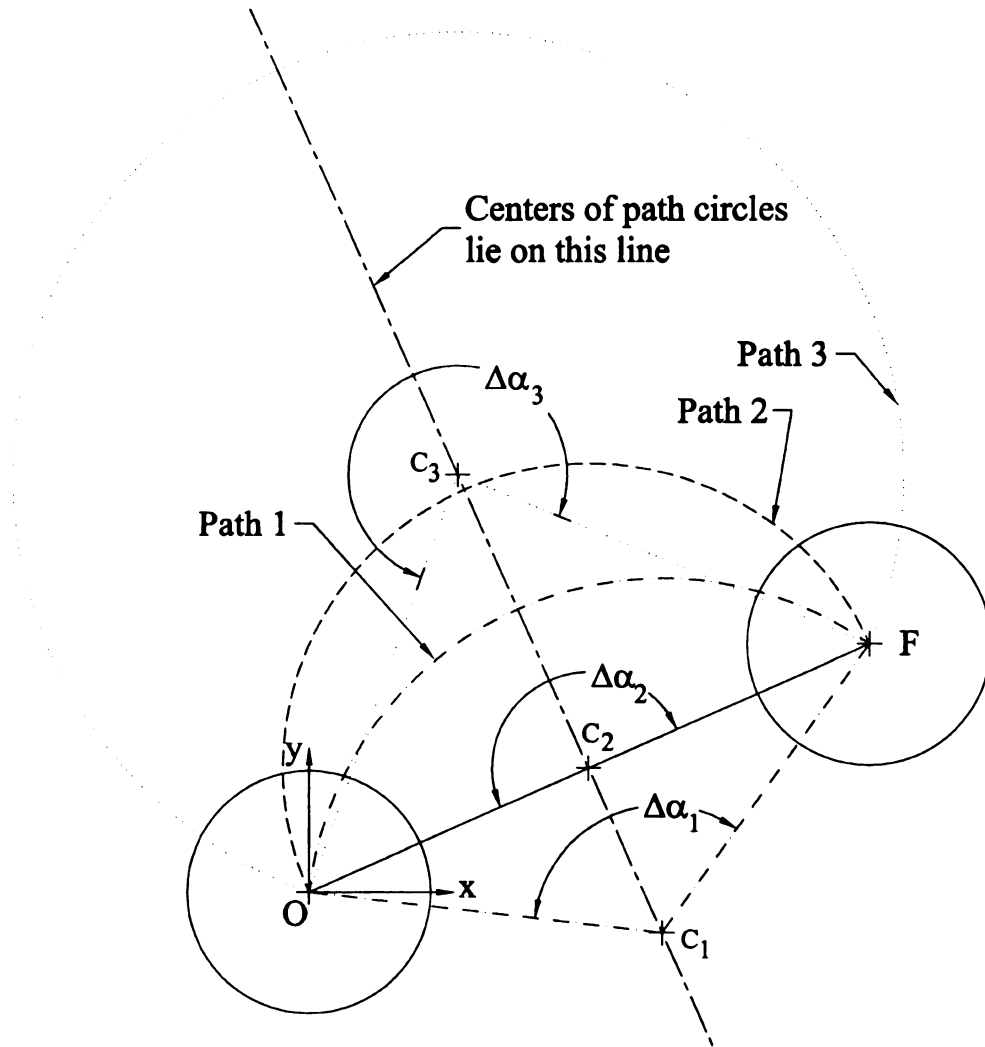


Figure 47. Paths of point F as $\Delta\alpha$ varies. from Error! Objects cannot be created from editing field codes. to Error! Objects cannot be created from editing field codes..

Figure 47, the range of $\Delta\alpha$ increases to include $180^\circ \leq \Delta\alpha \leq 360^\circ$. Again, the lower limit of $\Delta\alpha = 180^\circ$ occurs when the center of the path is at the midpoint of OF. The upper limit of $\Delta\alpha = 360^\circ$ occurs as radius of the path becomes infinite. This case is impractical because the sphere is traveling along a circle with infinite radius away from the point O. Theoretically, it would need to travel an infinite distance to the right until it returns back to point O from the left side of Figure 47.

The net reorientation $\Delta\phi_G$ of the sphere that occurs as a result of $0^\circ \leq \Delta\alpha \leq 360^\circ$ can be determined numerically by Equation (4.46), calculated previously:

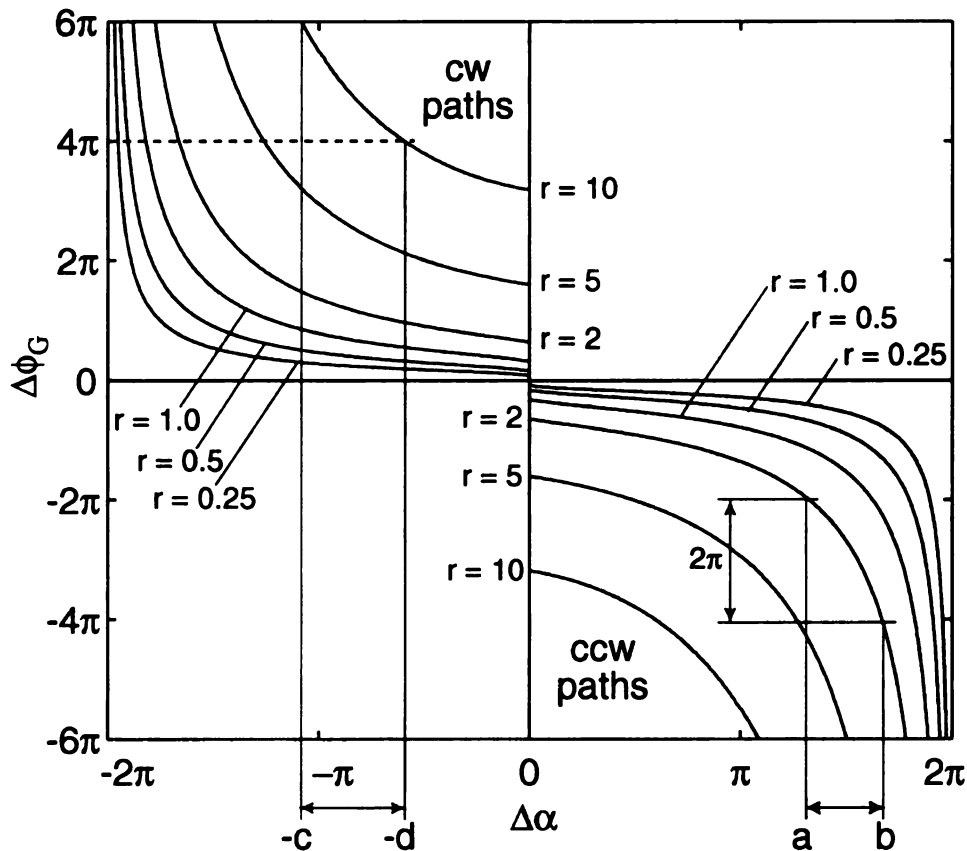


Figure 48. Net sphere re-orientation $\Delta\phi_G$ as a function of $\Delta\alpha$ for $r = 0.25, 0.5, 1.0, 2.0, 5.0, 10.0$.

$$\Delta\phi_G = 2 \arcsin \left(\frac{\sqrt{x_F^2 + y_F^2}}{2(\tan \theta' - \theta')} \right) (1 - \sec \theta') \quad (4.46)$$

The results of this equation are shown in Figure 48 for locations of point F with $r = 0.25, 0.5, 1.0, 2.0, 5.0,$ and 10 . As indicated above, the smallest reorientation $\Delta\phi_G$ of the sphere is determined by $\Delta\phi_G = -r$, and as $\Delta\alpha \rightarrow 360^\circ$ then $\Delta\phi_G \rightarrow -\infty$. The converse of these ranges holds true when the sphere travels in the opposite Clock-Wise direction along the circular paths. An example of this path is indicated in Figure 50, and the reorientation $\Delta\phi_G$ in this case is determined by

$$\Delta\phi_G = \left(-2\pi + 2 \arcsin \left(\frac{\sqrt{x_F^2 + y_F^2}}{2(\tan \theta' - \theta')} \right) \right) (1 - \sec \theta') \quad (4.54)$$

The reorientation $\Delta\phi_G$ results as determined by Equation (2.1) for the sphere traveling

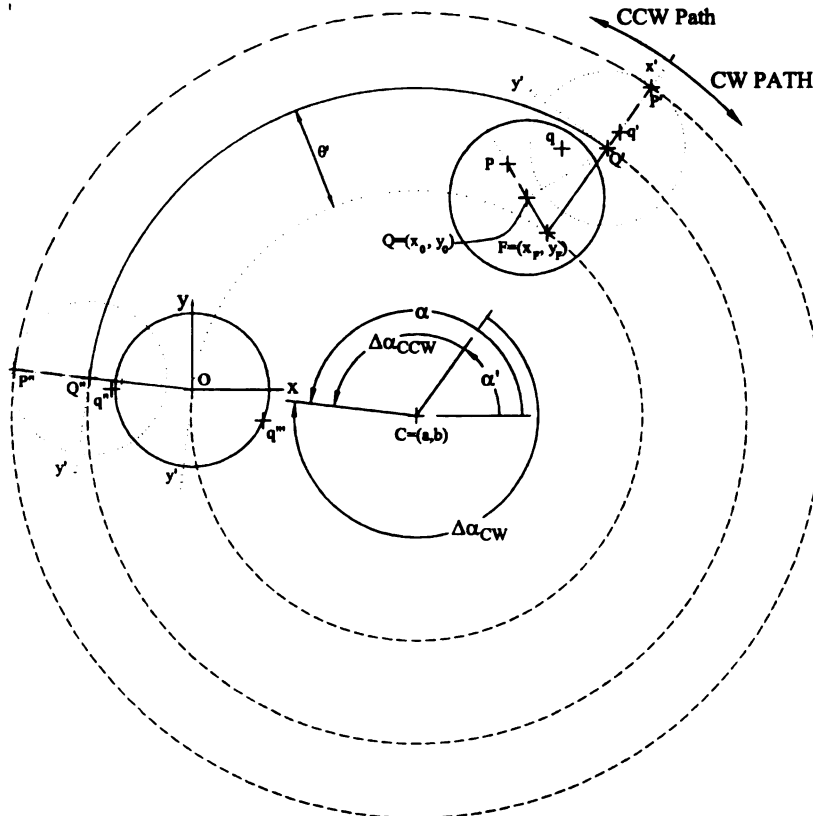


Figure 50. Counter Clock-Wise (CCW) and alternate Clock-Wise (CW) and paths for complete reconfiguration.

along the CW paths are also shown in Figure 48 for $-360^\circ \leq \Delta\alpha \leq 0^\circ$.

It is indicated by Figure 48 that complete reorientation of $\Delta\phi_G$ can be achieved by selecting different values of $\Delta\alpha$, regardless of the distance of the sphere, r , from its final destination. For example, Figure 48 illustrates that for $r = 2$, a range $-4\pi \leq \Delta\phi_G \leq -2\pi$ can be achieved by selecting $a \leq \Delta\alpha \leq b$. Thus, the actual range of $\Delta\phi_G$ is offset by 4π such that the net reorientation is $0 \leq \Delta\phi_G \leq 2\pi$. Similar conclusions can be made for the sphere traveling in the CW paths.

4.7 Other Comments

In this chapter, the spherical mobile robot, Spherobot was considered. Spherobot encounters computational constraints that are caused by its nonlinear nonholonomic rolling constraints. These constraints are such that traditional control techniques do not apply, and techniques proposed in the literature are not adequate for efficient control. To resolve this problem, a unique moving coordinate system is defined on the sphere. This causes the robot to follow linear and curvilinear paths on the plane while each control input is driven independently. The properties of these paths are then examined more closely and used to derive intuitive geometric motion planning strategies for moving the sphere to a prescribed location and orientation on the plane. The benefit of these strategies is their simplicity and limited calculations required, which suits them especially to real-time implementation.

CONCLUDING REMARKS

5. Concluding Remarks

Design and control of constrained robotics systems for enhanced dexterity and mobility has been examined via three case studies. In the first, the design of surgical mechanism for improved dexterity and reachability in MIS was examined. This system is constrained in size and in allowable motion by a port on the patient abdomen. The design achieves a delicate balance between load capacity, dexterous workspace, and DOF using an optimized geared linkage with tendon actuation. The resulting mechanism, which can be coupled to form a robotic or manual instrument, provides forceps at the tip of a linkage capable of bidirectional 180° articulation. The forceps are provided with unlimited rotation, actuation, and the capability to support a 4.5N load at the tip of a 1cm suture needle.

The second system considered is a miniature climbing robot for urban reconnaissance. Space constraints are also important for this system, as it must maneuver ventilation ducts and the exterior of buildings while minimizing detection. The resulting robot, which is the smallest of its kind, also satisfies mobility requirements and weight limitations using an innovative under actuated revolute hip biped structure. The system is capable of walking, climbing surfaces with any angle, traversing between surfaces with various inclinations, and moving between specified locations.

In the third case study, a spherical mobile robot for reconnaissance is examined. The robot provides excellent mobility, since it can roll in any direction, but control of the robot is complicated by its nonlinear nonholonomic motion constraints. The sphere reorientation problem represents a fundamental motion control dilemma that is not solved

via traditional approaches, which are more complicated and computationally intense. We achieve efficient point-to-point motion planning with a desired reorientation using an intuitive geometric motion planner. The motion planner is based upon a unique coordinate system defined on the sphere such that independent actuation of the control inputs causes the sphere to travel along intuitive linear and curved paths. Straightforward and efficient geometric planning techniques are then used to achieve point-to-point motion and desired reorientation of the sphere. Thus, superior mobility of the sphere can be achieved with very minimal computation.

In each of these state-of-the-art systems, innovative design and control strategies are key for providing enhanced dexterity and mobility. Each system has provides unique constraints in space, power, weight, and computational limitations that could not be solved using traditional methods. As robotics applications continue to expand, innovative solutions, such as those presented here, will be crucial to successful system realization.

BIBLIOGRAPHY

Bibliography

API-Portescap, 1998, "Miniature High Performance Motors & Peripheral Components for Motion Solution," API Motion, West Chester, PA.

Arora, J. S., 1989, *Introduction to Optimum Design*. New York: McGraw Hill.

Asimov, I., 1940, "Robbie," in *Super-Science Stories*, vol. 1.

ASM International Handbook Committee, 1996, *Stainless Steels*. Materials Park, OH.

Bach, F.-W., H. Haferkamp, J. Lindemaier and M. Rachkov, 1996, "Underwater Climbing Robot for contact Arc Metal Drilling and Cutting.," presented at 1996 IEEE IECON; 22nd Int. conf. on Industrial Electronics, pp. 1560-1565.

Bahr, B., Y. Li and M. Najafi, 1996, "Design and Suction Cup Analysis of a Wall Climbing Robot," *Computers Elect. Engng*, vol. 22, no. 3, pp. 193-209.

Bicchi, A., A. Balluchi, D. Prattichizzo and A. Gorelli, 1997, "Introducing the Spherical: An Experimental Testbed for Research and Teaching in Nonholonomy," presented at IEEE Int'l Conference on Robotics and Automation, pp. 2620-2625.

Bicchi, A., D. Prattichizzo and S. S. Sastry, 1995, "Planning Motions of Rolling Surfaces," presented at 1995 34th IEEE Conference on Decision and Control, New Orleans, LA, pp. 2812-2817.

Bloch, A. M. and P. E. Crouch, 1995, "Nonholonomic Control Systems on Riemannian Manifolds," *SIAM J. Control and Optimization*, vol. 33, no. 1, pp. 126-148.

Briones, L., P. Bustamante and M. Serna, 1994, "Robicen: A wall climbing pneumatic robot for inspection in nuclear power plants," *Robotics & Computer-Integrated Manufacturing*, vol. 11, no. 4, pp. 287-292.

Brockett, R. and L. Dai, 1993, "Non-holonomic kinematics and the role of elliptic functions in constructive controllability," in *Non-Holonomic Motion Planning*, Z. Li and J. W. Canny, Eds. Kluwer, Boston, pp. 1-22.

Brockett, R. W., 1981, "Control Theory and Singular Riemannian geometry," in *New Directions in Applied Mathematics*. New York: Springer Verlag, pp. 11-27.

Bunt, T. J. and W. M. J. Moore, 1993, "Evaluation of the strength of vascular anastomotic techniques.," *Am Surg*, vol. 59, no. 7, pp. 470-1.

Capek, K., 1923, *R.U.R. (Rossum's Universal Robots): a fantastic melodrama*. Garden City, NY: Doublday, Page.

Chow, W. L., 1939, "Über Systeme von Linearen Partiellen Differentialgleichungen erster Ordnung," *Math. Ann.*, vol. 117, pp. 98-105.

Cohn, M. B., L. S. Crawford, J. M. Wendlandt and S. S. Sastry, 1995, "Surgical application of milli-robotics," *Journal of Robotic Systems*, vol. 12, no. 6, pp. 401-416.

Cortland Cable Company, 1997, "Vectran Technical Specifications, Cortland, NY," .

Craig, J. J., 1989, *Introduction to Robotics*. New York: Addison-Wessley Publishing Company.

Dangi, G., J. Stam and D. Aslam, 2000, "Design, Fabrication, and Testing of a Smart Robotic Foot for Microrobotic Systems," presented at International Symposium on Robotics.

Dow-Corning, 1999, "Dow Corning 321 Dry Film Lubricant Information," Dow Corning, Midland, MI 10-809.pdf, 1999.

Dulimarta, H., M. Minor, G. Dangi, R. L. Tummala, R. Mukherjee and D. Aslam, 2000, "Control of an Underactuated Miniature Wall-Climbing robot with Minimal Sensors," presented at submitted to the IEEE Conference on Decision and Control, Sydney, Australia.

Ethicon Endo Surgeries, 1998, "Technical Brochure," , Corporate Headquarters: 4545 Creek Road, Cincinnati, OH 45242-2839.

Faraz, A. and S. Payandeh, 1997, "Synthesis and Workspace Study of Endoscopic Extenders with Flexible Stem," *ASME Journal of Mechanical Design*, vol. 119, pp. 412-14.

Goertz, R. C. and W. M. Thompson, 1954, "Electronically Controlled Manipulator," *Nucleonics*, vol. 12, no. Nov, pp. 46-47.

Guo, G., X. Qian and W. A. Gruver, 1992, "A single-dof multi-function prosthetic hand mechanism with an automatically variable speed transmission," *22nd ASME Biennial Mechanisms Conference, Robotics, Spatial Mechanisms and Mechanical Systems*, vol. 45, no. , pp. 149-154.

Halme, A., T. Schonberg and Y. Wang, 1996, "Motion Control of a Spherical Mobile Robot," presented at AMC'96-MIE.

Hassler, W. L., T. Murray, C. Armstrong and D. Price, 1994, "Rotational Endoscopic Mechanism with Jointed Drive Mechanism", Ethicon, Inc., July 19, 1994, US, Pat. #5,330,502.

Hermann, R. and A. Krener, 1977, "Nonlinear Controllability and Observability," *IEEE Transactions on Automatic Control*, vol. AC-22, no. 5, pp. 728-740.

Hirose, S., A. Nagakubo and R. Toyama, 1991, "Machine That Can Walk and Climb on Floors, Walls, and Ceilings," presented at Fifth International Conference on Advanced Robotics, pp. 753-758.

Hirose, S. and H. Tsutsumitake, 1992, "Disk Rover: A Wall-Climbing Robot using Permanent Magnet Disks," presented at 1992 IEEE/RSJ International Conference on Intelligent Robots and Systems, Raleigh, NC, pp. 2074-2079.

Huitema, T., 1998, "Articulation transmission mechanism for surgical instruments", Ethicon Endo-Surgery, Inc, Feb. 3, 1998, US, Pat. #5,713,505.

Ikeda, K., T. Nozaki and S. Shimada, 1992, "Development of a Self-contained Wall Climbing Robot," *Journal of Mechanical Engineering Laboratory*, vol. 46, no. 2, pp. 128-137.

Jacob, G., 1992, "Motion Planning by Piecewise Constant or Polynomial Inputs," presented at Proceedings of the IFAC Symposium on Nonlinear Control Systems Design, Bordeaux, Fr, pp. 239-244.

Jaeger, J. C., 1987, "Surgical Instrument with Adjustable Angle of Operation", Sept. 4, 1997, Pat. #4,763,669.

Jurdjevic, V., 1993, "The Geometry of the Plate-Ball Problem," *Archives for Rational Mechanics and Analysis*, vol. 124, pp. 305-328.

Knoepfler, D. J., 1993, "Adjustable Angle Medical Forceps", June 5, 1992, US, Pat. #5,209,747.

Lafferriere, G. and H. Sussmann, 1991, "Motion Planning for Controllable Systems without Drift," presented at 1991 IEEE Int'l Conf. on Robotics and Automation, Sacramento, Ca, pp. 1148-1153.

Lande, M. A. and R. J. P. David, 1981, "Articulation for Manipulator Arm", Association des Ouvriers en Instruments de Precision, Paris, Fr, USA, Pat. #4,300,362.

Li, Z. and J. Canny, 1990, "Motion of Two Rigid Bodies with Rolling Constraints," *IEEE Transactions on Automatic Control*, vol. 6, no. 1, pp. 62-72.

Luk, B., A. Collie and J. Billingsley, 1991, "Robug II: An intelligent wall climbing robot," presented at IEEE Int Conf on Robotics and Automation, Sacramento, Ca, pp. 2342-2347.

Luk, B. L., A. A. Collie, V. Piefort and G. S. Virk, 1996, "Robug III: A Tele-operated Climbing and Walking Robot," presented at UKACC Intl Conference on Control, pp. 347-352.

Maxon-Precision-Motors, 1999, "High Precision Drives and Systems Catalog," Maxon Precision Motors, Inc, Burlingame, CA.

Meritt, H. E., 1971, *Gear Engineering*. London: Pitman Publishing.

Micro-Mo-Electronics, 1997, "Miniature DC Drive Components Catalog," Faulhaber Group, Clearwater, FL.

Milenkovic, V., 1987, "New Nonsingular Robot Wrist Design," *Robots 11. 17th International Symposium on Industrial Robots*, pp. 13.29-13.42.

Minor, M., H. Dulimarta, et al., 2000, "Design and Implementation of an Under Actuated Miniature Climbing Robot," Submitted to IROS 2000.

Minor, M. and R. Mukherjee (1999). "A Mechanism for Dexterous End-Effector Placement During Minimally Invasive Surgery." *ASME Journal of Mechanical Design* vol. 121, no. 4, pp 472-479

Morin, P. and C. Samson, 1997, "Application of Backstepping Techniques to the Time-Varying Exponential Stabilisation of Chained Form Systems," *European Journal of Control*, vol. 3, no. 1, pp. 15-36.

Mueglitz, J., G. Kunad, P. Dautzenberg, B. Neisius and R. Trapp, 1993, "Kinematic problems of manipulators in minimal invasive surgery," *Endosc Surg*, vol. 1, pp. 160-164.

Mukherjee, R. and M. Minor, 1999, "A Simple Motion Planner for a Spherical Mobile Robot," presented at 1999 IEEE/ASME Int'l Conf. on Advanced Intelligent Mechatronics, Atlanta, Ga,

Mukherjee, R., M. Minor and J. Pukrushpan, 1999, "Simple Motion Planning Strategies for Spherobot: A Spherical Mobile Robot," presented at 1999 IEEE Conference on Decision and Control.

Mukherjee, R., M. Minor, G. Song and R. Satava, 1998, "Optimisation of an articulated instrument for enhanced dexterity in minimally invasive therapy," *Min Invas Ther & Allied Technol*, vol. 7, no. 4, pp. 335-342.

Murray, R. M. and S. S. Sastry, 1993, "Nonholonomic Motion Planning: Steering Using Sinusoids," *IEEE Transactions on Automatic Control*, vol. 38, no. 5, pp. 700-713.

Murray, R. M., L. Zexiang and S. S. Sastry, 1994, *A Mathematical Introduction to Robotic Manipulation*. Boca Raton: CRC Press.

Nishi, A., 1992, "A Biped Walking Robot Capable of Moving on a Vertical Wall," *Mechatronics*, vol. 2, no. 6, pp. 543-554.

Nishi, A., 1996, "Development of Wall Climbing Robots," *Computers Elect. Engng*, vol. 22, no. 2, pp. 123-149.

Oberg, E., and F. D. Jones, 1973, *Machinery's Handbook*, 19 ed. New York: Industrial Press, Inc.

Pack, R. T., J. L. Christopher and K. Kawamura, 1997, "A Rubbertuator-Based Structure-Climbing Inspection Robot," presented at IEEE International Conference on Robotics and Automation, Albuquerque, New Mexico, pp. 1869-74.

Pivotal Medical Innovations, 1996, "Technical Brochure," , Whittier, CA.

Plietsch, R., 1997, "Macroscopic and microscopic phenomena in the fatigue behaviour of a superelastic NiTi shape memory alloy under cyclic mechanical loading," Karlsruhe Research Center, Germany, Scientific FZKA-5913, June 1997.

Rosen, D. M., and M. A. Carlton, 1997, "Skin closure at laparoscopy.," *J Am Assoc Gynecol Laparosc (CRW)*, vol. 4, no. 3, pp. 347-51.

Rosheim, M. E., 1987, "Singularity-Free Hollow Spray Painting Wrist," in *Robots 11. 17th International Symposium on Industrial Robots*, pp. 13.7 - 13.28.

Samson, C., 1995, "Control of Chained Systems: Application to Path Following and Time-Varying Point Stabilization of Mobile Robots," *IEEE Trans. on Automatic Control*, vol. 40, no. 1, pp. 64-77.

Schenker, P. S., H. Das and T. R. Ohm, 1995, "A new robot for high dexterity microsurgery," *Computer vision, virtual reality and robotics in medicine. First international conference, CVR MED'95*, pp. 115-122.

Schurr, M. O., A. Melzer, P. Dautzenberg, B. Neisius, R. Trapp and G. Buess, 1993, "Development of steerable instruments for minimal invasive surgery in modular conception," *Acta Chir Belg*, pp. 73-77.

Seki, S., 1988, "Techniques for better suturing.," *Br J Surg*, vol. 75, no. 12, pp. 1181-4.

Shigley, J. E., and C. R. Mischke, 1989, *Mechanical Engineering Design*, 5th ed: McGraw-Hill.

Sordalen, O. J., 1993, "Conversion of the kinematics of a car with n trailers into a chained form," presented at Proceedings of the IEEE International Conference on Robotics and Automation, Atlanta, Ga, pp. 382-387.

Stanisic, M. M., and O. Duta, 1990, "Symmetrically Actuated Double Pointing Systems: The Basis of Singularity -Free Robot Wrists," *IEEE Transactions on Robotics and Automation*, vol. 6, no. 5, pp. 562-569.

Susnjara, K. J., and M. A. Fleck, 1982, "Wrist Construction for Industrial Robots", Thermwood Corporation, Dale, Ind., Oct. 12, 1982, USA, Pat. #4,353,677.

Tayebi, A., M. Tadjine and A. Rachid, 1997, "Invariant Manifold Approach for the Stabilization of Nonholonomic Systems in Chained Form: Application to a Car-like Mobile Robot," presented at Proceedings of the 1997 36th IEEE Conference on Decision and Control, San Diego, Ca, pp. 4038-4043.

Trowbridge, E. A., P. V. Lawford and C. E. Crofts, 1989, "Pericardial heterografts: a comparative study of suture pull-out and tissue strength.," *J Biomed Eng*, vol. 11, no. 4, pp. 311-14.

Tummala, R. L., R. Mukherjee, D. Aslam, N. Xi, S. Mahadevan and J. Weng, 1999, "Reconfigurable Adaptable Micro Robot," presented at submitted to IEEE SMC, Tokyo, Japan, pp. .

Wales, K. S., J. F. Paraschac and D. Stefanchik, 1997, "Articulating surgical instrument", Ethicon Endo-Surgery, Inc, Dec. 30, 1997, US, Pat. #5,702,408.

White, T. S., N. Hower, B. L. Luk and J. Hazel, 1998, "Design and Operational Performance of a climbing robot used for weld inspection in hazardous environments.," presented at IEEE Conference on Control Applications, pp. 451-455.

Wilson, J., 1990, "First-ever Climbing Robot," in *Electronics World & Wireless World*, vol. 96, pp. 837.

Yano, T., T. Suwa, M. Murakami and T. Yamamoto, 1997, "Development of a Semi Self-Contained Wall Climbing Robot with Scanning Type Suction Cups," presented at IEEE Int Conf on Intelligent Robots and Systems, pp. 900-905.

Yuan, R., W. Lee and S. Yu, 1997, "Mini-laparoscopic cholecystectomy: a cosmetically better, almost scarless procedure.," *J Laparoendosc Adv Surg Tech A (COD)*, vol. 7, no. 4, pp. 205-11.

Zhang, J., G. Guo and W. A. Gruver, 1992, "Optimal design of a six-bar linkage for an anthropomorphic three-jointed finger mechanism," *22nd ASME Biennial Mechanisms Conference, Robotics, Spatial Mechanisms and Mechanical Systems*, vol. 45, pp. 299-304.

Zvenyatsky, B., E. Aranyi and H. J. Tovey, 1995, "Articulating endoscopic surgical apparatus", United States Surgical Corporation, Jan. 24, 1995, US, Pat. #5,383,888.

APPENDICES

Appendix A

DALSA Design Drawings

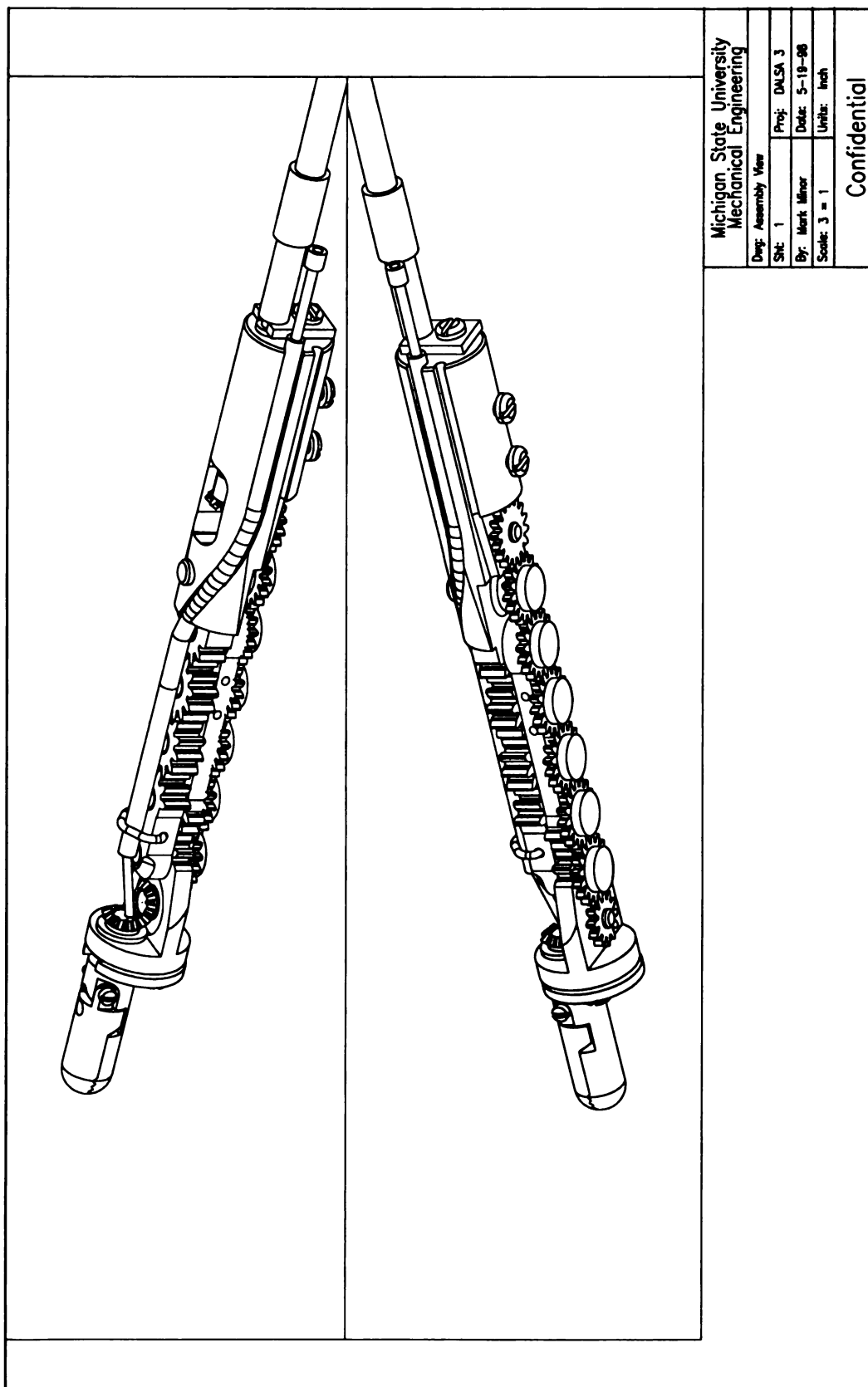


Figure 51. Assembled view of DALSA surgical mechanism (sheet 1).

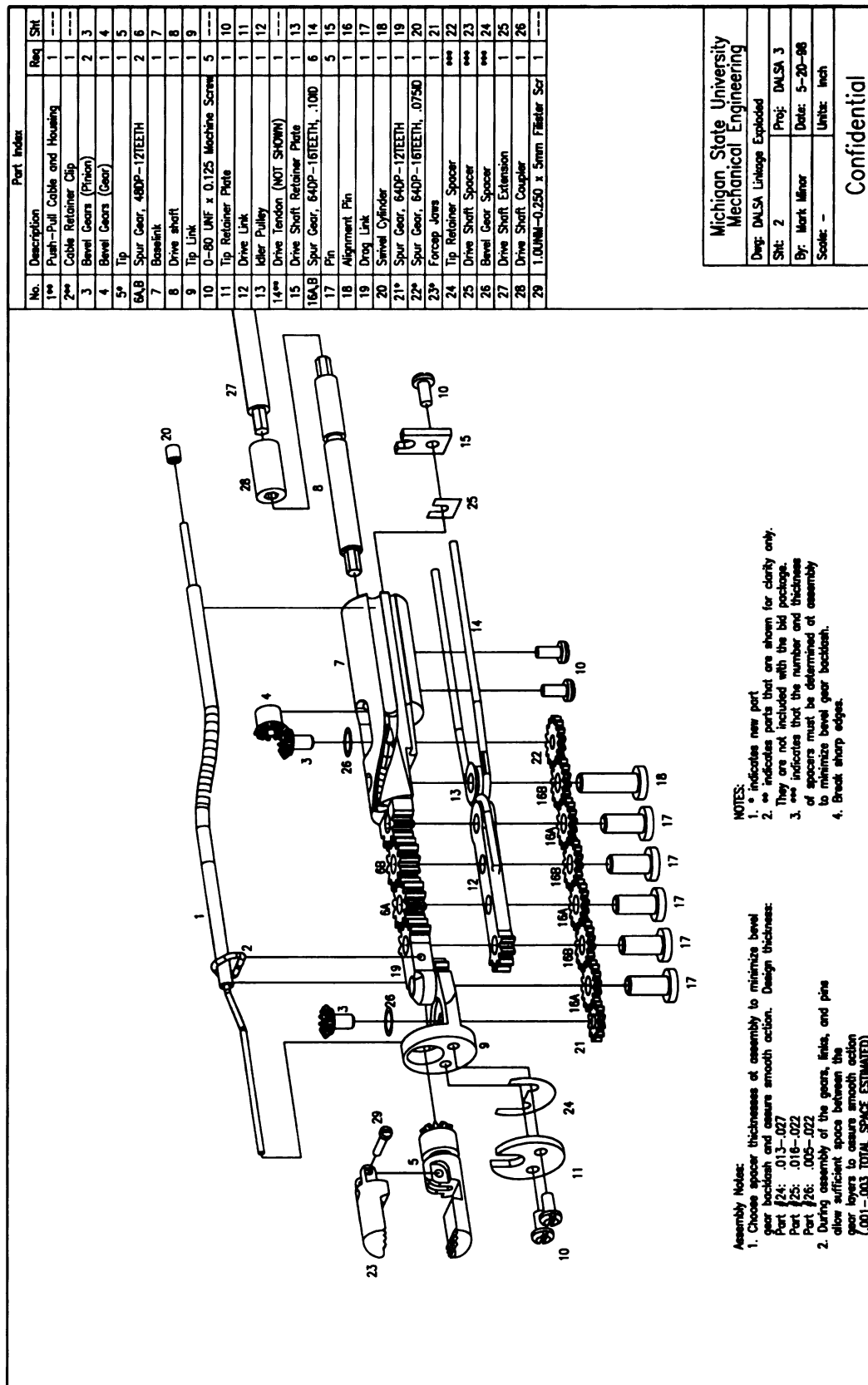


Figure 52. Exploded view of DALSA surgical mechanism (sheet 2).

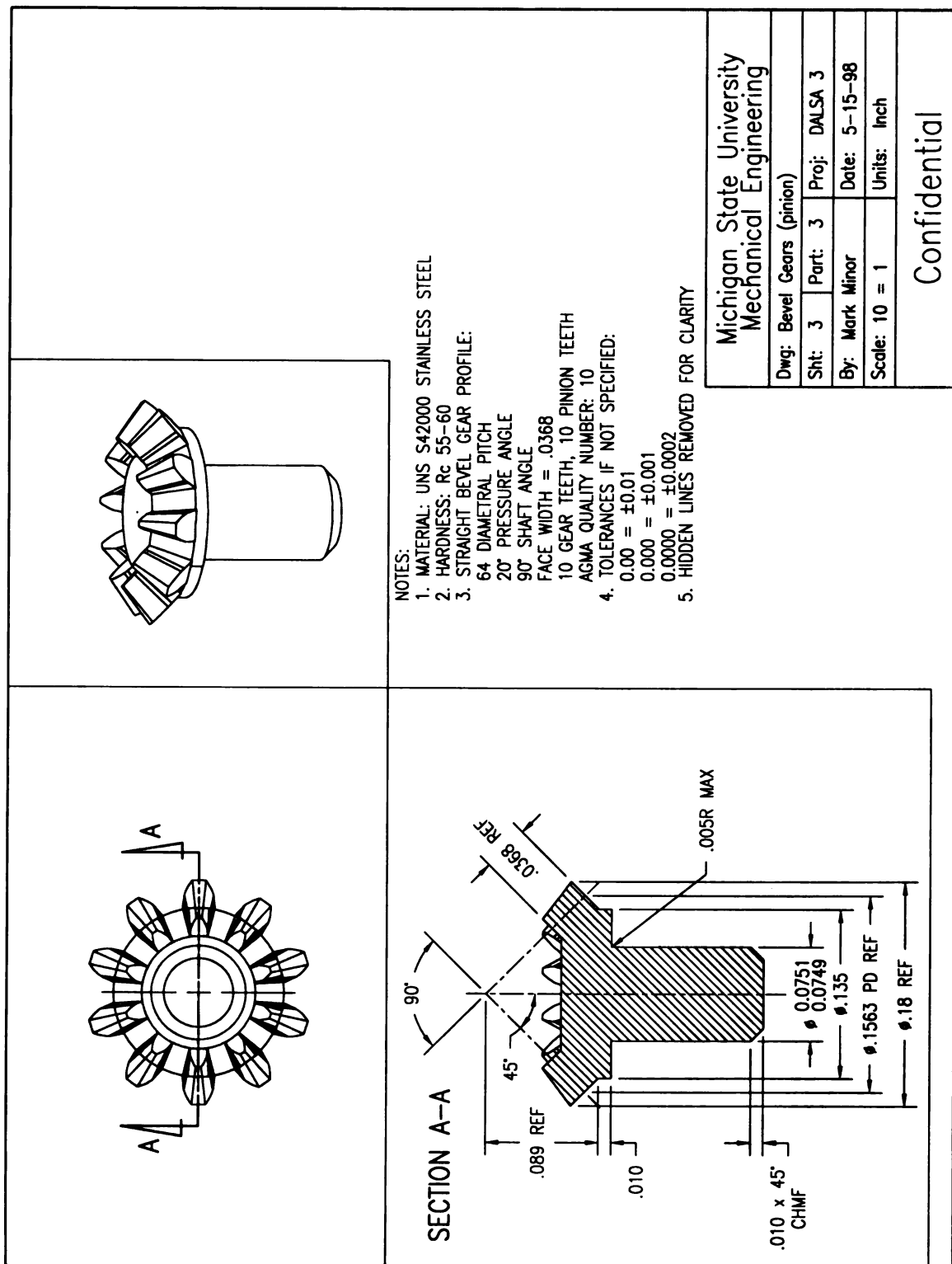


Figure 53. DALSA Component: Bevel Gear Pinion (sheet 3).

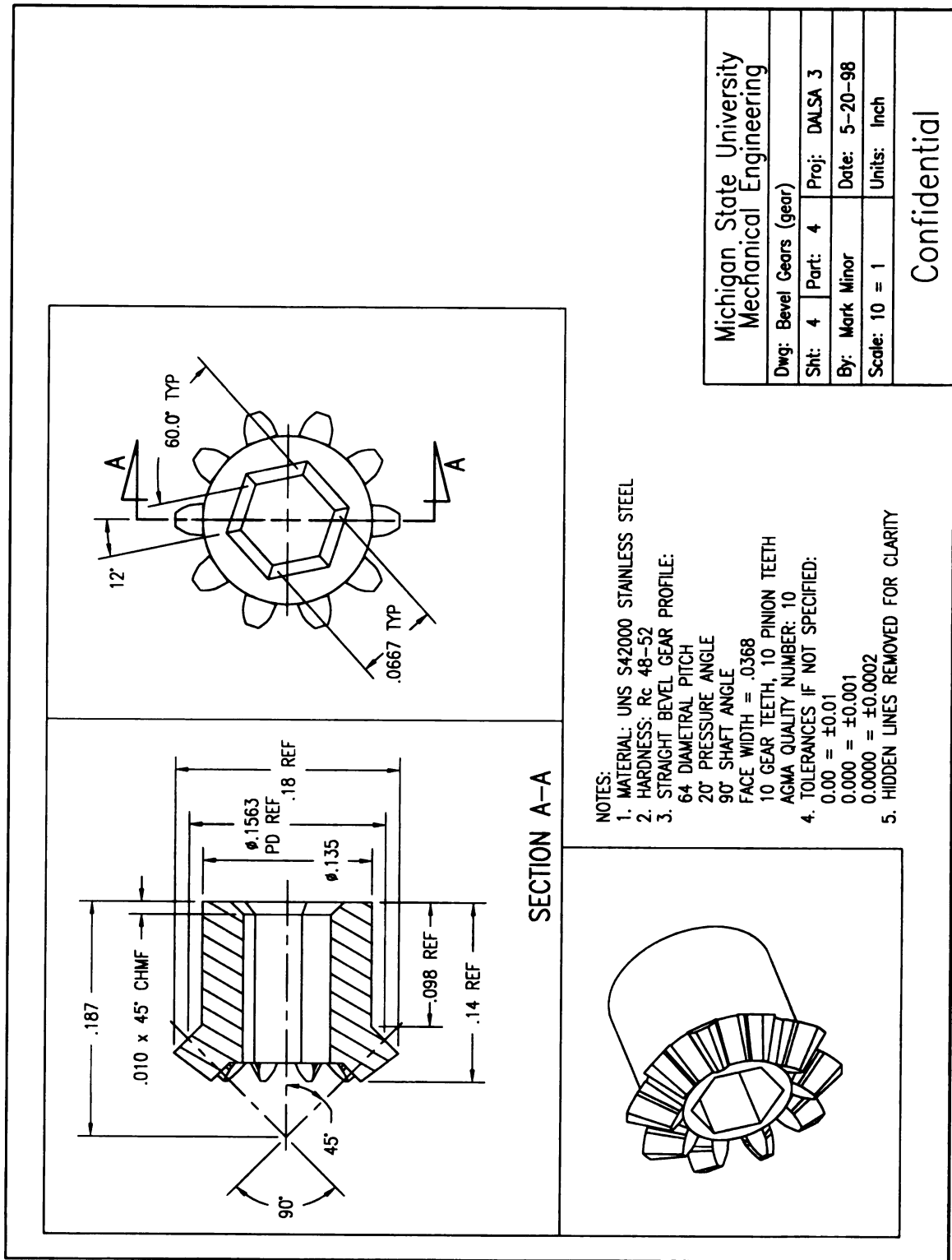
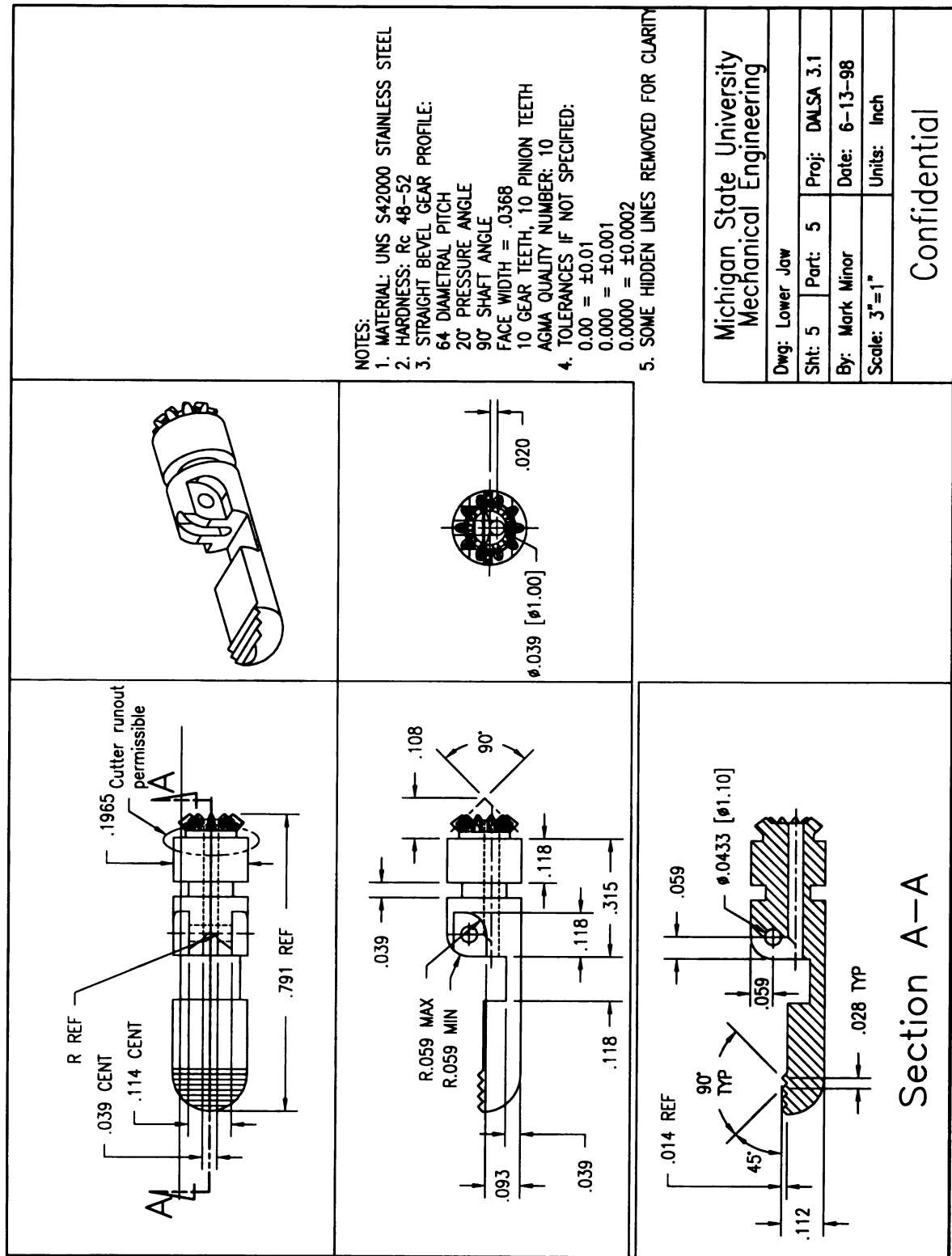


Figure 54. DALSA Component: Bevel Gear (sheet 4).



NOTES:

1. MATERIAL: UNS S42000 STAINLESS STEEL
2. HARDNESS: Rc 48-52
3. STRAIGHT BEVEL GEAR PROFILE:
64 DIAMETRAL PITCH
20° PRESSURE ANGLE
90° SHAFT ANGLE
FACE WIDTH = .0368
10 GEAR TEETH, 10 PINION TEETH
AGMA QUALITY NUMBER: 10
4. TOLERANCES IF NOT SPECIFIED:
0.00 = ± 0.01
0.000 = ± 0.001
0.0000 = ± 0.0002
5. SOME HIDDEN LINES REMOVED FOR CLARITY

Michigan State University
Mechanical Engineering

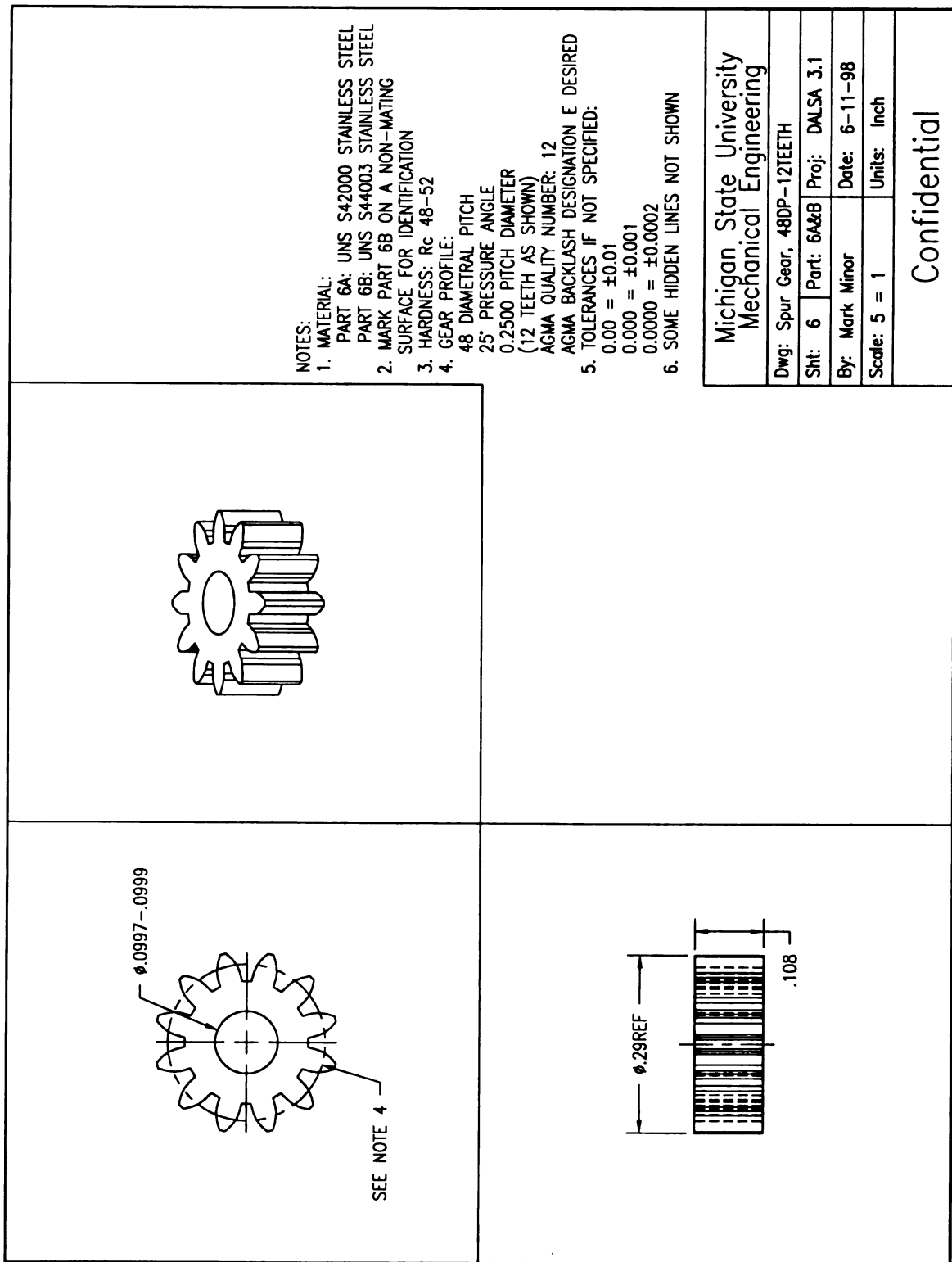
Dwg: Lower Jaw

Sht: 5 Part: 5 Proj: DALSA 3.1

By: Mark Minor Date: 6-13-98

Scale: 3"=1" Units: Inch

Confidential



NOTES:

1. MATERIAL:
PART 6A: UNS S42000 STAINLESS STEEL
PART 6B: UNS S44003 STAINLESS STEEL
2. MARK PART 6B ON A NON-MATING SURFACE FOR IDENTIFICATION
3. HARDNESS: Rc 48-52
4. GEAR PROFILE:
48 DIAMETRAL PITCH
25° PRESSURE ANGLE
0.2500 PITCH DIAMETER
(12 TEETH AS SHOWN)
AGMA QUALITY NUMBER: 12
AGMA BACKLASH DESIGNATION E DESIRED
5. TOLERANCES IF NOT SPECIFIED:
0.00 = ±0.01
0.000 = ±0.001
0.0000 = ±0.0002
6. SOME HIDDEN LINES NOT SHOWN

Michigan State University
Mechanical Engineering

Dwg: Spur Gear, 48DP-12TEETH

Sht: 6 Part: 6A&B Proj: DALSA 3.1

By: Mark Minor Date: 6-11-98

Scale: 5 = 1 Units: Inch

Confidential

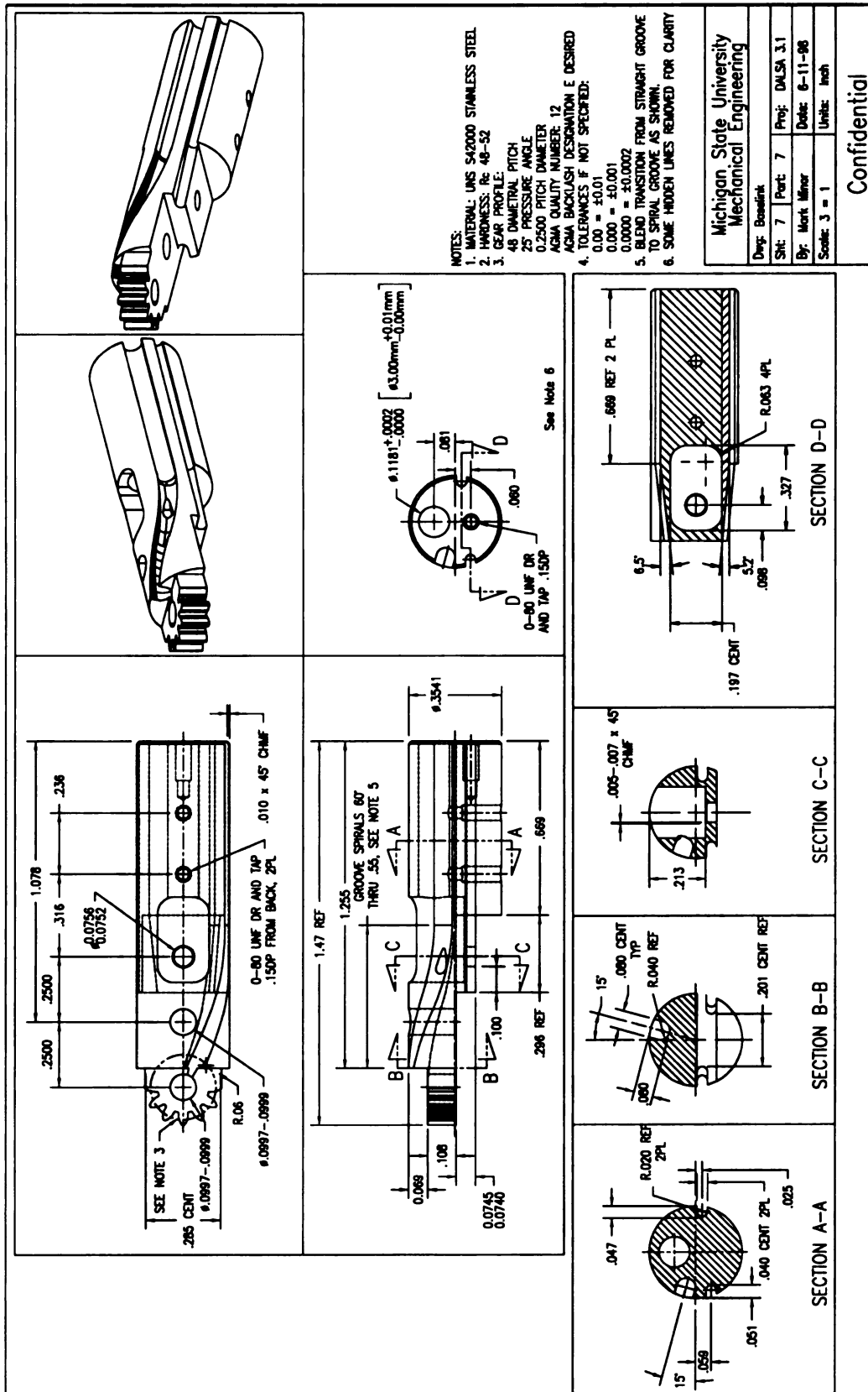


Figure 57. DALSA Component: Base Link (sheet 7).

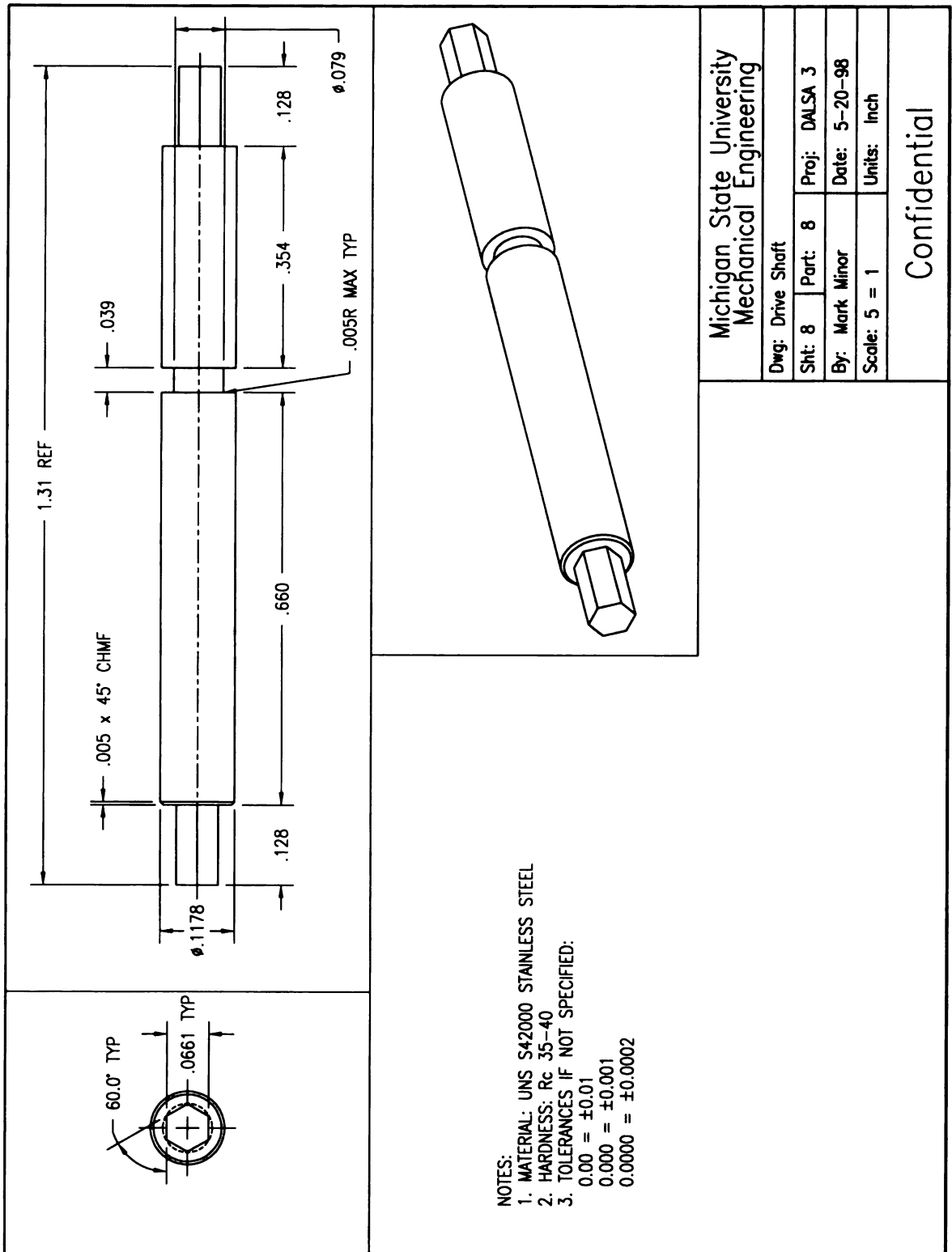


Figure 58. DALSA Component: Drive Shaft (sheet 8).

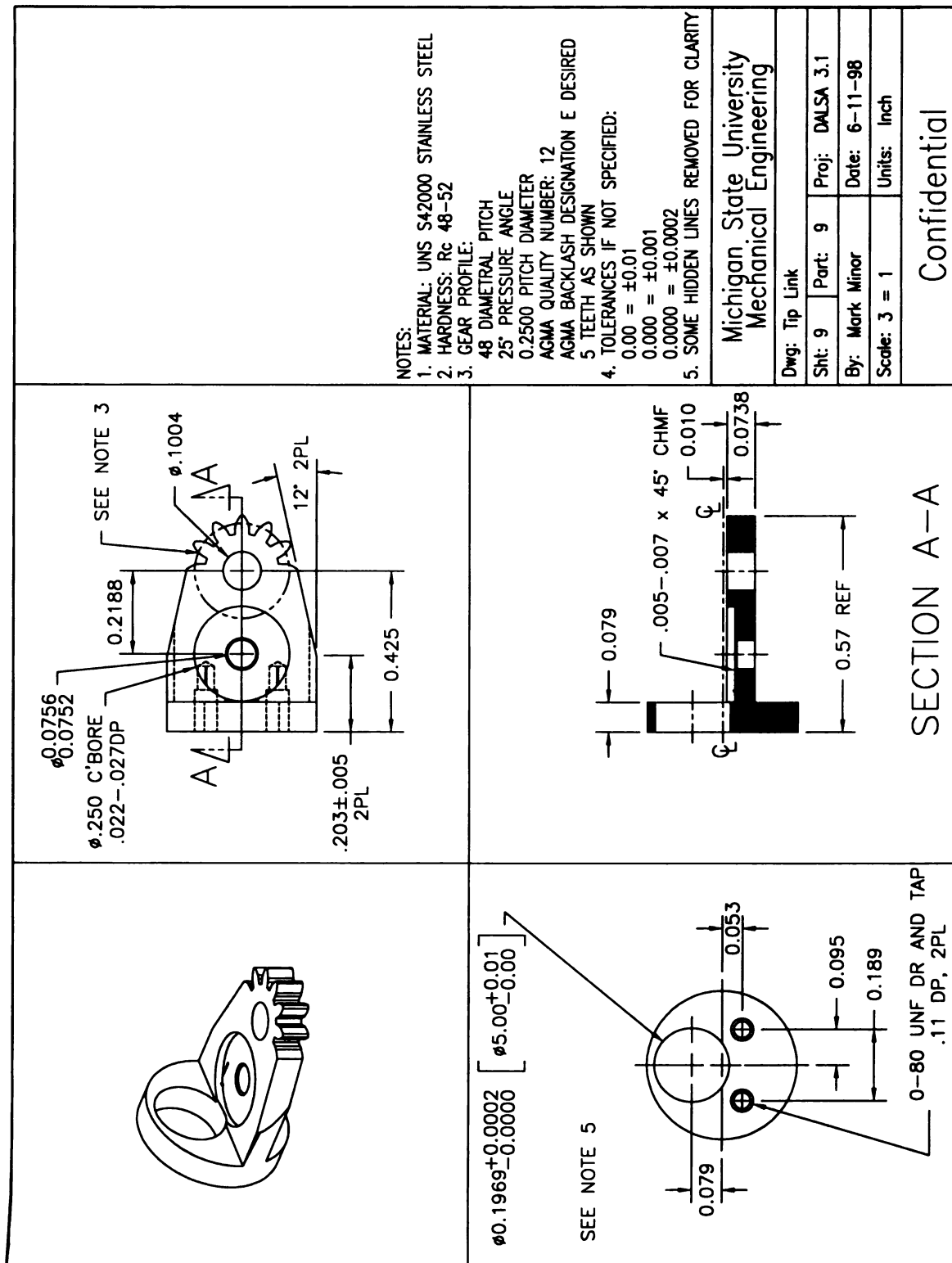


Figure 59. DALSA Component: Tip Link (sheet 9).

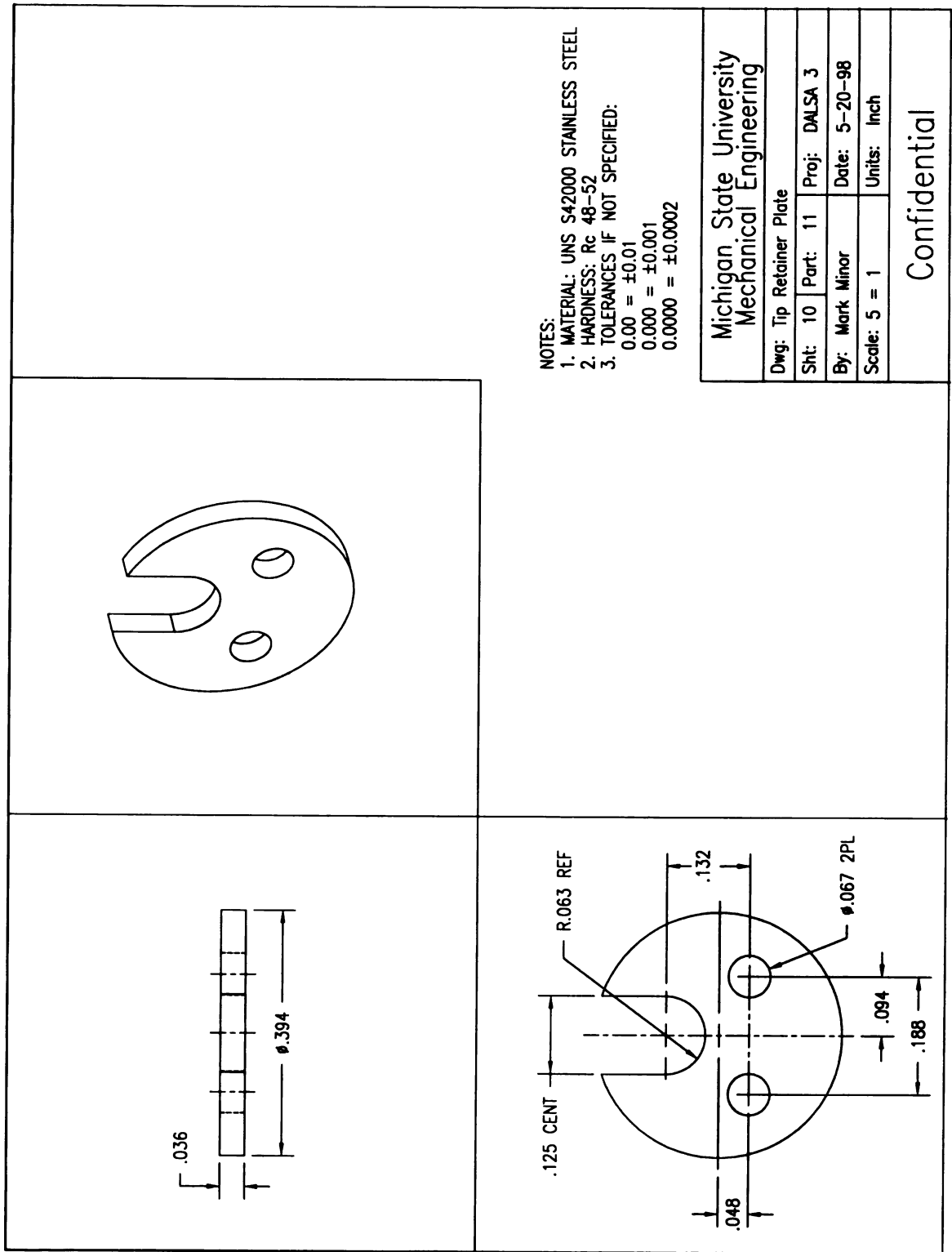


Figure 60. DALSA Component: Tip Retainer Plate (sheet 10).

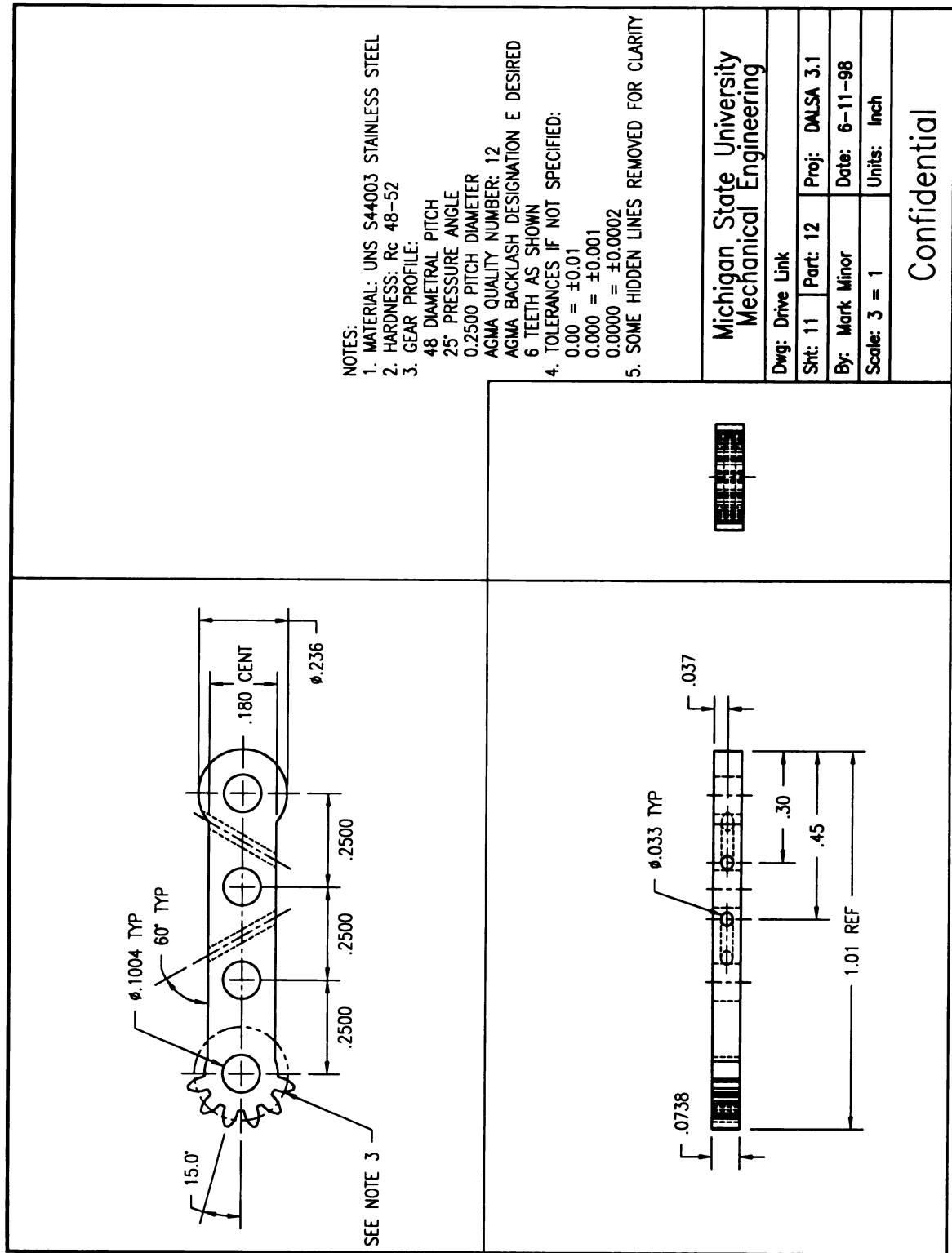


Figure 61. DALSA Component: drive link (sheet 11).

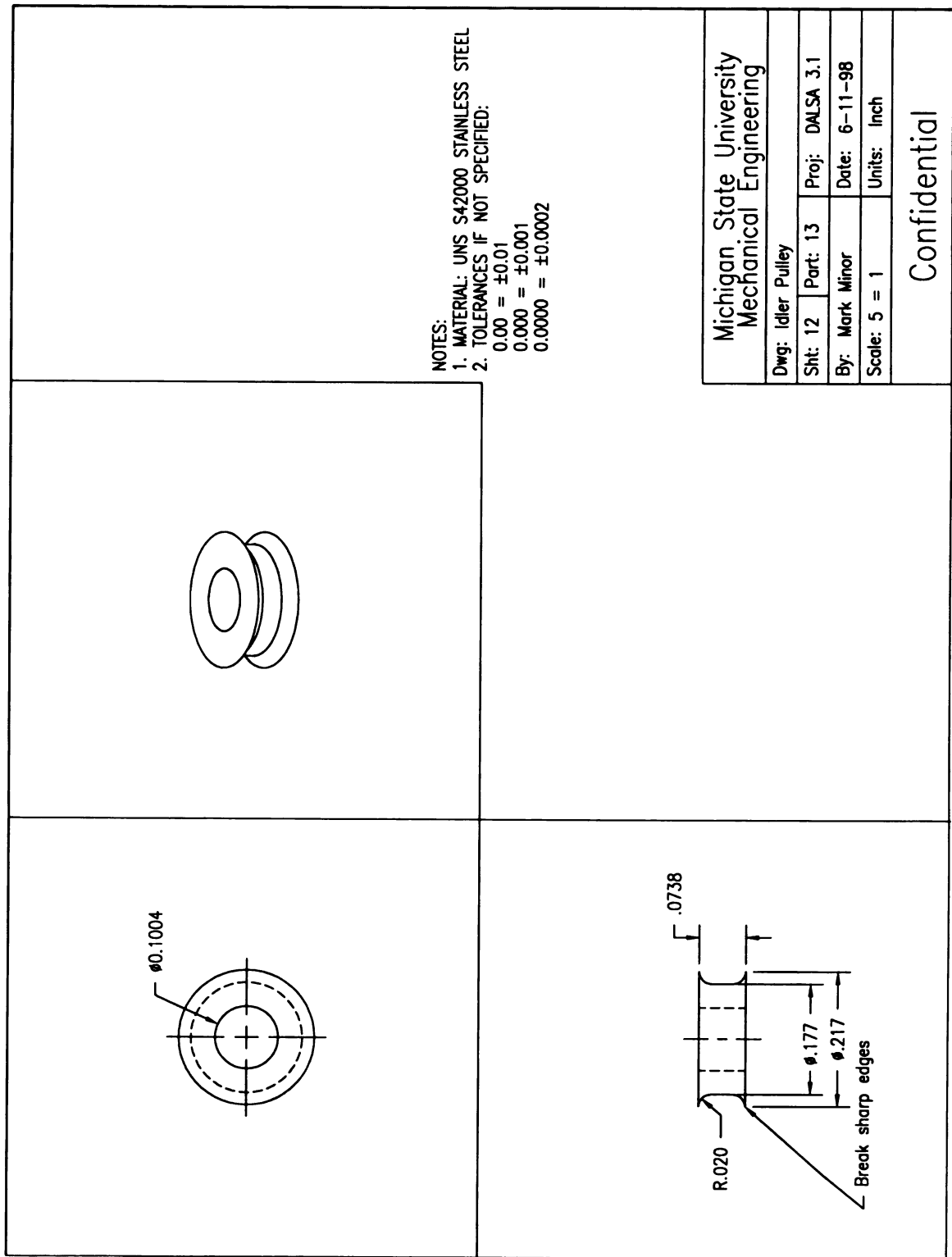


Figure 62. DALSA Component: Idler Pulley (sheet 12).

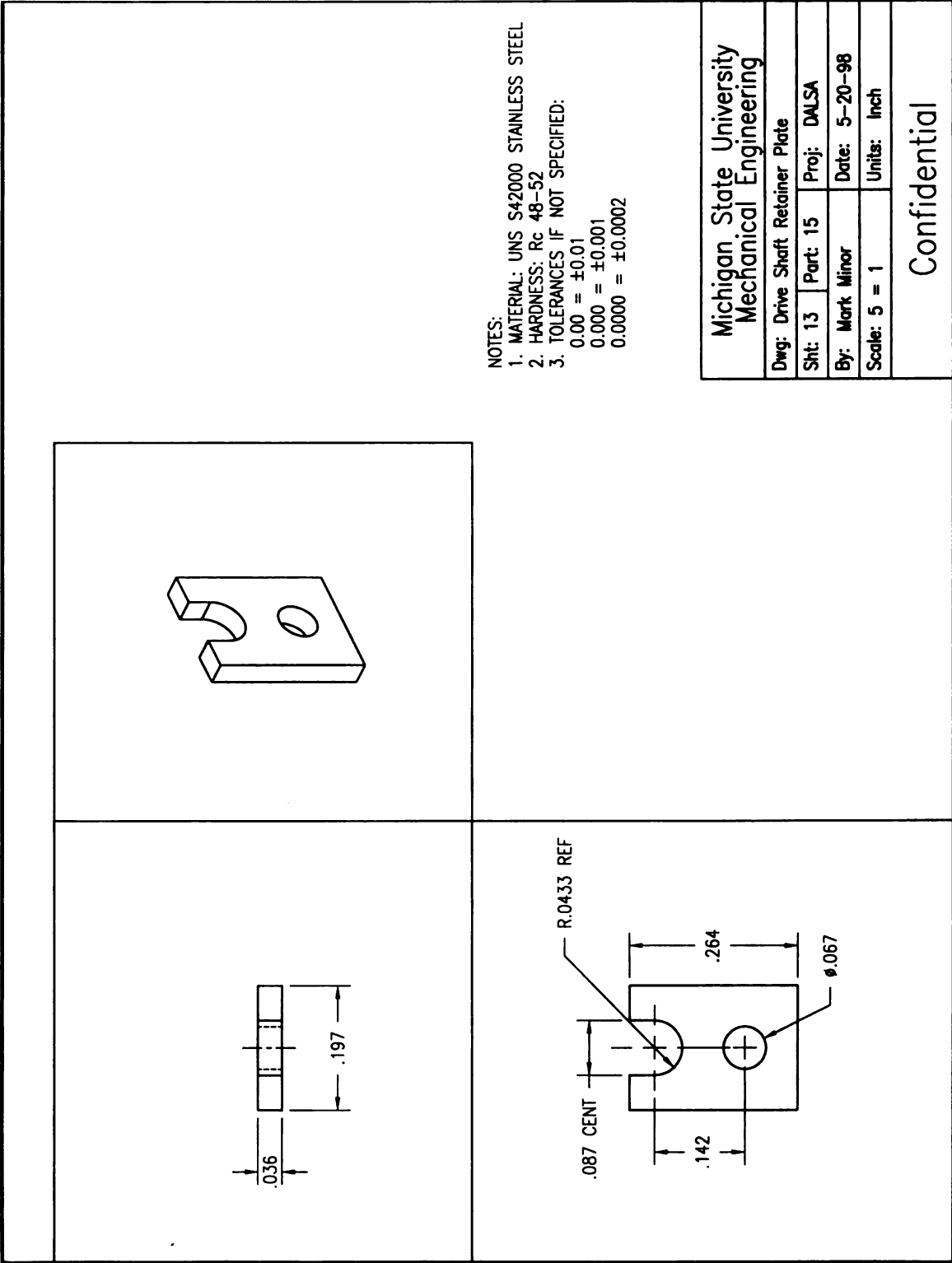


Figure 63. DALSA component: driveshaft retaining plate (sheet 13).

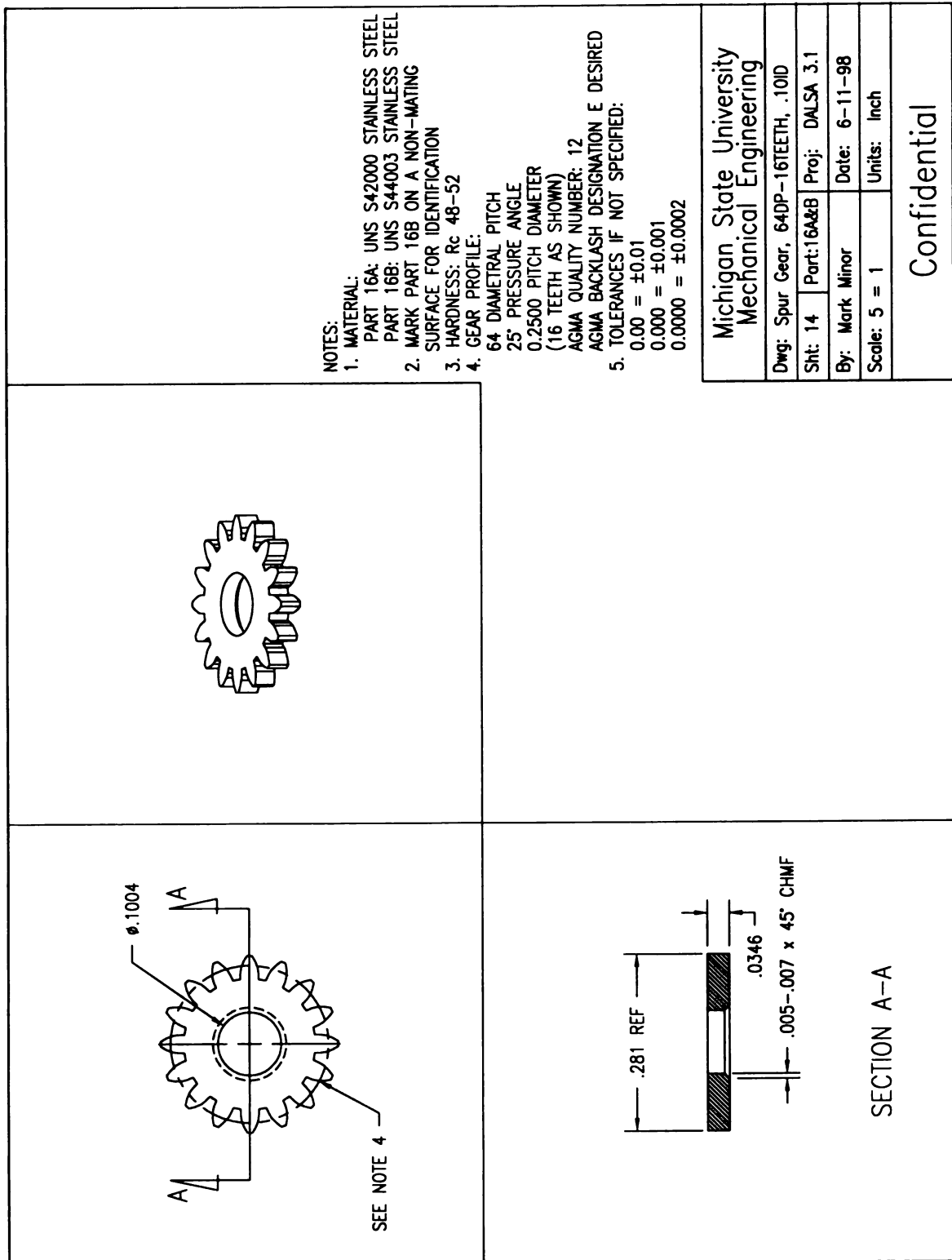


Figure 64. DALSA Component: Spur Gear 64DP, 16 Teeth (sheet 14).

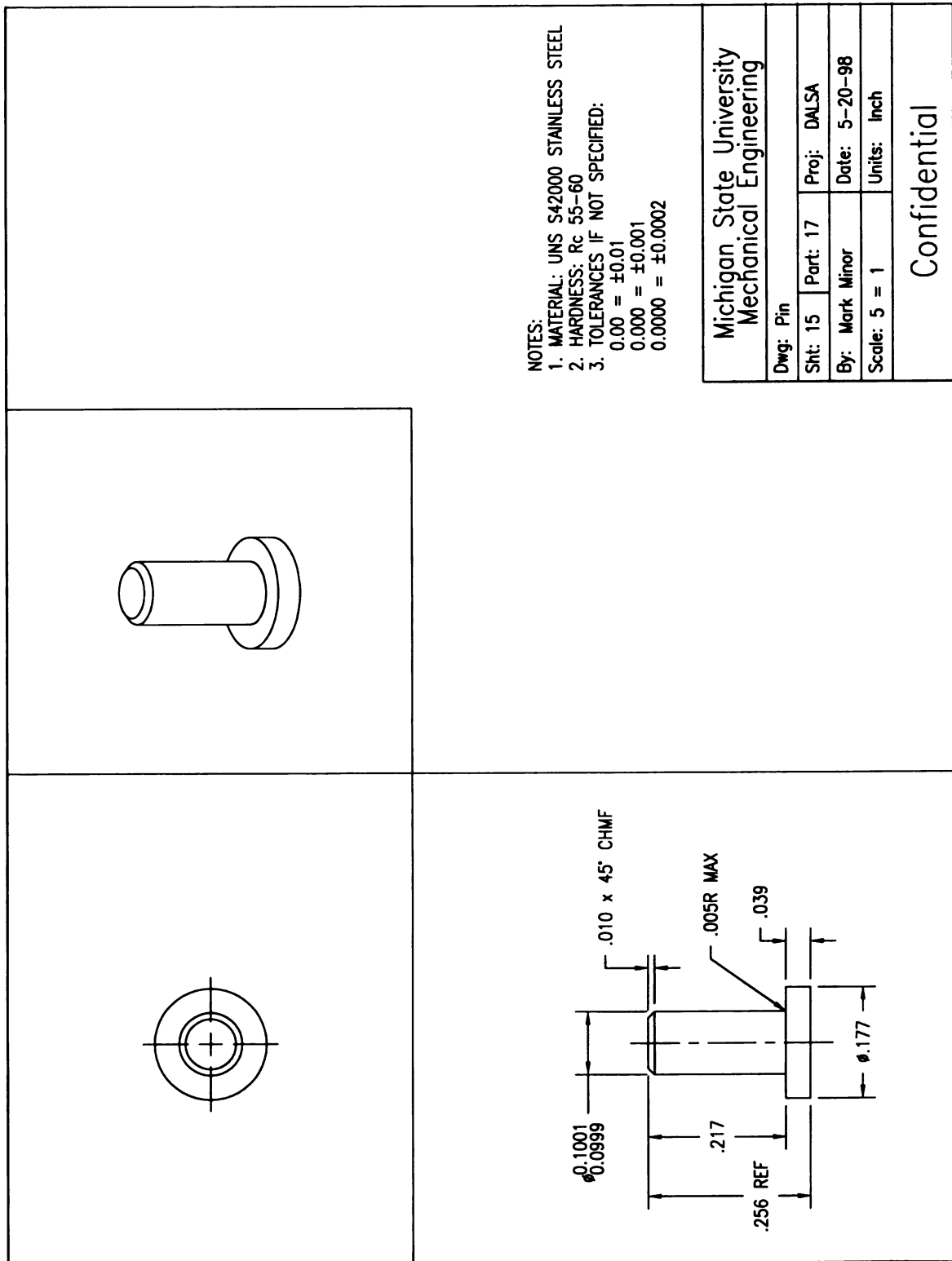


Figure 65. DALSA Component: Pin (sheet 15).

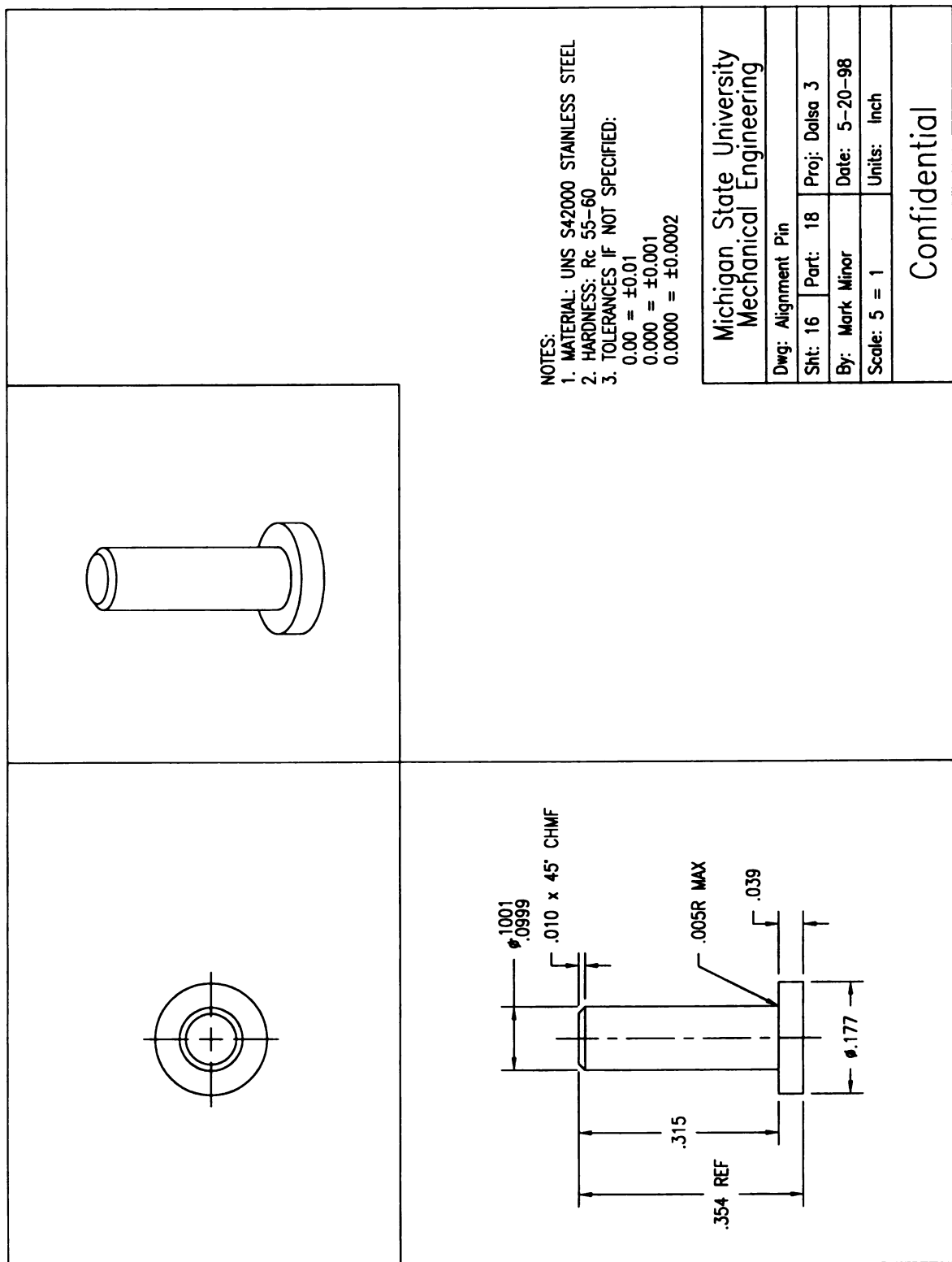


Figure 66. DALSA Component: Alignment Pin (sheet 16).

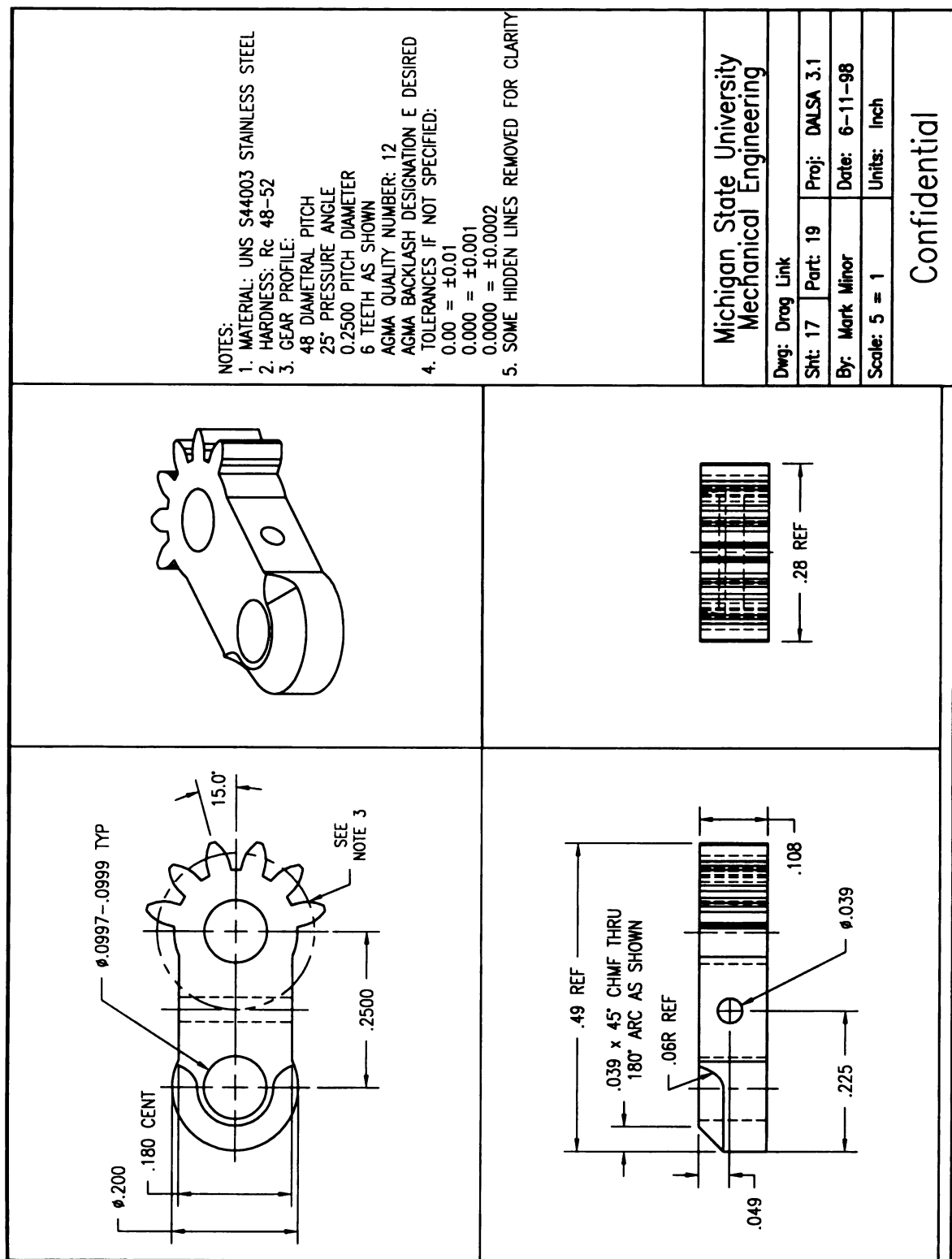


Figure 67. DALSA Component: Drag Link (sheet 17).

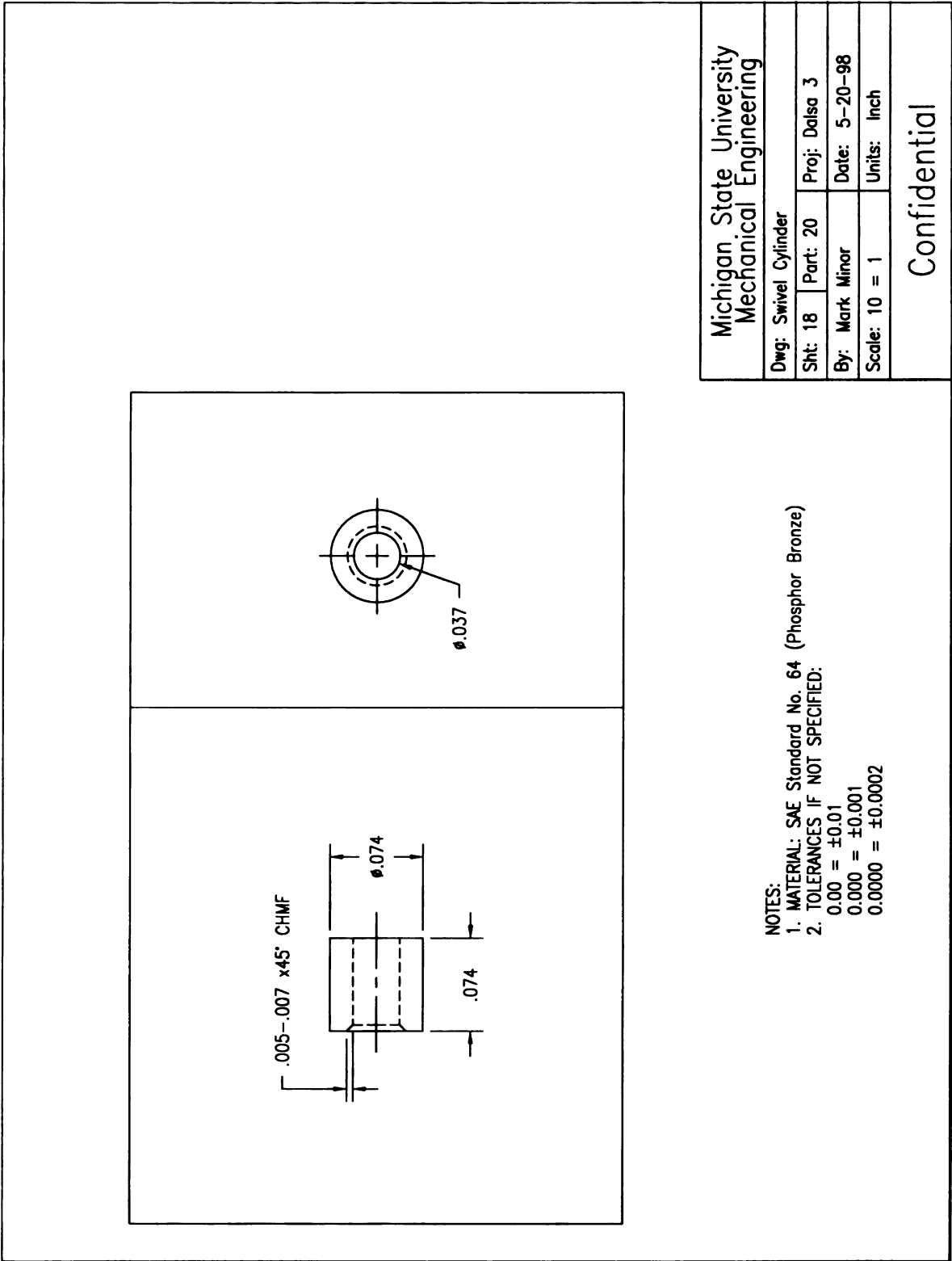


Figure 68. DALSA Component: Swivel (sheet 18).

| | | | |
|---|---------------|---------------|--|
| Michigan State University Mechanical Engineering | | | |
| Dwg: Swivel Cylinder | | | |
| Sht: 18 | Part: 20 | Proj: Dalsa 3 | |
| By: Mark Minor | Date: 5-20-98 | | |
| Scale: 10 = 1 | Units: Inch | | |
| Confidential | | | |

NOTES:
 1. MATERIAL: SAE Standard No. 64 (Phosphor Bronze)
 2. TOLERANCES IF NOT SPECIFIED:
 $0.00 = \pm 0.01$
 $0.000 = \pm 0.001$
 $0.0000 = \pm 0.0002$

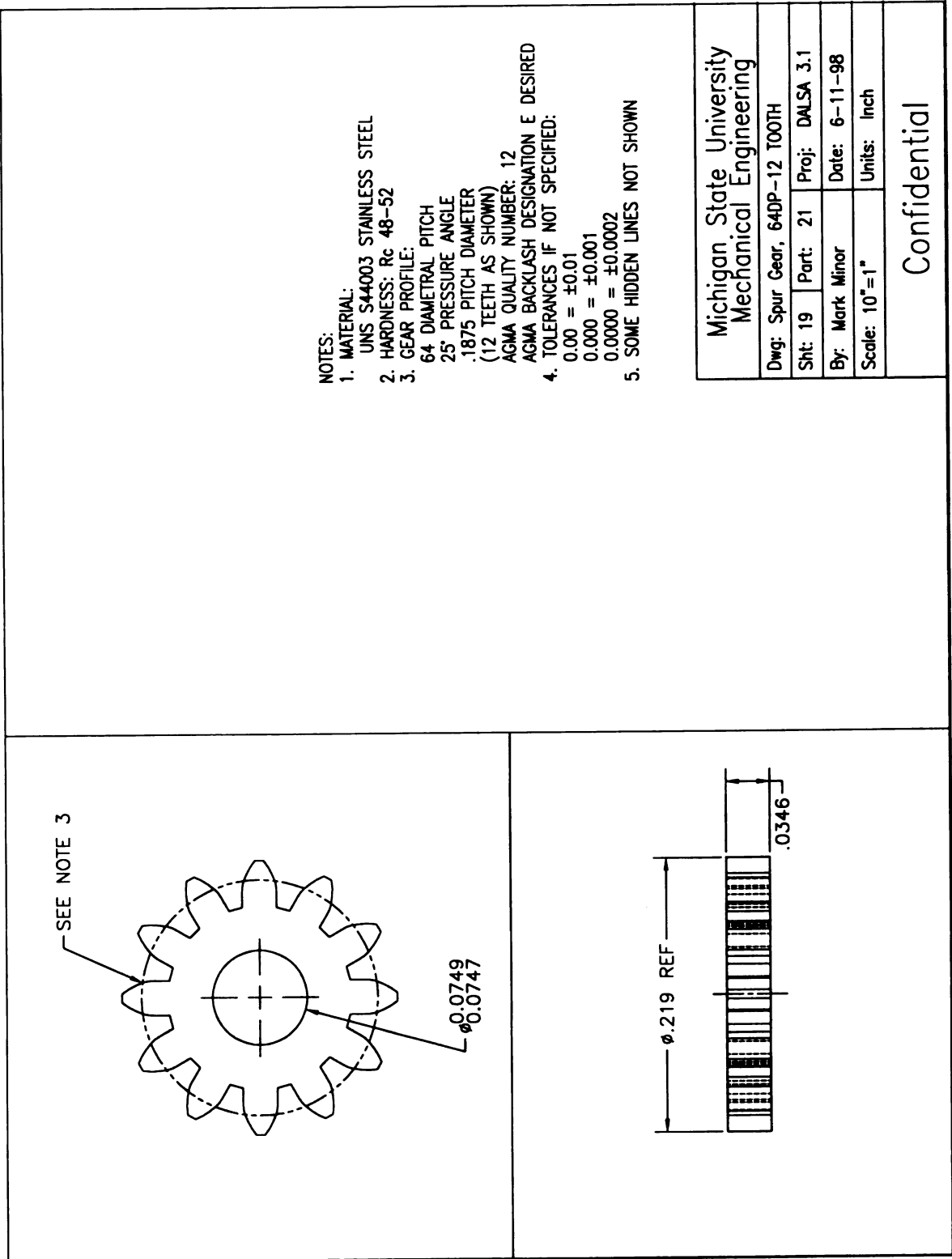


Figure 69. DALSA Component: Spur Gear 64DP, 12 Tooth (sheet 19).

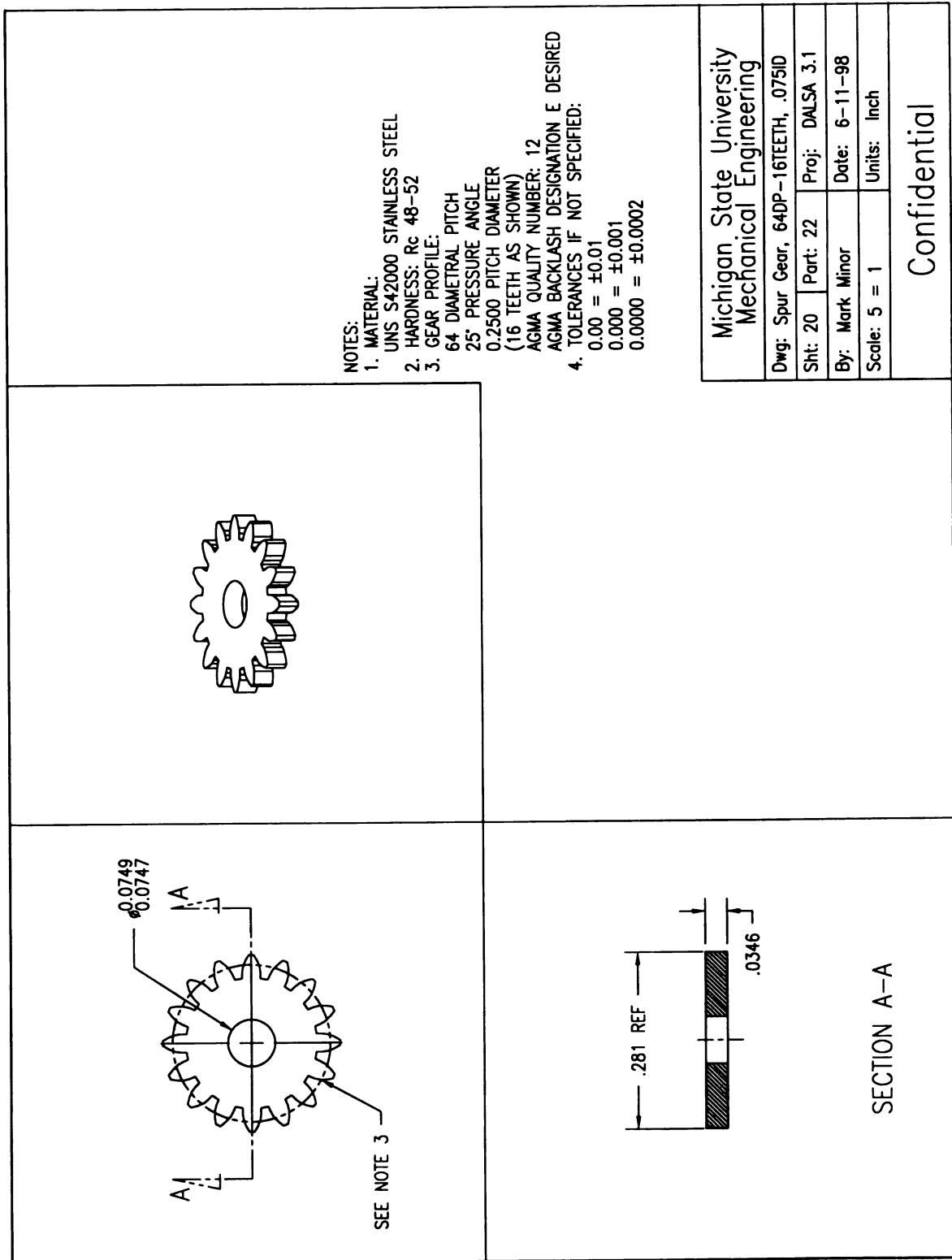


Figure 70. DALSA Component: Spur Gear 64DP, 16 Tooth, .075ID (sheet 20).

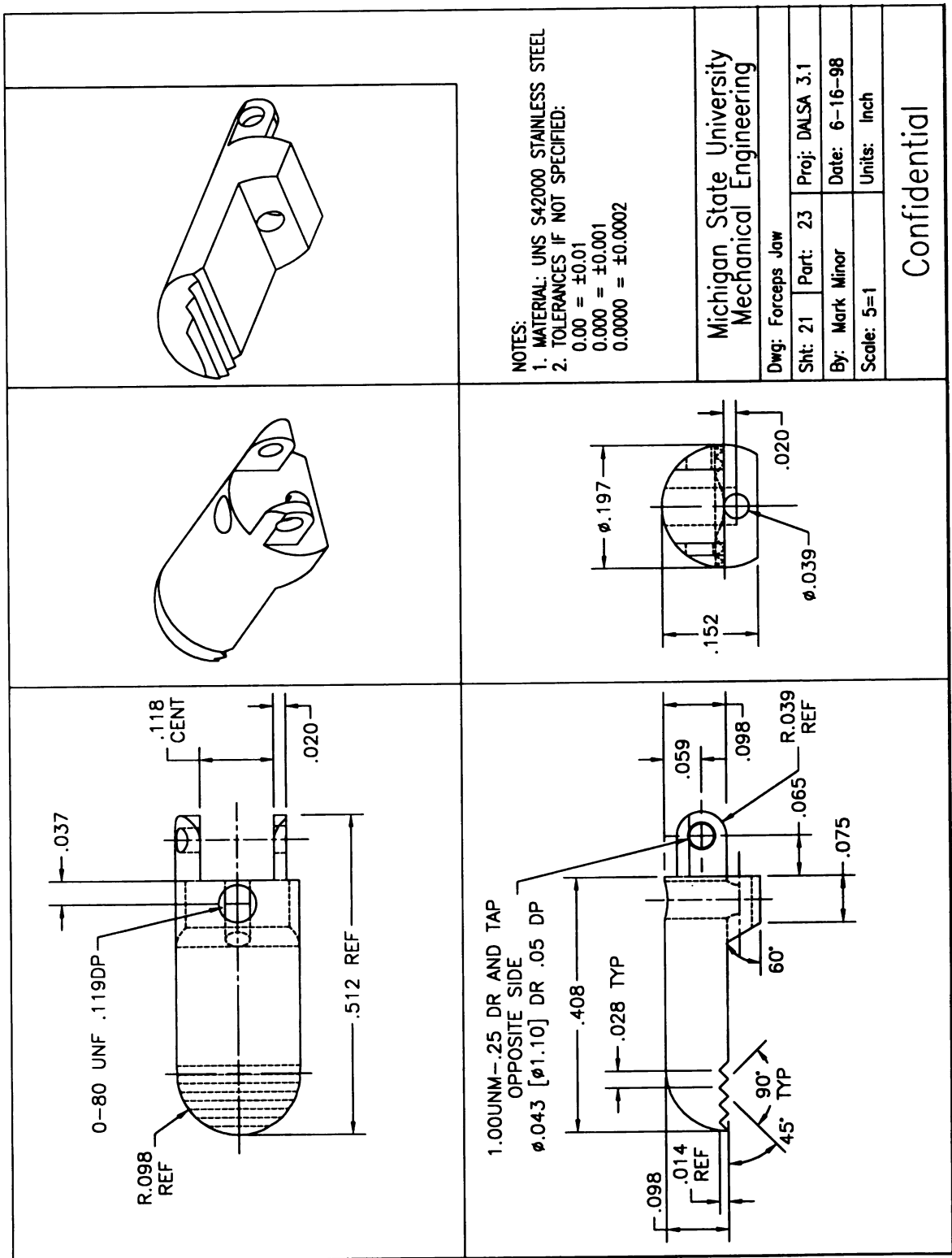


Figure 71. DALSA Component: Forceps Jaw (sheet 21).

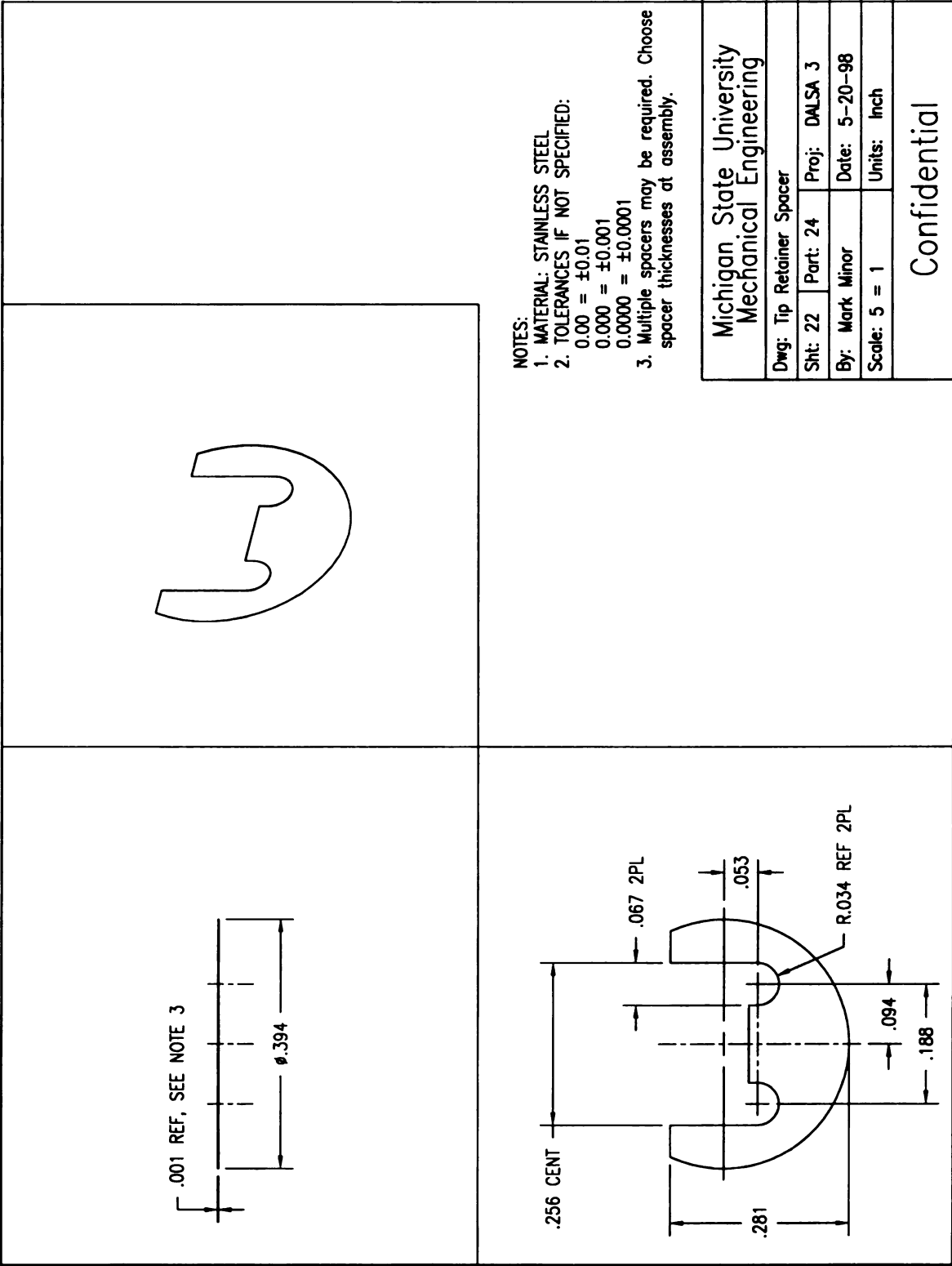


Figure 72. DALSA Component: Tip Retainer Spacer (sheet 22).

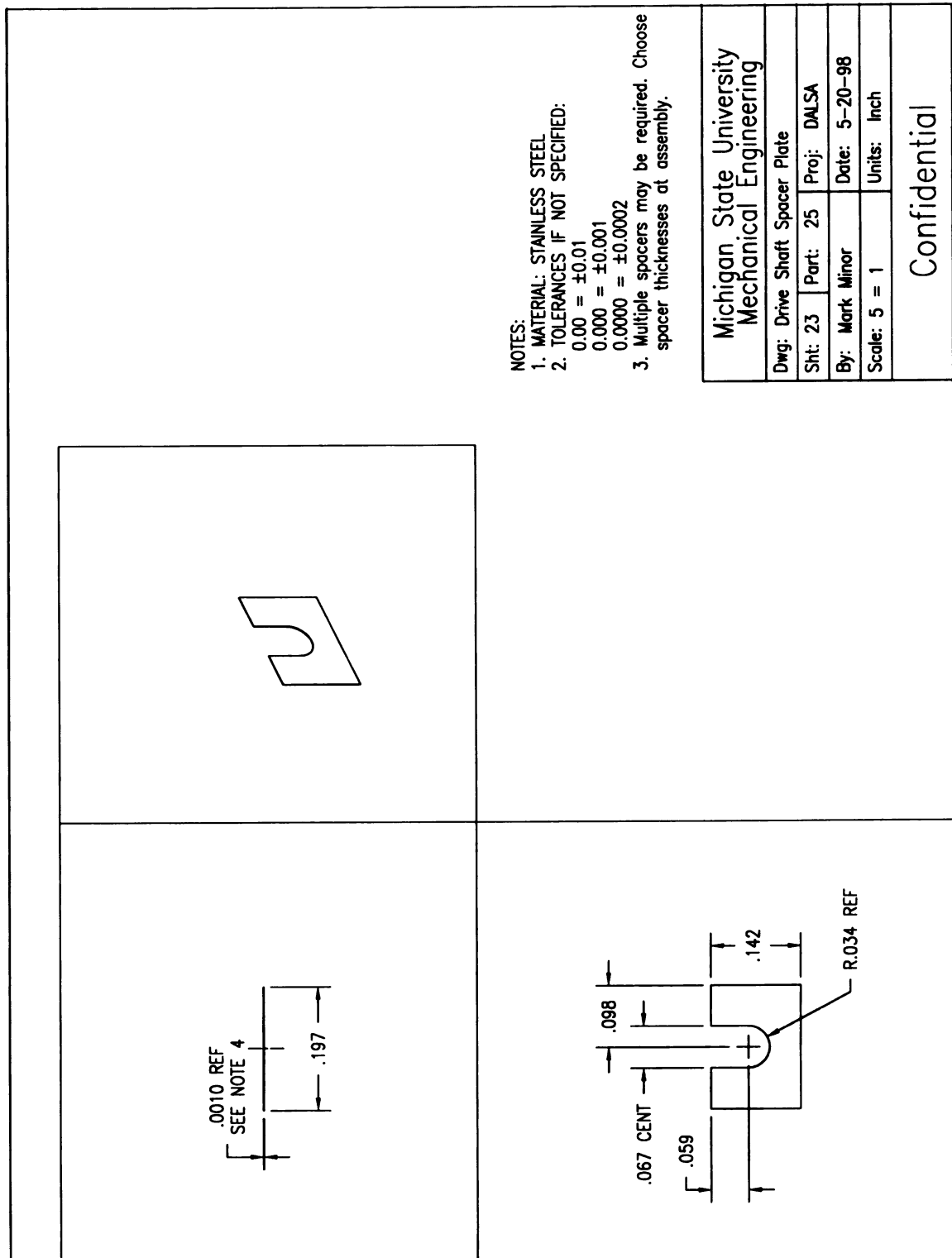


Figure 73. DALSA Component: Drive Shaft Spacer (sheet 23).

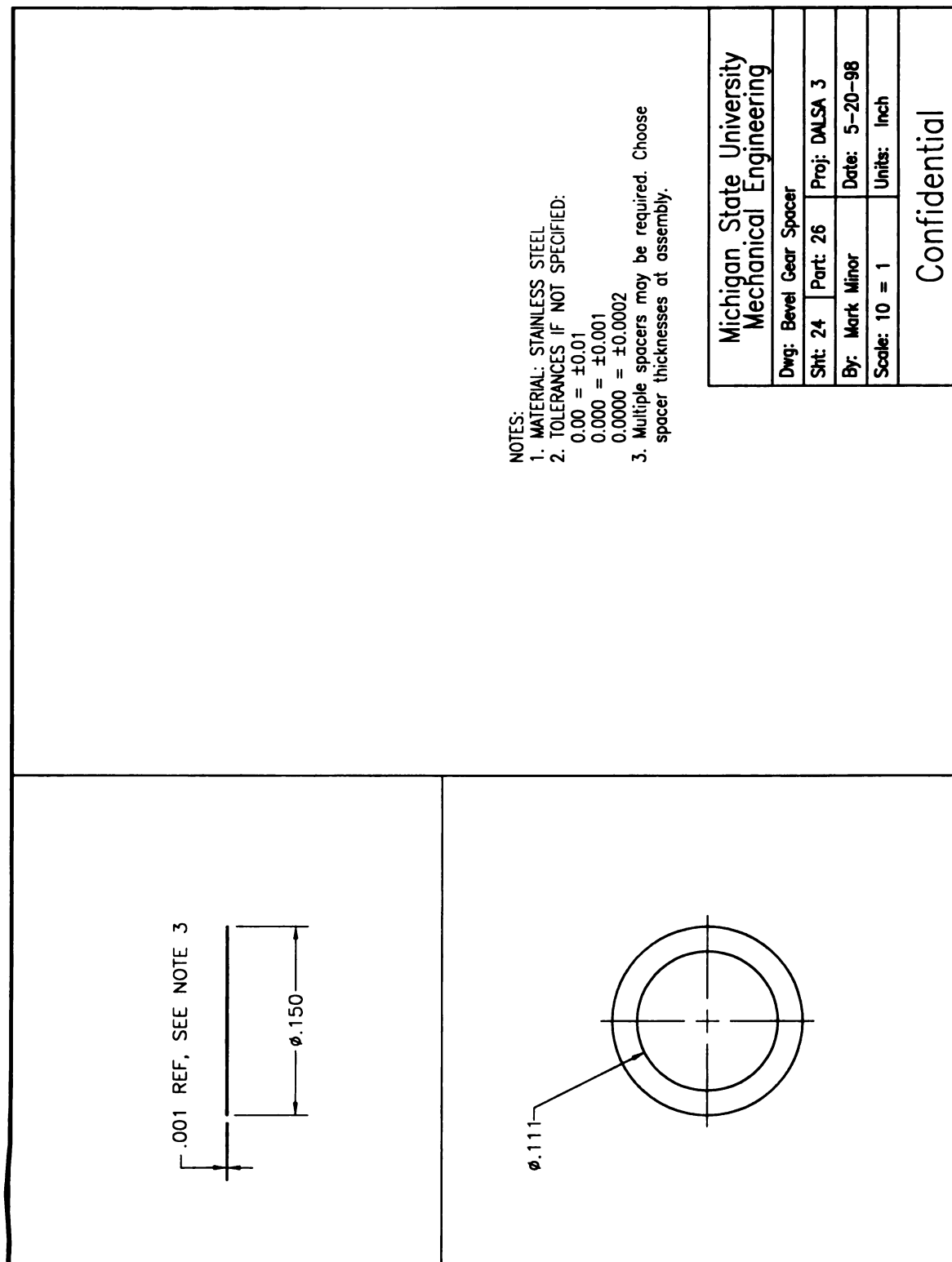


Figure 74. DALSA Component: Bevel Gear Spacer (sheet 24).

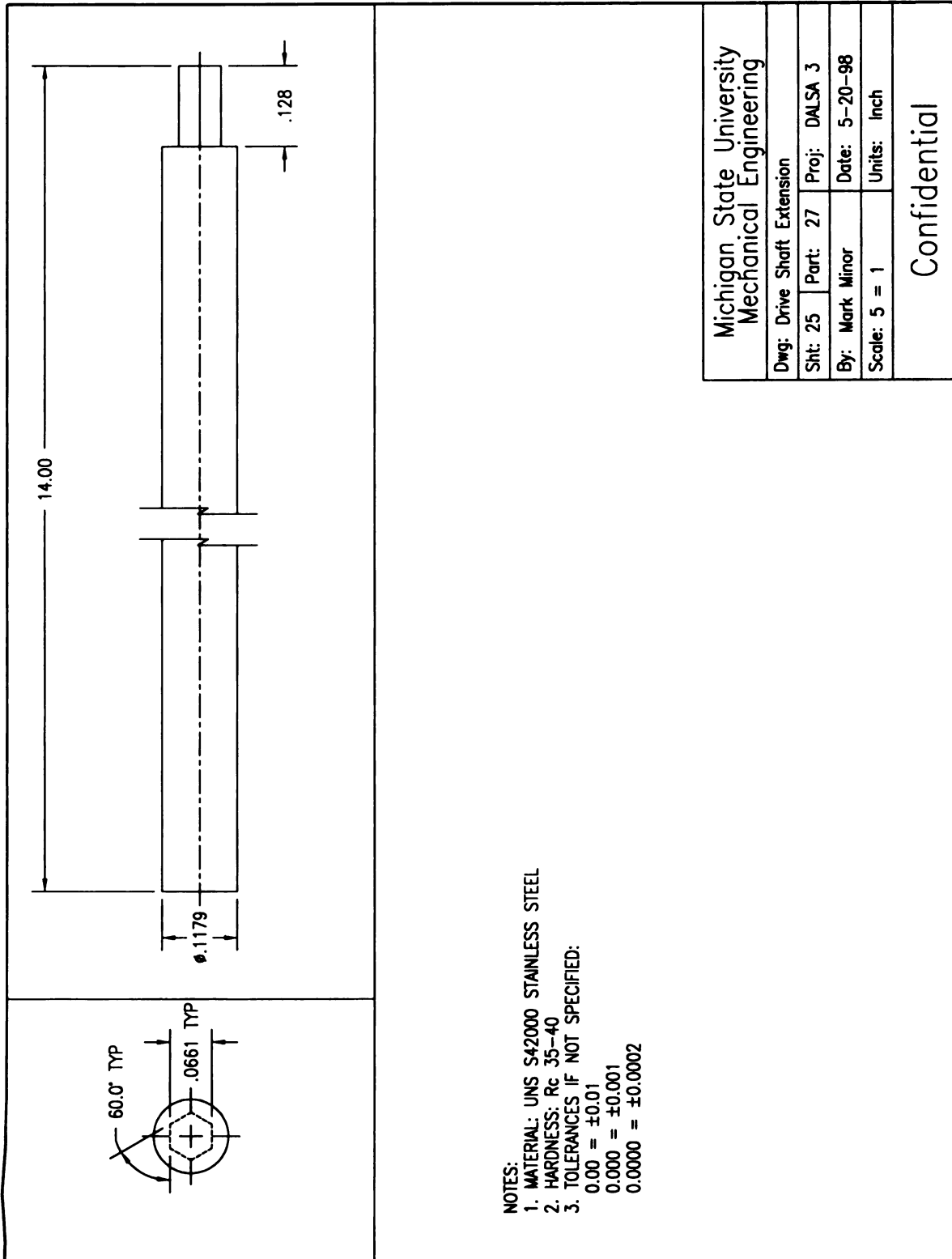


Figure 75. DALSA Component: Drive Shaft Extension (sheet 25).

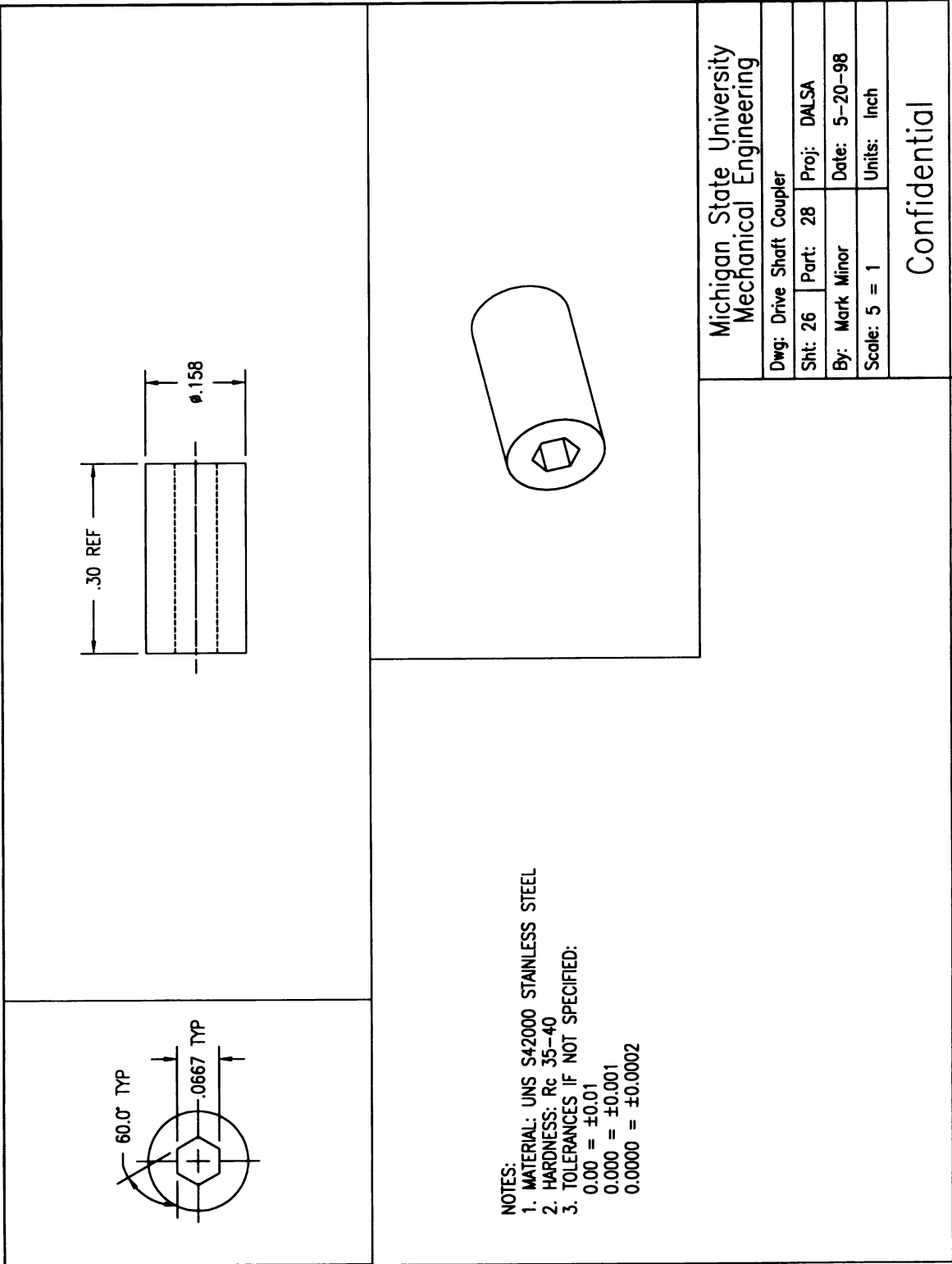


Figure 76. DALSA Component: Drive Shaft Coupler (sheet 26).

Appendix B

Climbing Robot Design Drawings

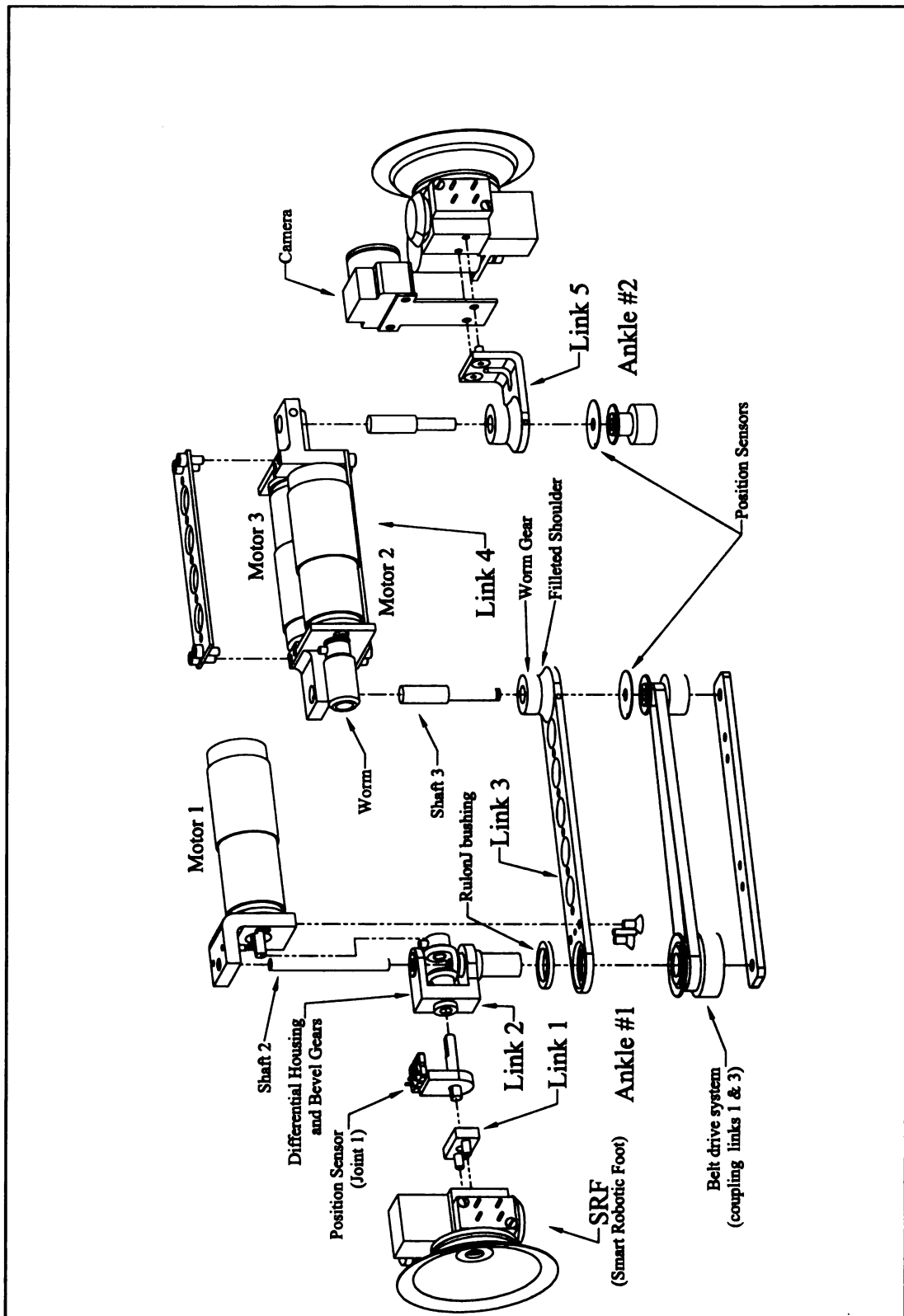


Figure 77. Exploded View of the RAMR1 climbing robot.

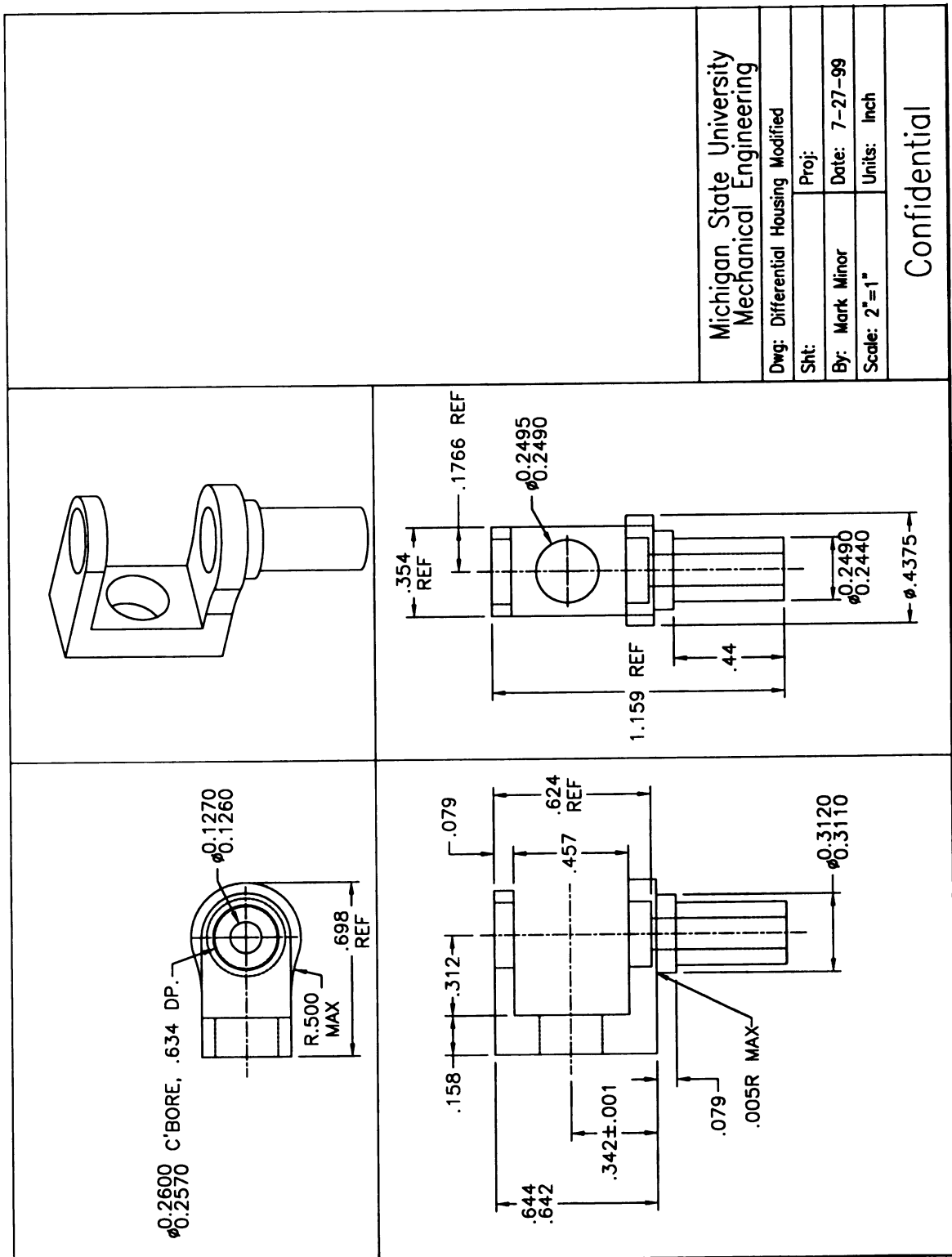


Figure 78. RAMR1 Component: Differential Housing

Michigan State University
Mechanical Engineering

Dwg: Differential Housing Modified

Sht: Proj:

By: Mark Minor Date: 7-27-99

Scale: 2"=1" Units: Inch

Confidential

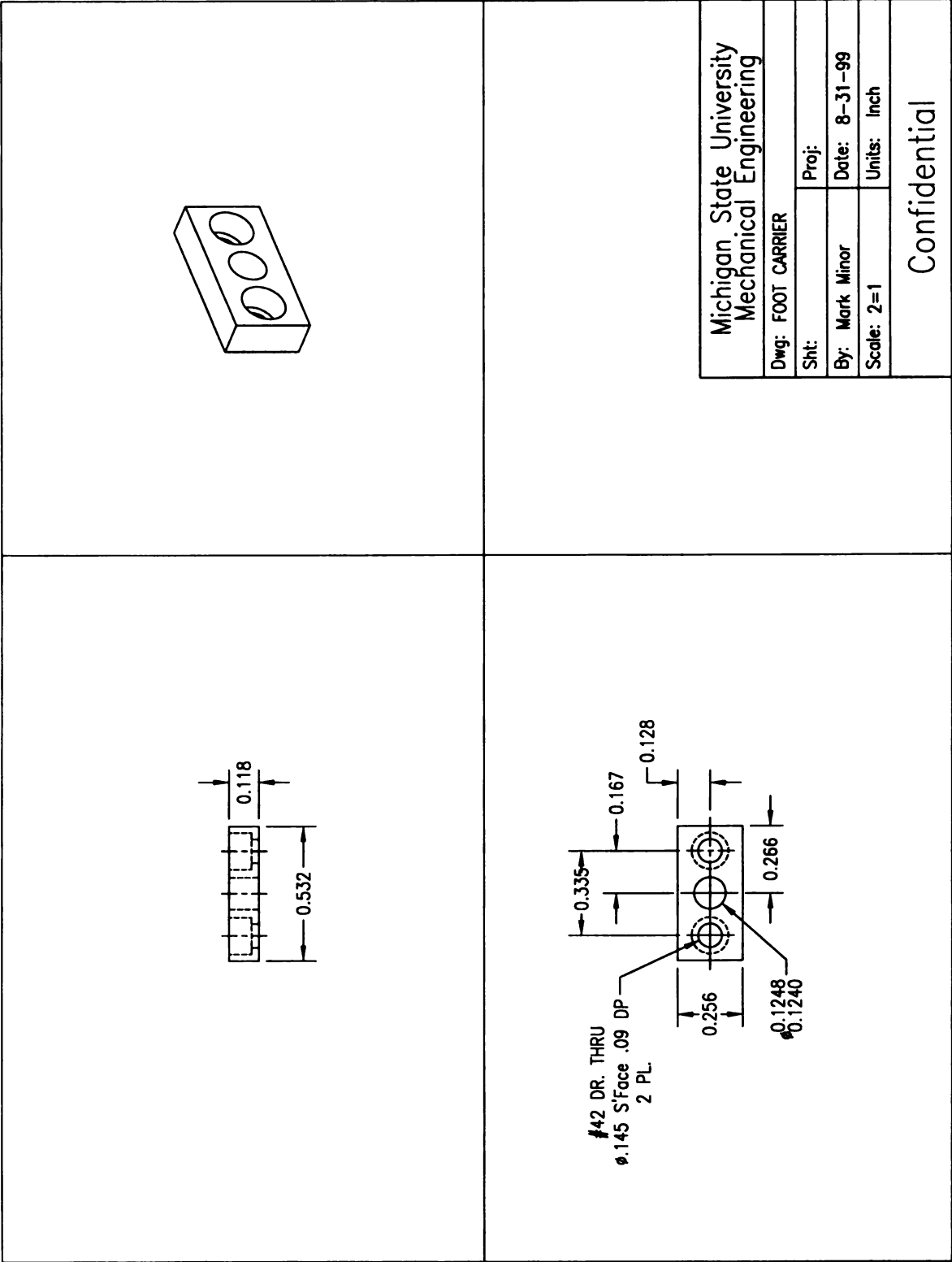


Figure 79. RAMR1 Component: Bracket for Foot #1.

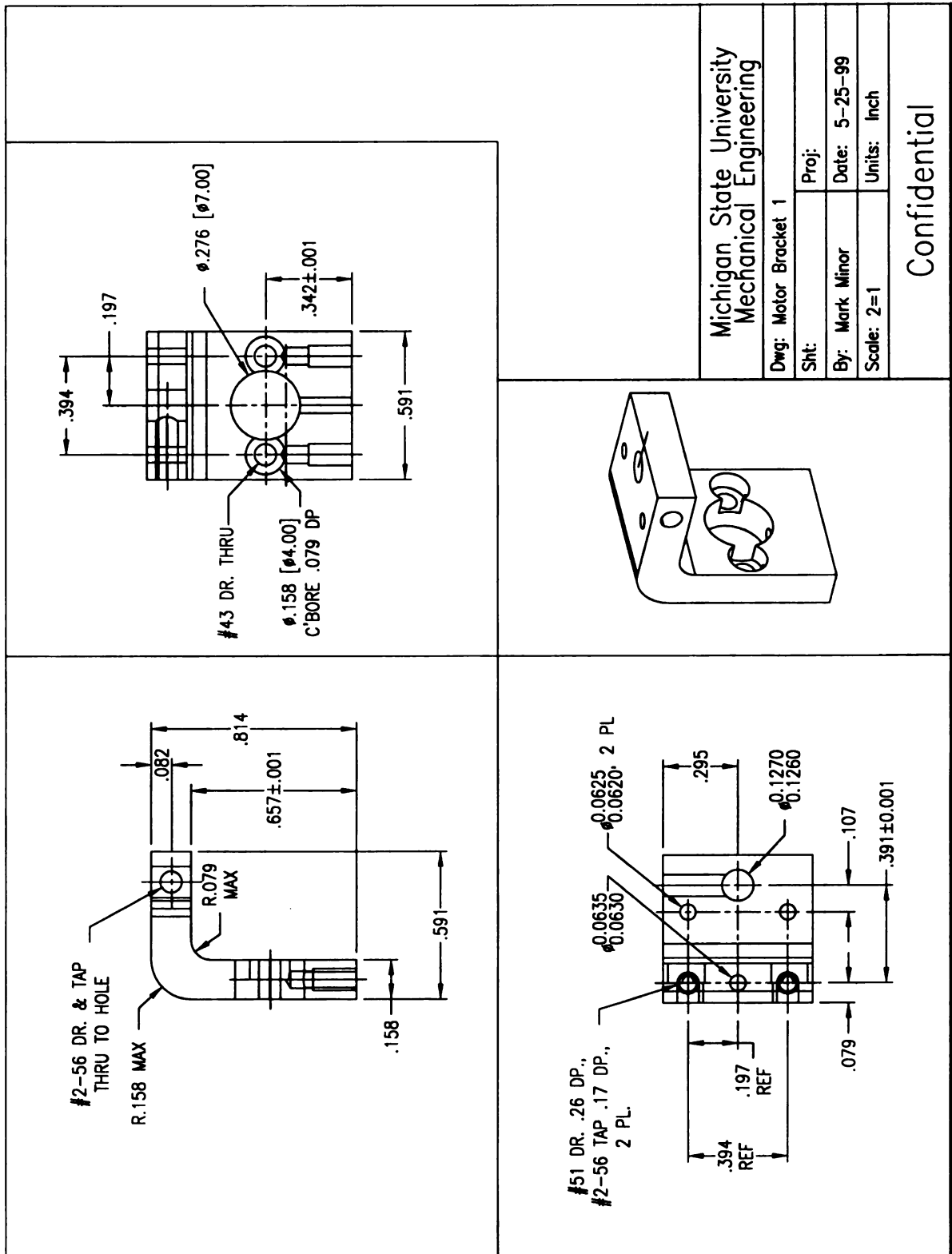
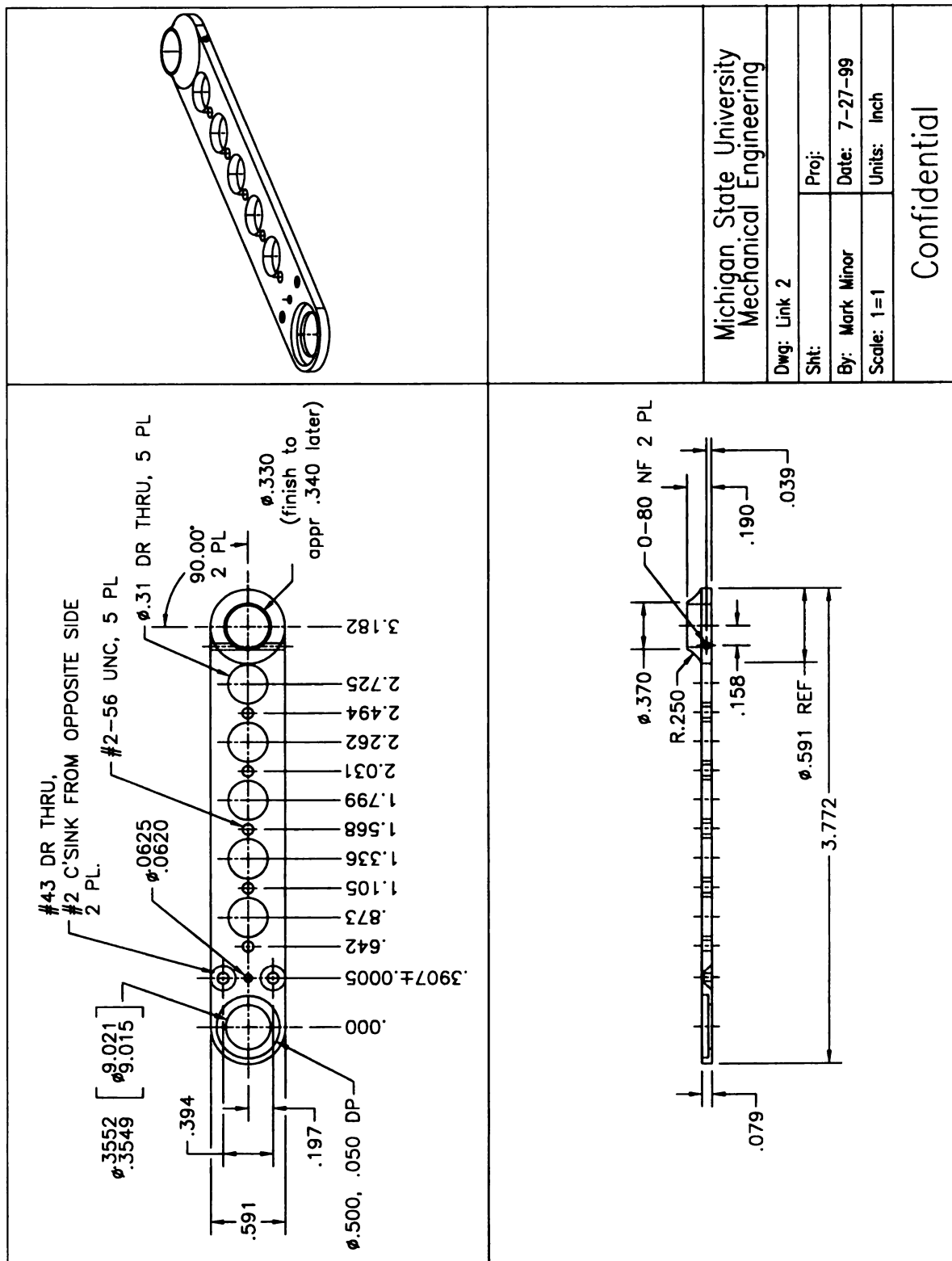


Figure 80. RAMR1 Component: Bracket for Motor #1.



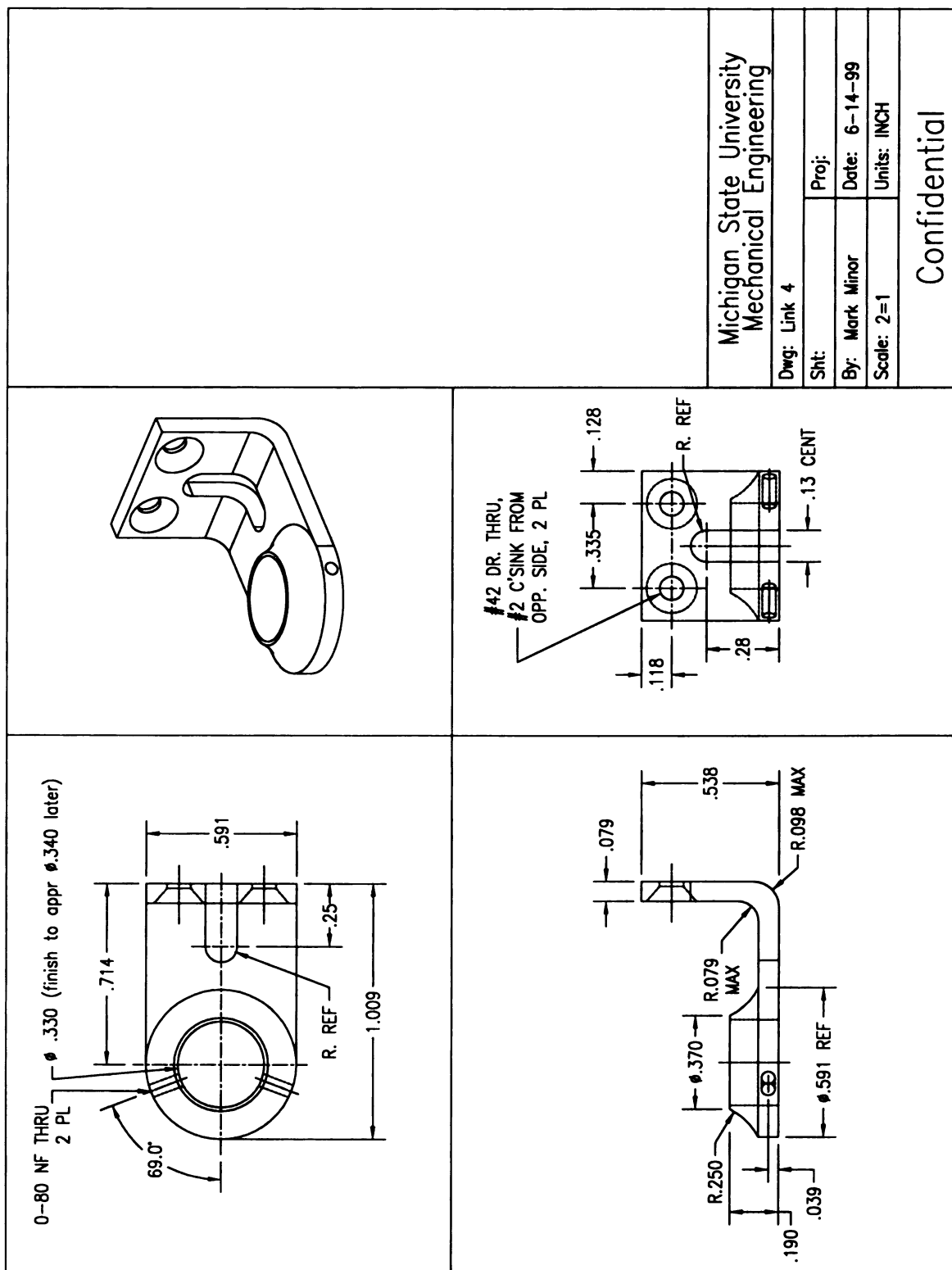


Figure 82. RAMR1 Component: Link #5

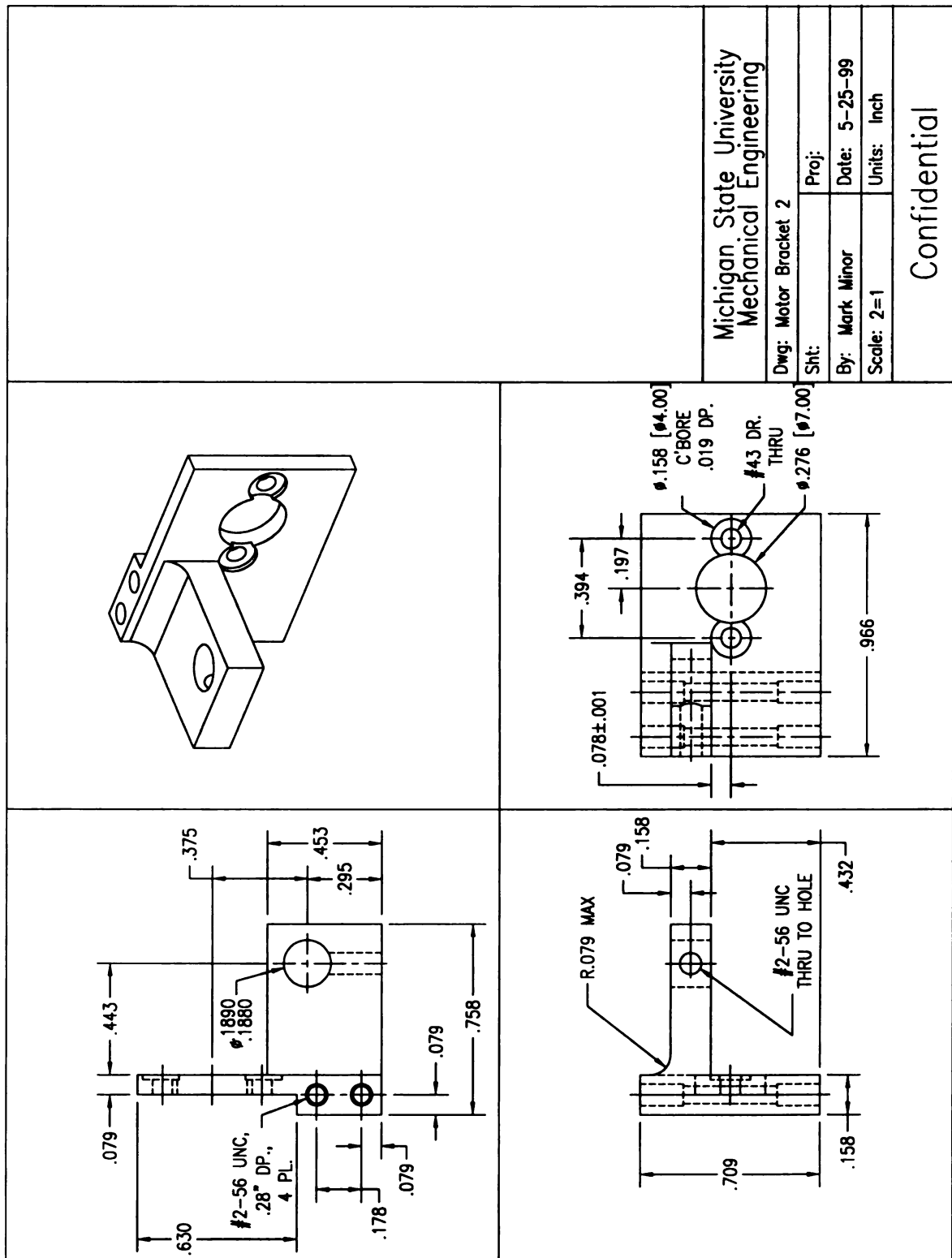


Figure 83. RAMR1 Component: Link 4 Bracket for Motors #2 and #3.

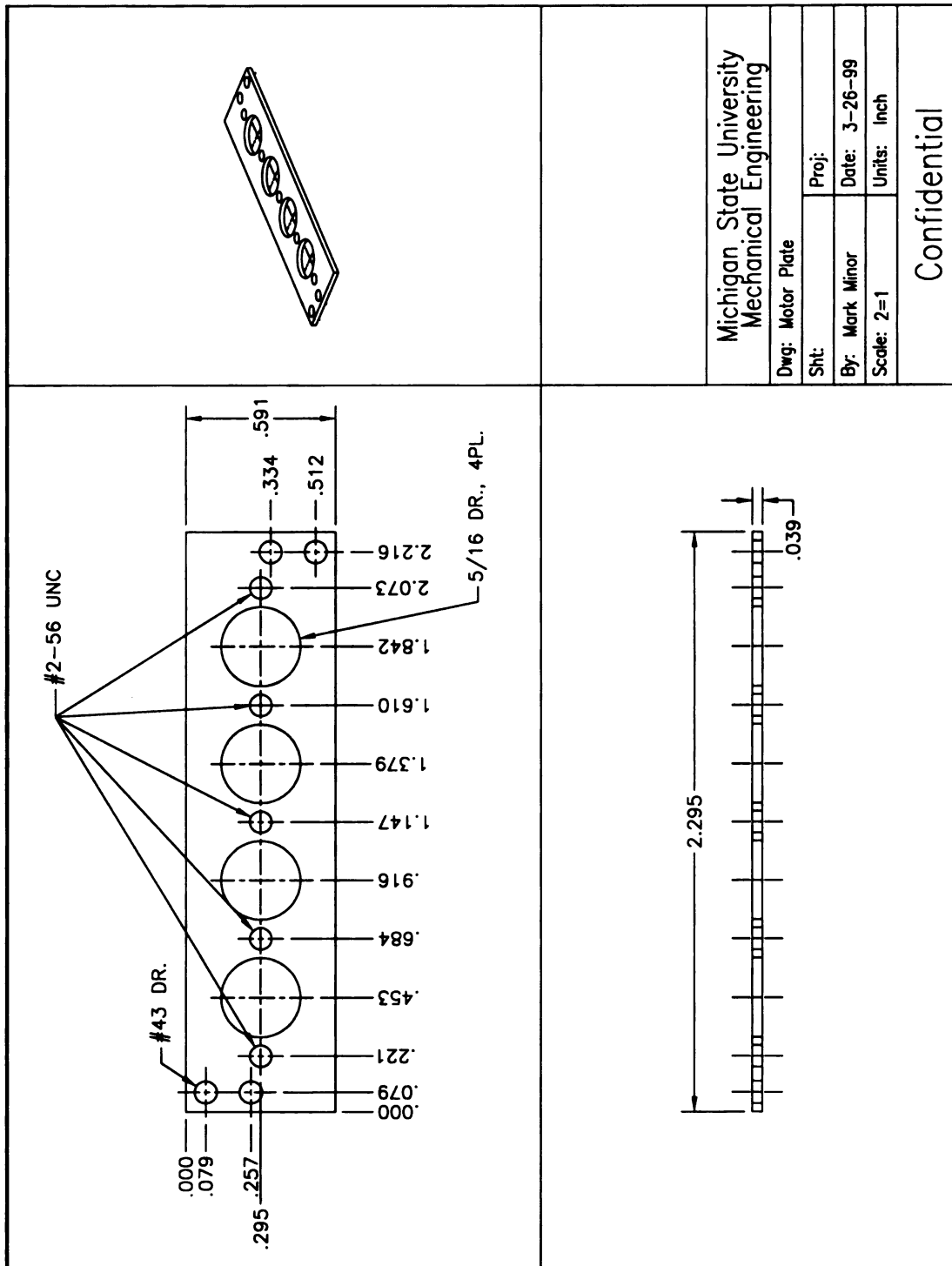


Figure 84. RAMR1 Component: Link 4 Motor Bracket Coupling Plate

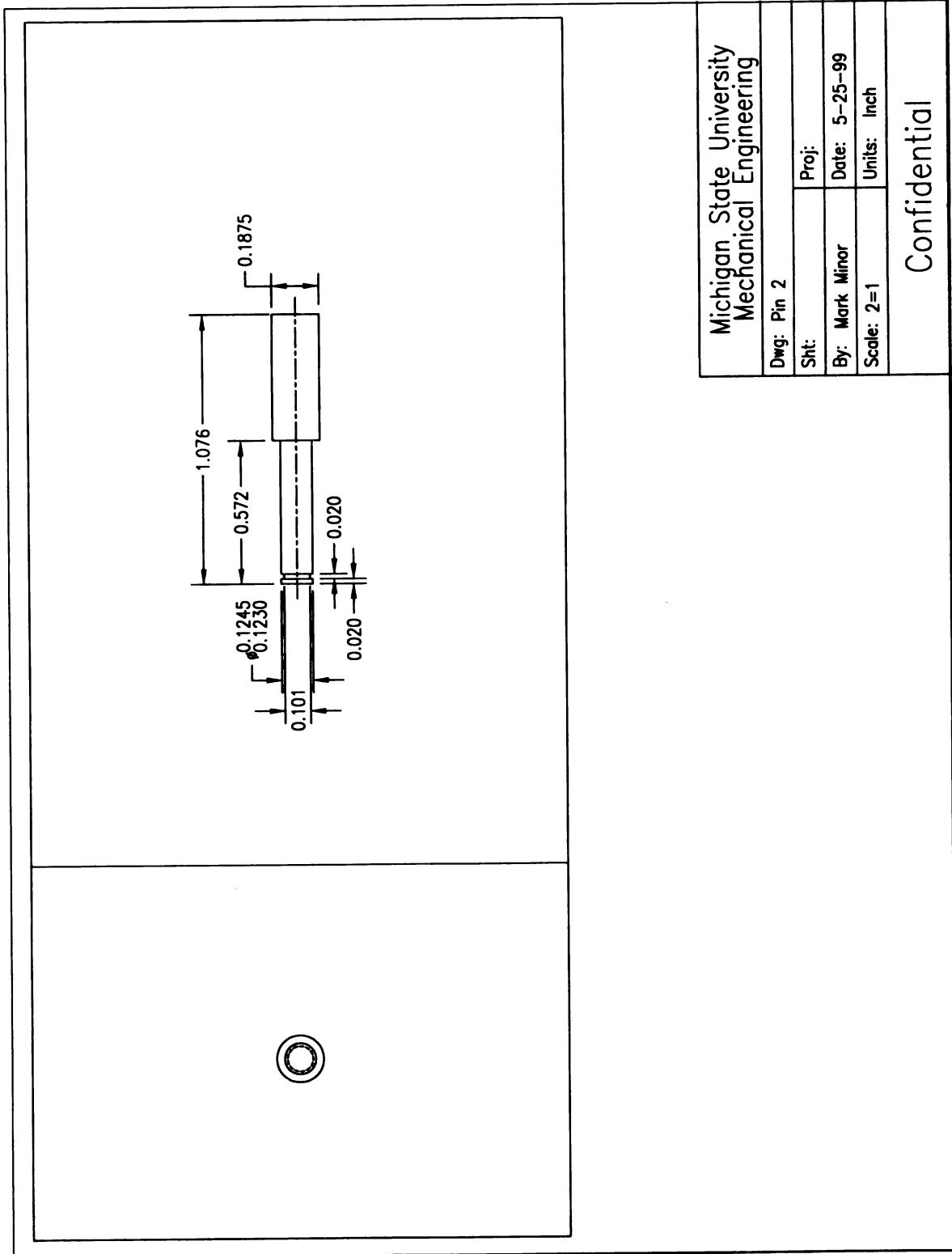


Figure 85. RAMR1 Component: Pin for Joint #3.

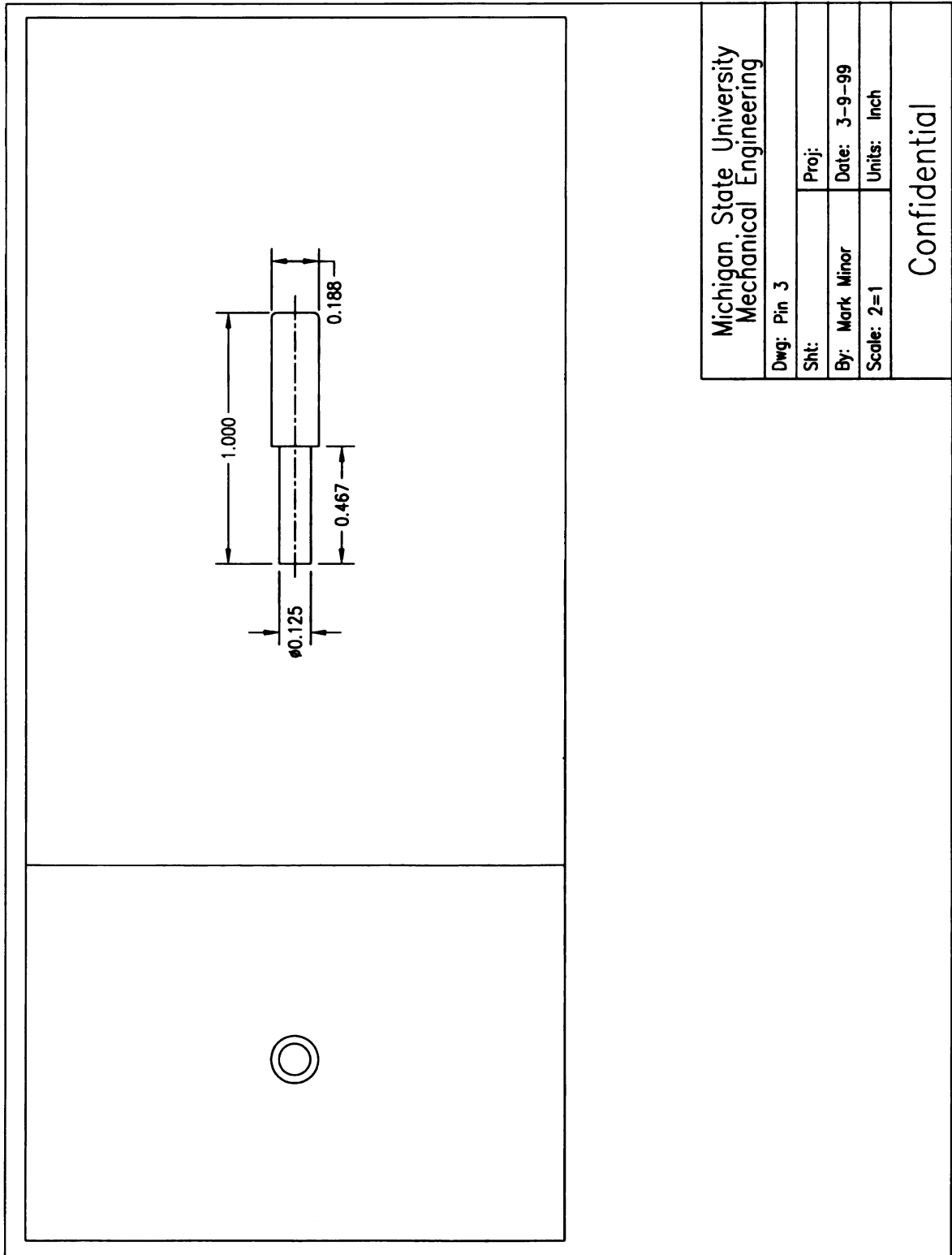


Figure 86. RAMR1 Component: Pin for Joint #4.

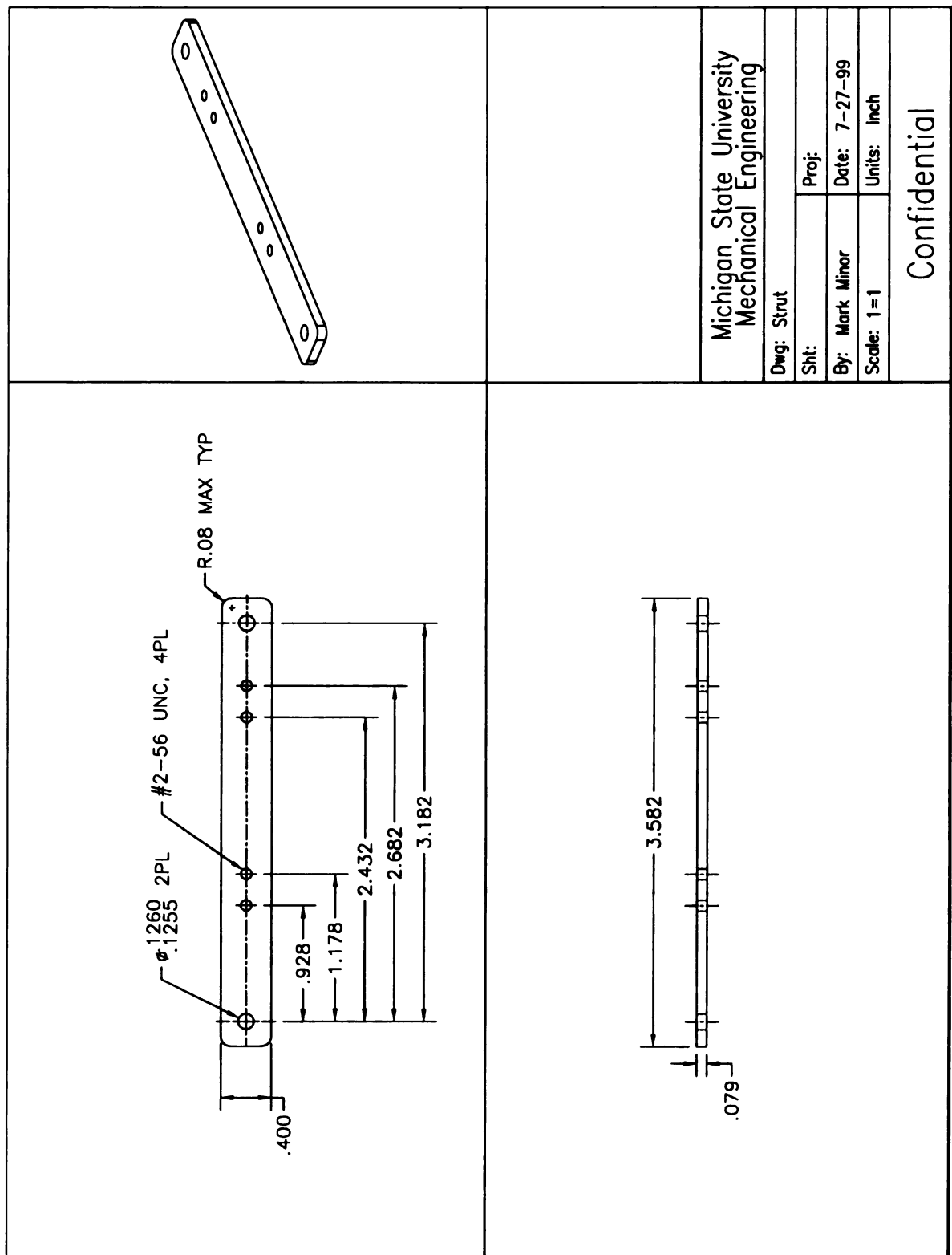
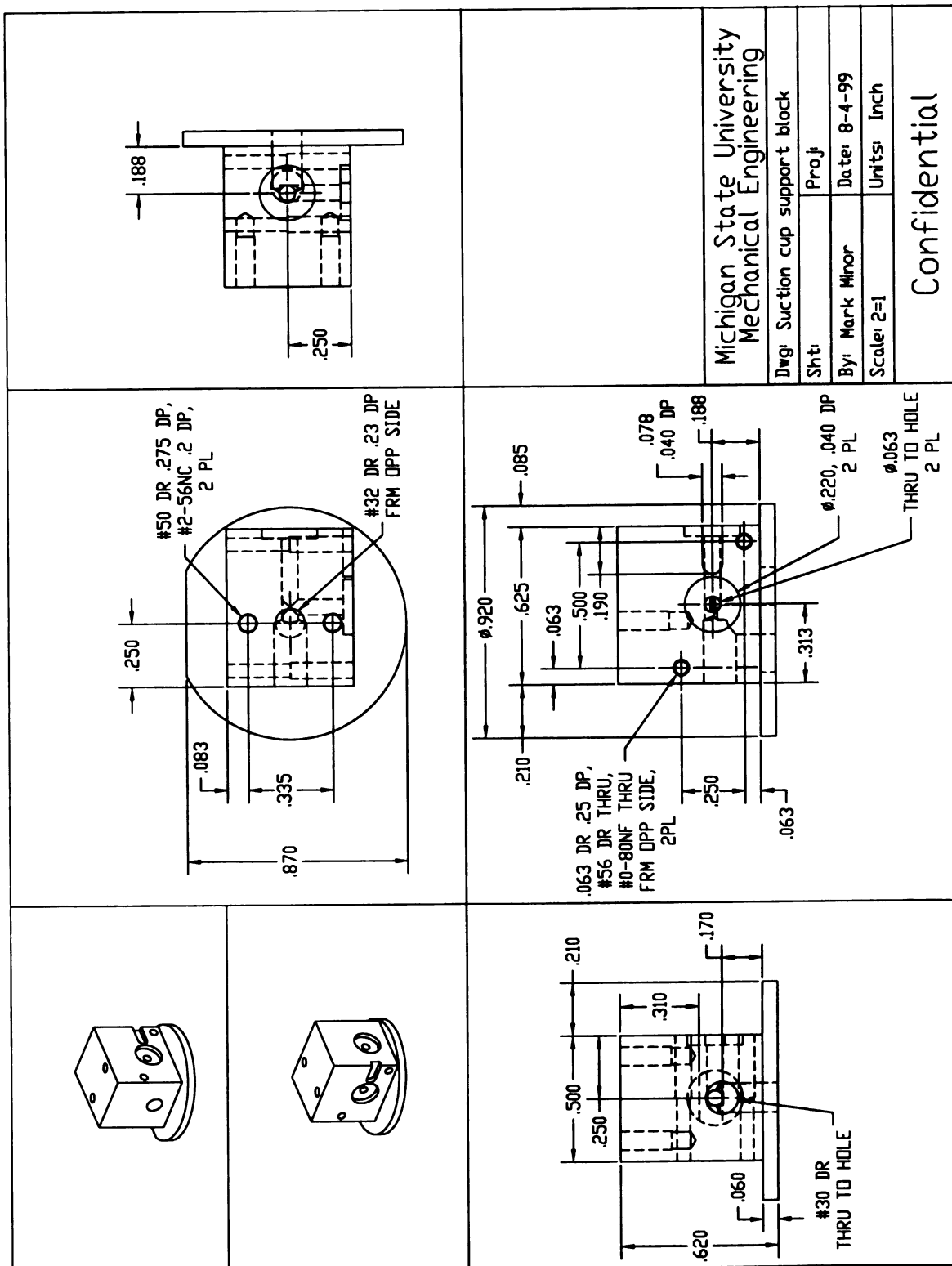
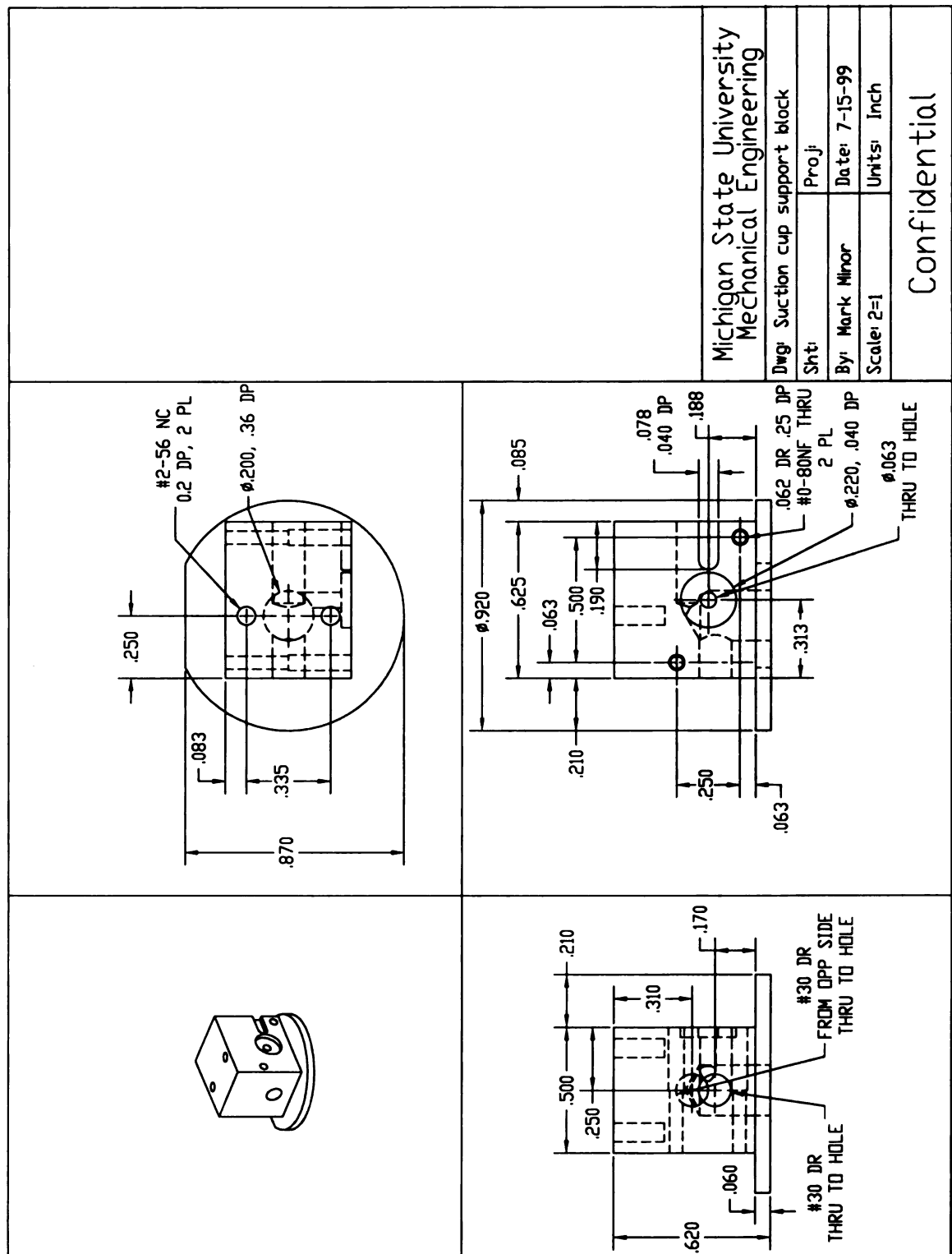


Figure 87. RAMR1 Component: Link 3 Support Strut.





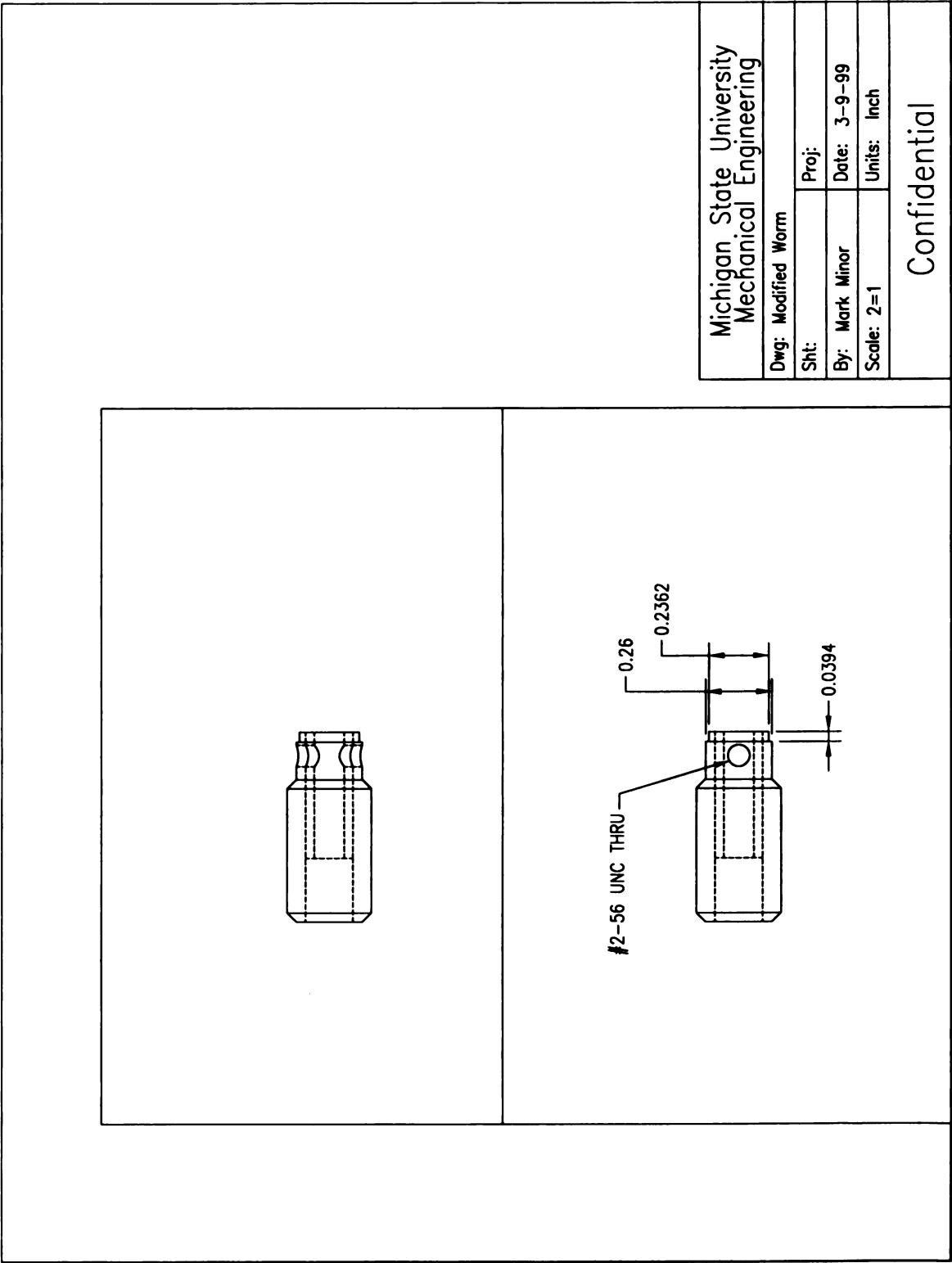


Figure 90. RAMR1 Component: Modified Worm.

MICHIGAN STATE UNIV. LIBRARY



31293021061787